Structural characterisation of semi-insulating LEC gallium arsenide

S. J. Barnett

To my Parents

ABSTRACT

Structural Characterisation of Semi-insulating LEC Gallium Arsenide

S J Barnett

Double crystal x-ray topography using a synchrotron radiation source has been used to measure the lattice distortions present in 50mm diameter samples of (001) semi-insulating LEC gallium arsenide. Lattice strains and tilts have been mapped in In-doped and undoped samples as well as annealed and unannealed samples taken from the seed and tail ends of boules. The properties of the x-ray source which are necessary for these measurements are discussed and it is concluded that a synchrotron source is the only practical choice.

Lattice strains of 90ppm and tilts greater than 100 arc seconds were measured in In-doped material both of which appear to be due to a combination of In concentration variations and the inhomogeneous dislocation distribution. Undoped samples were found to be more uniform with lattice strains of typically +20ppm towards the samples edges where the dislocation density is largest. The lattice tilt distribution in seed and undoped samples invariably exhibited a four-fold symmetry which was enhanced by the presence of lineage features lying along the <110> directions. Tail end samples were generally less uniform in lattice strain and showed a lower symmetry in their lattice tilts. These results are discussed in the light of current ideas concerning the origin of variations in lattice strain and EL2 concentration.

An x-ray diffraction method involving integrated intensity measurements of the quasi-forbidden 200 reflection, which is highly stoichiometry sensitive, is investigated. The results, however, show no conclusive stoichiometry variations but do highlight important experimental conditions which must be satisfied if such measurements are to be meaningful.

The images of dislocations in double crystal x-ray topographs are investigated and compared with theoretical simulations in order to assess the effects of point defect environment on the dislocation strain field. The results suggest that the EL2-dislocation interaction is not significantly strain driven.

CONTENTS

PREFACE

This thesis describes work undertaken from October 1982 at Durham University Physics Department and the Daresbury Laboratory synchrotron source, under the supervision of Dr B K Tanner (Physics Department) and Dr G T Brown (RSRE) and supported by the UK SERC and a CASE award from RSRE.

No part of this thesis has previously been submitted for a degree and any mention of work performed by other authors is duly referenced.

I would like to thank the Head of Physics, Professor A W Wolfendale, for provision of departmental facilities, and all the University staff who provided assistance during my time at Durham. I would also like to thank the UK Gallium Arsenide Consortium and Dr D A Hope of RSRE for the samples studied herein. I express particular thanks to my supervisor, Dr Brian Tanner, for his encouragement and helpful supervision and to my industrial supervisor, Dr Graham Brown, for many useful discussions and patient guidance.

Thanks are also due to the following:
Staff at the Daresbury Synchrotron source, particularly Dr Graham Clarke for assistance with the diffraction equipment.
Dr Martin Hill, Mr Bryan Barry, for experimental assistance
Dr M S Skolnick for provision of the infrared microscopy facilities
Dr Y Epelboin for provision of the dislocation image simulation programs
Peggy Cox and Sally Clay for typing this manuscript
Dorcas Dosser for proof-reading

Finally, all my friends and colleagues for their encouragement, particularly during the final stages of thesis preparation.

Some of the work presented herein has been previously published in the open literature, as detailed below:

"The structural characterisation of semi-insulating GaAs by double crystal x-ray topography"
G T Brown, M S Skolnick, G J Jones, B K Tanner, S J Barnett
Proc. Semi-Insulating III-V Materials Conference, Kah-nee-ta (1984) pp76-82

"Investigation of the homogeneity and defect structure in semi-insulating LEC GaAs single crystals by synchrotron radiation double crystal x-ray topography"
S J Barnett, B K Tanner, G T Brown
Mat. Res. Soc. Symp. Proc. Vol. 41 (1985) pp83-88

"X-ray double crystal topographic studies of III-V compounds"
B K Tanner, S J Barnett, M J Hill
Inst. Phys. Conf. Series 76 (1985) pp429-438
Microscopy of Semiconducting Materials Conference IV, Oxford (1985)

"The distribution of lattice strain and tilt in LEC semi-insulating GaAs measured by double crystal x-ray topography"
S J Barnett, G T Brown, B K Tanner
Inst. Phys. Conf. Series, 87 (1987) pp615-620
Microscopy of Semiconducting Materials Conference V, Oxford (1987)

1. GaAs PROPERTIES AND GROWTH

1.1 Introduction

1.2 Growth of single crystal GaAs

1.3 LEC growth of GaAs

1.4 Characterisation of semi-insulating LEC GaAs

a. Undoped semi-insulating GaAs

b. In-doped semi-insulating GaAs

1.1 Introduction

There is intensive research proceeding throughout the world with the aim of producing integrated circuits and discrete devices capable of operating at faster speeds. This requirement is being driven by the need for faster computers for real-time data processing, both in the civilian and military fields, and high frequency amplifiers necessary for direct broadcasting satellites and military radar systems. While Si will always dominate the IC market and increases in speed are continually being achieved by use of novel structures and fabrication techniques, there are intrinsic speed limitations to Si-based systems imposed by the material properties of Si. Thus there is a requirement to exploit the properties of the intrinsically faster III-V semiconductors of which GaAs is the most extensively studied and most highly-developed example. GaAs as a material offers several advantages over Si:

a) higher electron mobility - an order of magnitude greater than Si

b) lower electron effective mass - 7% that of Si

c) direct band gap material - higher efficiency opto-electronic and photovoltaic devices

d) can be alloyed with other group III and V elements to tailor the bandgap - laser action at the required wavelength

e) greater radiation hardness than Si - (10^7-10^8rads.) more suitable for space and military applications

f) can operate at higher temperatures than Si

Currently GaAs only holds a small percentage of the substrate market and price is an important factor in determining the future market share. Current prices are approximately £5 per cm^2 for GaAs compared to only 11p per cm^2 for Si.

Also GaAs wafer size is much smaller than Si (3" cf 8") making GaAs wafer processing less efficient. There are, however, many applications where this price offset can be overcome by increased performance. For example, radiation hardness and increased efficiency of GaAs photocells make them ideal for power generation on satellites where the increased cost is insignificant compared to the increased efficiency and longer life. The current market for GaAs devices runs at approximately $50M compared to that of Si, which is $25,000M - only a 2% market share. This market share is dominated by analogue devices but as we move towards the 1990s the IC share of the market will begin to dominate with a total predicted value of $800M (ref.1). The market for GaAs substrates is at present dominated by semiconducting horizontal Bridgman grown crystals for use in opto-electronic devices. Again, as we move into the 1990s the market is expected to change and become dominated by undoped semi-insulating GaAs produced by the liquid encapsulated Czochralski technique which will be used as a substrate material for IC fabrication by direct ion implantation.

For the large scale integration of digital devices and device compatibility it is necessary to achieve a high uniformity of device performance. For example, the digital application of GaAs enhancement mode FETs fabricated by direct ion implantation into undoped semi-insulating substrates requires a threshold voltage uniformity of less than 25mV. Current technology is capable of producing threshold voltage variations of typically σV_{th} $\approx$60mV (ref. 2) in undoped GaAs and there is much evidence sugesting that substrate non-uniformity is the primary cause of these variations. There is therefore intense research into the structural, compositional and optical non-uniformities present in semi-insulating GaAs, a review of which is presented in section 1.4. Compared with Si, there are many more problems associated with the growth of GaAs substrates and their subsequent processing into devices, either by direct ion implantation or via epitaxial growth. These problems arise partly because of the relative immaturity of the GaAs processing industry compared to that of Si, but mainly because

GaAs is intrinsically more difficult to grow and process. The problems originate at the crystal growth stage due to the low critical resolved shear stress of GaAs, which results in a high dislocation density in substrate material. The dislocation distribution is inhomogeneous which, it is thought, leads to non-uniform electrical properties and consequently to non-uniform device performance. The high temperatures encountered during device processing can lead to type conversion due to As loss or diffusion of a dopant, eg Cr. Many problems have been solved for particular device manufacturing processes but the problem of substrate uniformity still exists and plays an important part in affecting device performance.

1.2 Growth of single crystal GaAs

Bulk single crystal GaAs is manufactured via its polycrystalline state from its constituent elements Ga and As, of which there is a supply sufficient to satisfy current and projected demands. Whether or not these demands are met will depend on economic constraints and the ability of the high purity producers to predict and react to market trends. Ga is present at about 0.005% in bauxite and concentrates naturally in one of the steps during aluminium production. 90% of today's high purity Ga is obtained from this source with production levels being determined by economic incentive. (6N purity Ga sells for approximately $450 per kg.) As is produced as a by-product of ore smelting, especially lead and zinc ores. Most of the As produced is used in the pesticide and herbicide industry, but due to increasing awareness of the environmental effect of these poisonous compounds its use is declining and the semiconductor industry, with its high added-value products, should have no difficulty in increasing its share of this market. (6N purity As sells for approximately $150 per kg.)

There are two high volume commercial production methods of single crystal

GaAs; the horizontal Bridgman (HB) method and the liquid encapsulated Czochralski (LEC) method, both of which have produced variants which are utilised at the research stage. HB growth, because of its greater maturity and cheaper manufacturing costs, is responsible for approximately 90% of GaAs wafers. These HB grown crystals are contaminated with Si from the fused silica growth container and are consequently, in their undoped state, n-type semiconducting. Undoped HB material thus tends to be primarily used for light emitting diodes, laser diodes and photovoltaic devices where the substrate is used as a platform for epitaxial growth. If HB material is doped with Cr, which behaves as a deep acceptor and compensates for the Si shallow donors, it becomes semi-insulating and can be used for IC fabrication where good electrical isolation is required. A major attribute of LEC material is that it can be grown in a high purity state with a low Si concentration and is semi-insulating in its undoped state. The remaining impurities, mainly C, a shallow acceptor, are compensated for by the native deep donor known as EL2 (fig. 1.1).

LEC material has several advantages over Cr-doped HB material for the production of ICs. Firstly, the LEC material is produced in round wafers 2" or 3" in diameter, which are necessary for wafer processing machinery developed for the Si processing industry. Cr-doped HB material is 'D' shaped and cutting this into circular wafers is expensive and wasteful, as is the production of new wafer processing machinery capable of handling 'D' shaped material. Secondly, there is lower electron impurity scattering in undoped material and therefore a higher electron mobility. Thirdly, because of the high diffusion coefficient of Cr in GaAs, there is a tendency during processing at high temperatures for Cr to diffuse to regions where it is not required. For these reasons the role of SI LEC GaAs in the substrate market is likely to increase over the next decade, although there are problems associated with the higher dislocation density and its non-uniform distribution.

1.3 LEC growth of GaAs

The Czochralski method of crystal growth named after its inventor, was first reported in 1917 (ref. 3) and was subsequently developed by Teal and Little (ref. 4) in the 1940s and 50s, to a state where it was useful to the semiconductor industry. The method involves the pulling of a seed crystal from a melt consisting of the crystal compound. The temperature at the surface region of the melt is such that the melt freezes onto the seed which is being slowly 'pulled' from the melt. The Czochralski method of growth for Si is well developed and dislocation free material is available commercially up to 8" in diameter. The major developments in the Czochralski growth of GaAs are described below, along with some of the problems encountered.

The dissociation pressure of As from GaAs at its growth temperature (1238°C) is 1atm; therefore, in a standard Czochralski puller, growth of stoichiometric GaAs can only be achieved if the entire containing vessel is kept at a temperature of 550–600°C and there is sufficient vapour pressure of As above the melt to prevent dissociation. A similar problem was first tackled by Metz, Miller and Mezelsky (ref. 5) when growing PbTe crystals. They placed an encapsulating liquid immediately above the melt, above which was an over pressure of inert gas sufficient to prevent dissociation of the more volatile melt species. This enabled them to use a standard puller to grow crystals of materials whose melts contained volatile species.

A suitable and widely-used encapsulant is B_2O_3. The liquid encapsulation (LEC) method was first used to grow GaAs by Mullin et al (ref. 6) in 1965. They used a standard Ge puller and covered the melt with about 1cm of B_2O_3 to prevent dissociation of As from the melt. When the crystal is pulled through the encapsulant there remains a thin layer of B_2O_3 covering the crystal, thus preventing As loss from the pulled crystal which is still at high

temperature. Having solved the problem of how to grow GaAs under more favourable conditions the next problem to be solved was that of automatic diameter control.

As an LEC crystal is 'pulled' the volume of the melt decreases and, therefore, the power required to maintain the melt at the correct temperature for constant diameter growth decreases as growth proceeds. Some automatic method of diameter control is clearly essential. During the commercial growth of Si, the diameter of the pulled crystal is controlled by optically monitoring the shape of the melt/crystal meniscus as it meets the growing crystal surface. Changes in the meniscus shape reflect changes that are about to occur in the crystal diameter (ref. 7) and so, with the aid of feedback mechanisms, the pulling rate and/or heater power can be adjusted to produce a constant diameter crystal. The B_2O_3 used as the encapsulant during GaAs gorwth is only semi-transparent. This, coupled with refractive index fluctuations in the high pressure gas above the melt, makes the above method of diameter control ineffective. Another approach to diameter control, first used by Bardsley et al (ref. 8) for the growth of Ge crystals, is to monitor the weight of the melt during growth. Then either the measured weight or its differential with respect to time can then be compared with a theoretical estimate of that quantity and adjustments made to the pulling rate and heater power in order to produce a crystal of constant cross-sectional area. This is the method currently employed for the commercial production of LEC GaAs.

Until 1977 the crucibles used to contain the GaAs melt were made from fused silica which resulted in a high Si impurity level in the grown GaAs crystals (Si concentration - greater than $10^{16}cm^{-3}$). The resulting crystals were therefore n-type due to the incorporation of Si on Ga sites, which acts as a shallow donor. High resistivity material was produced by doping with Cr which acts as a deep acceptor (0.79eV below the conduction band) and compensates for the Si

donors to produce semi-insulating material (resistivity $>10^7$ohm cm). In 1977 Swiggard et al (ref. 9) reported the growth of undoped semi-insulating material from pyrolytic boron nitride crucibles. The concentration of Si (approx. $5x10^{14}cm^{-3}$) is then sufficiently low that C impurities, which act as shallow acceptors, can compensate for the Si donors. Any remaining C impurities are then compensated for by the native defect EL2, a deep donor. The resulting material is then semi-insulating with higher electron mobility than Cr-doped material due to lower impurity scattering. Thus it is the native defect EL2 which is ultimately responsible for the semi-insulating properties of undoped LEC material. Although the growth of semi-insulating material was then possible, it was not a consistently reproducible process until 1982 when Holmes et al (ref. 10) reported the effects of As melt concentration on the resistivity of the grown crystal. They found that the EL2 concentration increased from $5x10^{15}cm^{-3}$ to $1.7x10^{16}cm^{-3}$ as the As atomic fraction of the melt increased from 0.48 to 0.51. This resulted in a critical As melt fraction of 0.475 above which there was sufficient EL2 to compensate the residual C acceptors and give rise to high resistivity semi-insulating material. Below this As concentration limit the residual C acceptors are uncompensated and the material is p-type. These results were the first to suggest a link between EL2 and a native defect such as an As interstitial or Ga vacancy.

As previously mentioned, the critical resolved shear stress of GaAs is significantly lower than that of Si and because of the high thermal gradients encountered during growth the dislocation density in commercial material is relatively high (10^4-10^5cm^{-2}). Once formed, the dislocations move by a process of glide and climb into an inhomogeneous distribution, arranging themselves into cellular structures and linear arrays (lineage). Certain electrical properties have shown correlation with dislocation density, thus leading to the hypothesis that dislocation density and structure play an important role in determining the final device uniformity.

There have been two approaches aimed at reducing the dislocation density:

a) Reduction of the thermal gradients encountered during the post-growth cooling stage. These have been reduced by the addition of post growth heating elements which surround the pulled crystal. The pulled crystal can then be maintained at a high temperature and after growth the whole crystal cooled slowly and more uniformly. Another approach is fully to encapsulate the pulled crystal in B_2O_3 (the FEC method). This reduces the heat conducted from the pulled crystal to the ambient high pressure gas and therefore reduces temperature gradients. There are, however, problems associated with reducing the temperature gradients. As the thermal gradients are reduced the growth diameter is liable to change very rapidly for small melt temperature fluctuations, thus making the growth of constant diameter crystals more difficult. Both these methods go some way towards reducing the dislocation density in substrate material.

b) If In is alloyed into GaAs the lattice is hardened, giving it a higher critical resolved shear stress and thus making dislocation formation more difficult (refs. 11, 12). This method, when combined with the FEC method, is capable of producing dislocation-free material. There are, however, problems of non-uniformity in the grown crystal; time-dependent convective currents in the melt cause In concentration fluctuations in the grown crystal (striations), and since the segregation coefficient of In in GaAs is less than one, there is a gradual increase of In concentration in the crystal as growth proceeds. If a vertical magnetic field of 1200Oe is applied to the melt during FEC growth (ref. 13) then the In growth striations are reduced and it is possible to achieve extremely uniform material on which enhancement mode FETs have a threshold voltage scatter σVth $\approx$17mV (ref. 2). There are however some detrimental effects associated with In doping; In strains the GaAs lattice and if GaAs layers are epitaxially grown on In-doped substrates the strain can cause the formation

of misfit dislocations at the substrate/layer interface. The EL2 concentration is lower in In-doped material; it is therefore necessary to have a low C concentration in order that the material is semi-insulating. The activation efficiency of Si implants in In doped material is generally lower than for undoped material; this arises from the amphoteric nature of Si which has a greater tendency to occupy As sites in In-doped material. Thus In doping is capable of giving improved uniformity but because of the detrimental effects listed above it is not certain that it produces the ideal material for all fabrication processes.

From the above brief history describing the major developments in the LEC growth of semi-insulating undoped GaAs it is clear that there are still many problems to be solved in order to produce uniform material with a high resistivity and electron mobility. The use of In-doping goes some way to reaching this goal but whether it is the ultimate solution is not clear. The next section goes on to discuss the results of various substrate characterisation exercises which have formed the current theories relating to the sources of non-uniformity of LEC material.

1.4 Characterisation of SI LEC GaAs (substrate uniformity)

1.4 a Undoped semi-insulating LEC GaAs

The ultimate measure of substrate quality is the uniformity and performance of the devices manufactured on that substrate. Studies of FETs made by direct ion implantation into undoped SI LEC material have revealed 'W' shaped profiles of threshold voltage as a function of position across a wafer diameter (refs. 2, 4). More detailed studies using small geometry FETs have shown inhomogeneities in threshold voltage (refs. 2, 15) that are linked to the macroscopic dislocation structure. It is important to determine which substrate

properties give rise to the threshold voltage non-uniformity. To this aim many methods have been used to study the electrical, optical and structural properties of SI LEC GaAs.

Etching studies have been undertaken by a number of authors (refs. 16, 17) with the aim of revealing the dislocation distribution and density in wafers as a function of growth parameters. The two most commonly used etches are molten KOH (ref. 18) and the so-called AB etch (ref. 19). The molten KOH etch reveals dislocations as they meet the crystal surface as pits and a one-to-one correlation between etch pits and dislocations has been established by x-ray topography (ref. 20). The dislocation density distribution across 50mm diameter wafers has been found to be 'W' shaped (refs. 16, 17) with cellular and linear clustering of dislocations. (Large cell size is indicative of low average dislocation density, 100μm diameter cells correspond to an average epd of $1x10^{5}cm^{-2}$.) The etch pit density (epd) on a (001) wafer shows 4-fold symmetry (ref. 16), as might be expected from crystal anisotropy considerations. Theoretical calculations of dislocation density (ref. 21) have been undertaken assuming the dislocation density to be proportional to the actual resolved shear stress in the crystal minus the critical resolved shear stress summed for each slip system. The calculated dislocation distribution shows the same 4-fold symmetry as that experimentally observed and predicts that, for zero dislocation density undoped material, (over any part of the wafer) a maximum of 40°C temperature difference between ambient and melt is required (in commercial pullers this is typically 200°C). The AB etch, on the other hand, is sensitive to the local environment of the dislocation, specifically the Fermi level. Dislocations in cell walls or lineage features that lie parallel to the crystal surface etch as grooves, while those isolated in the cell centre etch as ridges (ref. 17, 22). Both types of etch feature are dotted with pits indicating the presence of precipitates which have been identified as hexagonal As (ref. 23).

Resistivity and leakage current measurements (refs. 24, 25) reveal an 'M' shaped profile across the wafer diameter, the inverse of epd. Sheet carrier concentration measurements (ref. 26) reveal a 'W' shaped profile. As previously mentioned, measurements of the resistivity as a function of melt composition (ref. 10) show that for growth of semi-insulating material (resisitivity $>10^7$ohm cm) there is a minimum As concentration in the melt and lower As concentrations give rise to p-type material due to uncompensated C acceptors.

Infrared absorption measurements at 1μm wavelength, which have been shown to represent the concentration of the deep donor EL2 in its neutral state (ref. 27) show a direct correlation with the dislocation structure. Dislocations arranged in cellular structures and lineage features are clearly visible as areas of increased IR absorption, indicating higher concentrations of EL2 (refs. 27, 28). The spatially averaged concentration shows a 'W' shaped profile with the minimums along the <110> directions being smaller than those along the <100> directions (ref. 29).

Cathodoluminescence images of SI LEC material (refs. 30, 31) show an increased total CL emission from cell walls and lineage features which is not uniform across the whole CL spectrum. The 1.51eV CL peak shows an increase at cell walls and a uniform level across the cell interior. A 0.68eV CL map shows the same profile, except in a region of approximately 20μm either side of the CL increase at the cell walls. Here there is a decrease in 0.68eV CL intensity with respect to that of the cell interior. This 0.68eV CL peak has been shown to be due to hole capture by neutral EL2 and thus there is a region surrounding the cell wall which is denuded of EL2. The increase of EL2 at cell walls and lineage features cannot be due to dislocations gettering EL2 as they climb as this would result in a diffusion-like EL2 profile. Instead there must be an attractive force between dislocations and EL2 which depletes the concentration of EL2 in the area surrounding cell walls (ref. 30).

The fact that melt composition affects the EL2 concentration has led to attempts to measure stoichiometry as a function of position on wafers and down the boule. This has been done using x-ray diffraction methods to measure accurately the lattice parameter, which it is thought depends on stoichiometry. Data from some of these studies is presented in fig. 1.2 but unfortunately results are inconclusive, with some indicating an increase in lattice parameter with respect to As melt concentration (refs. 32, 33, 34) and others a decrease (ref.35, 36). The validity of this lattice parameter data is questioned if one notes that the precision of each set of data is quoted by the authors to be, at worst, 1ppm but the total spread of all data sets exceeds 150ppm. (All the data is normalised to the same temperature and value of wavelength). The absolute stoichiometry and/or impurity concentration may play an important part in the spread. It is probable that the melt composition does not reproducibly represent the crystal composition since the amount of As lost during synthesis and growth is notoriously difficult to control. Okada et al (ref. 34) measured the lattice parameter of 'stoichiometric' samples supplied by three manufacturers and found lattice parameter differences of about 12ppm, which he ascribed mainly to differences in impurity concentrations. High impurity concentrations may play an important part in data sets 32 and 35 (fig. 1.2) since this material was produced in the 1960s and early 1970s before good impurity control was achieved. The usefulness of lattice parameter data is further questioned by measurements taken before and after dicing the wafer into 10x10mm^2 chips (ref. 37). The 'W' shaped lattice parameter distribution normally found across the wafer diameter in undoped LEC material which, in this case, had an amplitude of $1x10^{-4}$Å ($\Delta d/d$ = 17ppm) was reduced to $4x10^{-5}$Å ($\Delta d/d$ = 7ppm) upon dicing the wafer. This change revealed the effects of elastic distortion in the wafer, possibly due to the dislocation structure which, according to the author, was relieved upon dicing. He ascribed the strain remaining after dicing to stoichiometry variations but it is not clear why this could not be the remnants of an elastic strain introduced by the dislocation structure.

Some of the strongest evidence relating lattice parameter to crystal stoichiometry comes from Nakajima et al (ref. 33) who measured a consistent lattice parameter increase of 8.5ppm when they injected As into the Ga-rich melt of a LEC grown crystal. Also direct measurements of crystal stoichiometry have been made by Coulombic titration (refs. 38, 39, 40) and Terashima et al (ref. 39) have measured an increase in lattice parameter with increasing As composition in the crystal. Other corroborative evidence comes from measurements of Si implant activation against lattice parameter (ref. 41) which show an increased activation efficiency with increasing lattice parameter. This is interpreted by the author to be due to an increase in the As concentration which is consistent with other results, assuming that for increased As concentration the Si atoms are more likely to reside on Ga sites and therefore be electrically active. This latter observation is supported by Takano et al (ref. 42) who found a direct correlation between FET threshold voltage and the lattice parameter.

Measurements of the effects of 950°C anneals (ref. 43) show an increase in the EL2 concentration for the first 5 hours of the anneal, followed by a decrease until the process stabilises after several tens of hours. The above changes are accompanied by a gradual flattening of the EL2 profile across the wafer (refs. 43, 44). Other properties (infrared absorption, photoluminescence, cathodoluminescence and resistivity) all show an improvement in spatial uniformity after annealing (refs. 45, 46). The effects of 950°C anneals on lattice parameter have also been investigated (ref. 47) and show an increase for a 5-hour anneal but this trend is reversed if the anneal time is lengthened to 25 hours. This lattice parameter change is not accompanied by any improvement in lattice parameter uniformity (ref. 47). The thermal stability of the As_{Ga} (As on a Ga site) electron spin resonance signal (ref. 48) and its relationship to the EL2 distribution suggest that As_{Ga} is the origin of EL2 but there are several discrepancies (ref. 48) which exclude this simple model.

The purpose of the lattice parameter measurements discussed above was to establish a connection between strain and stoichiometry and, therefore, determine point defect concentration variations in order to speculate on the nature of the deep donor EL2 (EL2 cannot be impurity-related since its concentration usually exceeds the impurity concentration). The most credible lattice parameter trends (increasing with increasing As concentration) have been interpreted as an increase in As interstitials in As-rich crystals and an increase in As vacancies in Ga-rich crystals (refs. 33, 34, 39) and this interpretation agrees with Si implant activation efficiency data (ref. 41) and FET threshold voltage data (ref. 42). However, precise titration, density and x-ray density measurements (ref. 38) indicate that on either side of the stoichiometric composition the dominant defects are vacancies (since the x-ray density always exceeds the actual density). This latter set of data is, however, slightly suspect since the author did not use lattice parameter data from his own samples. The above stoichiometric interpretation of lattice parameter data is not unique, as is shown by the wafer dicing experiments of Okada (ref. 37) which reveal the presence of elastic strains in wafers which have been investigated by x-ray topographic methods.

X-ray topography has been used by several authors to investigate the defect structure and macroscopic strain in LEC undoped material and is used extensively in the present study. Double crystal topography using a synchrotron radiation source has shown the presence of dislocations arranged in cellular structures, slip bands and linear arrays (ref. 49) and has revealed lattice tilts associated with the dislocation structure (refs. 49, 50). Four-fold symmetric and eight-fold symmetric Bragg angle distributions (refs. 51, 52), depending on dislocation density, have been observed and lattice strains across a wafer of 20ppm (ref. 50) measured. This work is not discussed in detail here since it bears a similarity to the present work and is, therefore, referenced later in the context of the results presented in section 3.3.

1.4b Indium-doped GaAs

The growth of striation-free zero dislocation In-doped semi-insulating material has been reported by a number of authors (refs. 2, 13) who used the FEC method and applied a magnetic field during growth. This material gives good FET uniformity (threshold voltage scatter σV_{th} = 17mV) but is, however, not the ideal substrate for all device fabrication processes as outlined in section 1.3. Dislocated In-doped material behaves in many respects similarly to undoped material in that there is an improvement in EL2 uniformity on annealing (ref. 44). Resistivity variations which follow the dislocation distribution are also found and they depend critically on melt composition (ref. 53).

Since the dislocation density in In-doped material is generally 10^2–$10^3 cm^{-2}$ (c.f. 10^4–$10^5 cm^{-2}$ for undoped LEC material) it has been possible to study the dislocation structure in more detail using x-ray topography. Studies have classified the various types of dislocations as arising from different sources (refs. 54, 55) during crystal growth and comparisons of topographs with photoluminescence images indicate increased PL intensity around dislocations as in undoped material (ref. 56). PL measurements across wafers have indicated In concentration variations of 10–20% (refs. 57, 58) and these results, along with the x-ray topographic studies, are discussed in section 3.3 with reference to this work.

1.5 Aims of present work

The above section presents an outline of the characterisation exercises undertaken on LEC GaAs and highlights the dependence of electrical properties on the structural properties of GaAs. At the time of embarking on the present work (1983) the dislocation structure and lattice parameter variations had not been investigated to any great extent although the relationship between

dislocations and certain electrical properties had been well established.

The present work aims to use the high x-ray fluxes of low divergence available from a synchrotron radiation source in order to perform x-ray topographic studies of SI LEC GaAs. Relative lattice parameter and lattice tilt fluctuations will be studied as a function of position on 50mm slices and the effects of annealing and position in the boule will be assessed. The role of the macroscopic defect structure in determining non-uniformity will also be studied.

The next section discusses x-ray topographic techniques and goes on to discuss the source and diffraction optics required in this study. Section 3 presents the results, starting with initial investigations and leading on to the main study of lattice distortions in LEC material, the results of which are discussed in the light of the above review.

Section 4 describes x-ray work done in an attempt to optimise conditions for determining stoichiometry variations and in section 5 the x-ray topography images of dislocations present in the material are discussed.

Section 6 presents a brief overview and conclusion from this work.

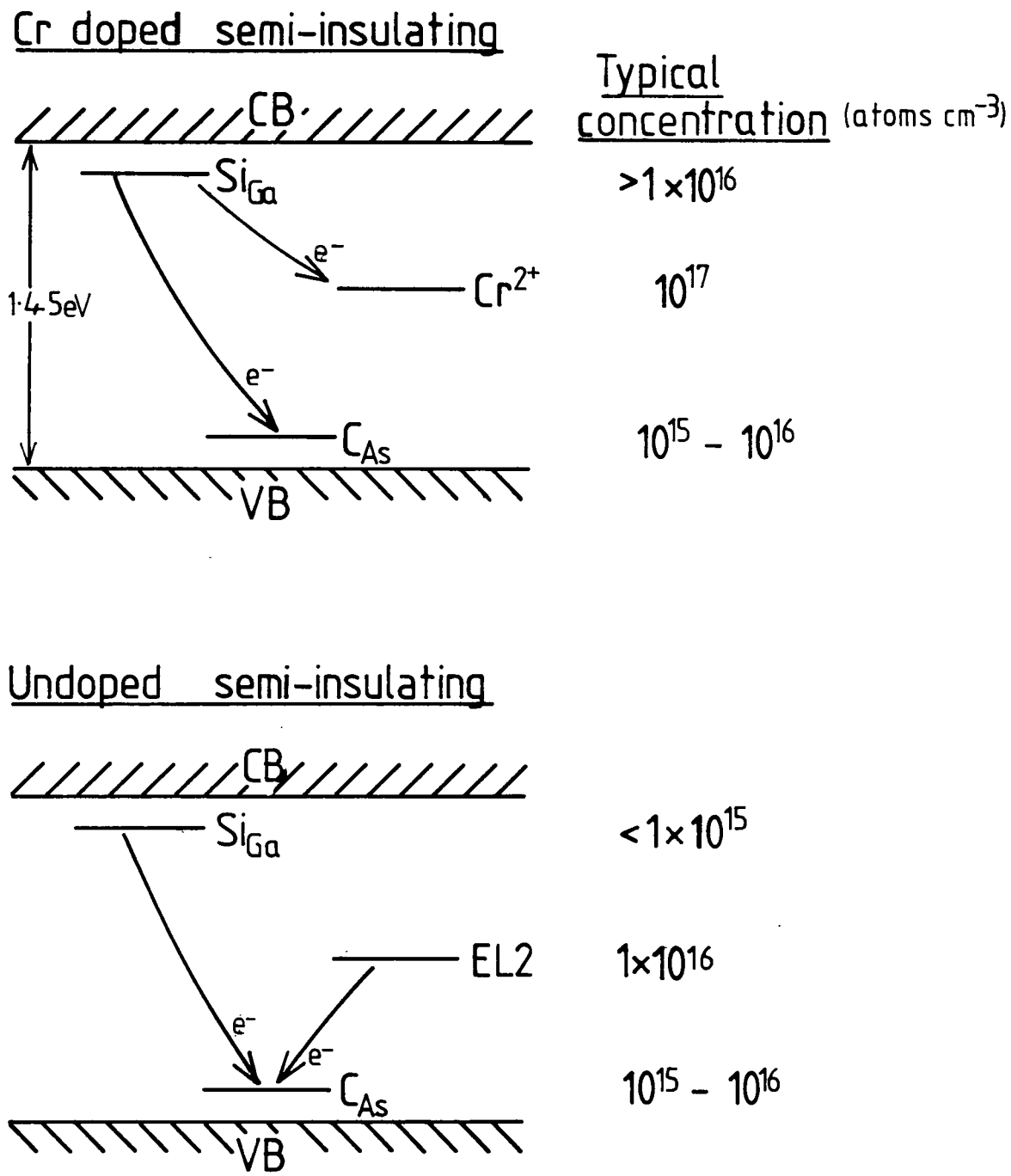

Fig. 1.1 Band gap energy level diagram of GaAs showing the major levels responsible for its semi-insulating nature

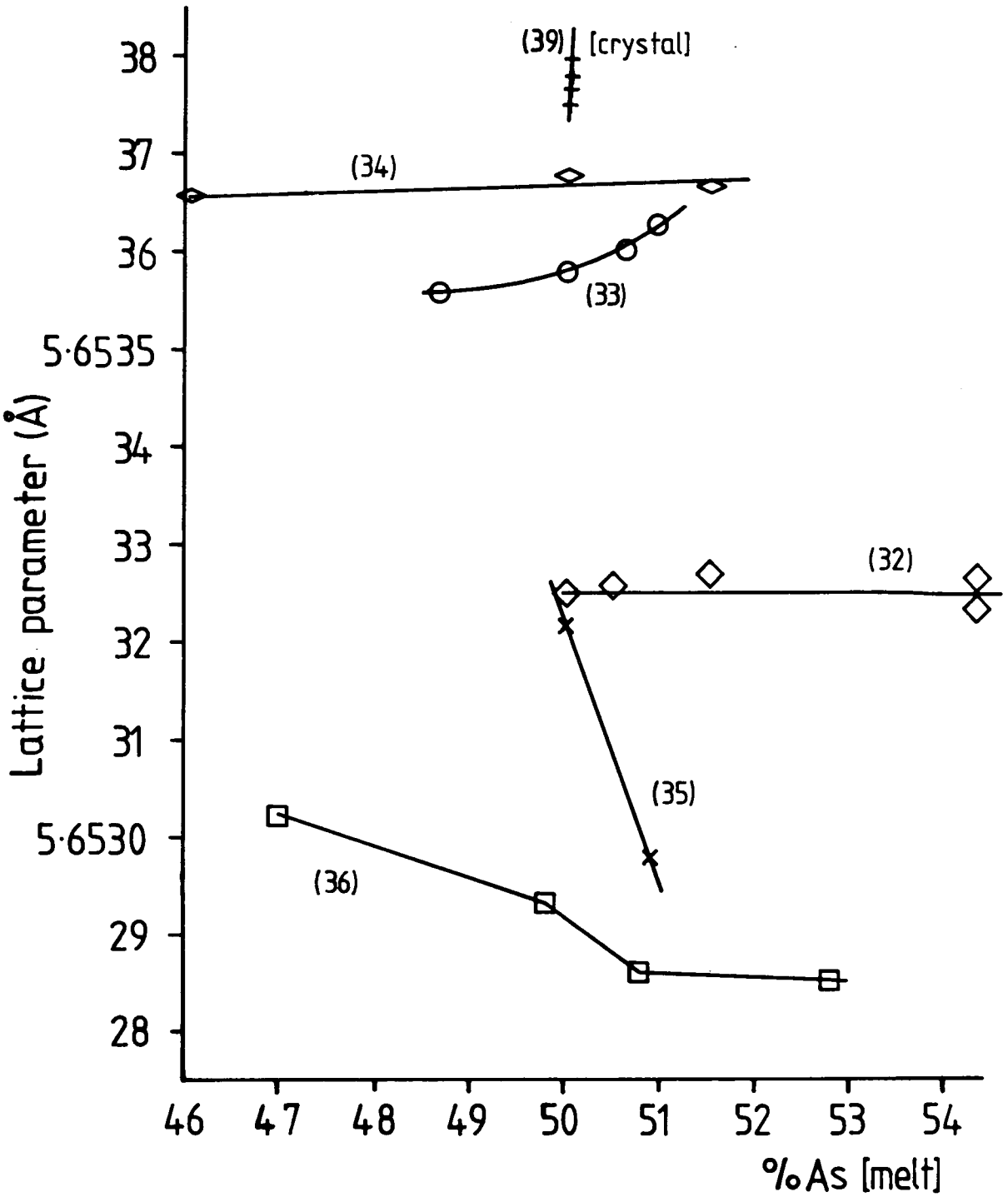

Fig. 1.2: Lattice parameter data measured as a function of stoichiometry after several authors. All data is normalised to the same temperature.

2. X-RAY TOPOGRAPHY

2.1 Introduction

2.2 X-ray topographic techniques

a Single crystal techniques

b Multiple crystal techniques

2.3 X-ray sources

2.4 X-ray diffraction methods for measuring lattice strain and tilt

2.5 Double crystal x-ray topography

a Du Mond diagrams

b Vertical beam divergence

c The theory of lattice strain and tilt measurements

d Reference crystals

2. X-RAY TOPOGRAPHY

2.1 Introduction

The increasing use of x-ray topography for the assessment of lattice defects in single crystals stems from the requirement to characterise more and more perfect crystals containing fewer and fewer defects. This is particularly so in the semiconductor industry where considerable effort is directed at the eradication of lattice defects which have adverse affects on electrical properties and certain fabrication processes. The high strain sensitivity and the ability to image large volumes of samples make x-ray topography an ideal technique for this application. The equipment necessary to record good quality topographs is relatively inexpensive and a wide range of systems is now commercially available. Such is its wide range of uses that most industrial and academic laboratories interested in the perfection of single crystals have at least one x-ray topographic technique at their disposal.

X-ray topography is, in many respects, complementary to transmission electron microscopy (TEM). Transmission electron microscopy offers a means of imaging short range strain fields at high magnification and it is ideally suited to materials containing a high density of defects (greater than 10^6 dislocations cm^{-3}) since, for electron transparency, samples must be less than $1\mu m$ thick and are consequently only a few tens of microns in lateral extent. X-ray topography, on the other hand, offers the means to study samples up to millimetres thick and 100s of mm in lateral extent, and can be sensitive to both short and long range strains. It is non-destructive since no special sample preparation is necessary so long as saw and polishing damage are removed. It is possible, for example, to study the same sample at various stages of a particular fabrication process, something which cannot be done with TEM.

X-ray rocking curves are typically 5-20 arc seconds wide compared to 0.5 degrees for electrons. This narrow reflection range gives x-ray topography its high strain sensitivity, typically 1 part in 10^6 for double crystal techniques, and results in large image widths compared to electron microscopy. Dislocation images are typically 15-100μm wide which limits the maximum concentration that can be tolerated before significant image overlap, particularly in transmission topography, to about $10^3 cm^{-3}$. Since x-rays are uncharged and their refractive index is very close to unity, it is impossible to produce an x-ray lens with a sensible focal length. The large image widths are therefore important, since the spatial resolution of the technique is limited in practice by that of the recording medium which, at best, is 0.5μm for nuclear emulsion plates.

For many years, because of the lack of a powerful x-ray source, many x-ray topographic techniques were very time-consuming, particularly in the transmission mode where one traverse topograph recorded on a high resolution plate could take tens of hours. In recent years reliable rotating anode sources have been developed with brilliances an order of magnitude greater than sealed tube sources, and with the advent of dedicated synchrotron radiation (SR) sources producing highly collimated x-ray beams with usable fluxes three orders of magnitude higher than standard cooled target sources, there has been a revived interest in x-ray topography. Real-time topography of dynamic processes in crystals is possible using TV imaging systems, and the use of cryostats, magnets, mechanical deformation stages and environmental chambers is made easier.

This chapter gives a brief outline of the most commonly used topographic techniques and then discusses the requirements of this project, along with the x-ray optics of the particular technique which was used.

2.2 X-ray Topographic Techniques

The many x-ray topographic techniques can be split into two distinct classes, single and multiple crystal techniques. Single crystal methods use an incident beam which has an angular divergence or spectral width at least one order of magnitude greater than the rocking curve width of the sample crystal. Multiple crystal methods use one or more 'perfect' crystals to limit the divergence and/or spectral width of the beam, such that the sample is subject to a highly collimated monochromatic beam of x-rays. As a result of the divergence, single crystal techniques are sensitive to short range strain gradients such as those surrounding lattice defects, while multiple crystal techniques can also be sensitive to small, long range strain fields and misorientations. The two categories of techniques are thus sensitive to particular contrast mechanisms.

Broadly speaking there are two types of contrast in x-ray topography; orientation contrast and extinction contrast. Orientation contrast, as its name implies, arises from areas in the crystal where there is a misorientation of the lattice. When using characteristic radiation, if the misorientation is greater than the divergence of the incident beam then no diffraction occurs from the misorientated region. Extinction contrast arises from the disruption of the perfect crystal wavefield by a strain gradient such as those surrounding extended lattice defects. Depending upon the severity of the distortion and the diffraction geometry, the contrast can vary from a simple increase or decrease of diffracted intensity to complex interference patterns. Dynamical diffraction theory is required to give an accurate description of extinction type contrast (see Chapter 5).

The most commonly used techniques are briefly described below, along with their particular applications. For more detailed discussions of these techniques, see Tanner (ref. 59), Tanner and Bowen (ref. 60) and Lang (ref. 61). For

explanation of diffraction theory and other related technical terms, reference should be made to Tanner (ref. 59), Batterman and Cole (ref. 62) and Pinsker (ref. 63).

2.2a Single Crystal Techniques

Berg-Barrett Topography (Fig. 2.1a)

The technique was developed by Berg in 1931 (ref. 64) and refined by Barrett in 1945 (ref. 65). It should be used as the first tool to assess crystal quality as it is the least sensitive and quickest topographic technique. It is used in the reflection mode using characteristic radiation and an asymmetric reflection. Suitable diffraction conditions are chosen such that the incident beam makes an angle of a few degrees with the crystal surface and the diffracted beam emerges as close as possible to the normal to the crystal surface, thus enabling short sample-to-film distances in order to give good spatial resolution. Since the depth of sample contributing to diffraction is typically 1-5μm, a relatively large defect density can be tolerated, up to 10^5-10^6 dislocations cm^{-3} without significant image overlap. The relatively large incident beam divergence means this technique is not very sensitive to orientation contrast but only to large strain gradients such as those found close to dislocation cores (extinction contrast).

Section Topography (Fig. 2.1b)

This technique uses characteristic radiation in the transmission mode. The incident beam from a point source is highly collimated in the plane of diffraction such that its width is significantly less than the width of the Bormann fan on the exit surface of the sample. The diffracted beam emerging from the back surface of the crystal is allowed to pass through a set of slits and is imaged in the normal way on a high resolution nuclear emulsion plate. The topograph reveals the lattice distortions within the Bormann triangle and is a

useful way of determining the depth of defects in the crystal. Section topography, although limited in the volume of crystal examined, should be regarded as the most fundamental topographic technique since the complex interference patterns seen in extinction contrast are not integrated in volume as is the case in Berg-Barrett and Lang topography.

Lang Topography (Fig. 2.1c)

This technique utilises the same diffraction geometry as section topography. However, in order to image whole crystals, the crystal and film are traversed through the incident beam to produce a section topograph integrated over the whole crystal. It is only necessary to limit the divergence of the beam to avoid simultaneous diffraction of the $K\alpha_1$ and $K\alpha_2$ lines; thus slits are typically hundreds of microns wide. Lang topography and section topography are sensitive to extinction contrast but only to relatively large misorientations due to the large incident beam divergence.

White Radiation Topography

As its name implies, this technique uses white radiation which, in order to be sensitive to orientation contrast, must be highly collimated such as that produced by a synchrotron radiation source. It can be operated in either transmission or reflection and besides the radiation source requires the minimum of equipment. The sample is merely placed in the beam path and because of the white radiation source, diffraction will occur simultaneously from a number of lattice planes allowing the recording of several images on a single photographic plate. This is useful when trying to identify Burgers vectors of dislocations or analysing directional components of other lattice distortions, since it is often necessary to make only one or two exposures.

The high intensity of SR enables real-time dynamic processes to be studied using TV imaging systems. This is particularly useful for studying dislocation

motion during sample stressing or thermal cycling and domain wall movement. The large spaces available in synchrotron experimental stations allow the uncluttered use of cryostats, large magnets, environmental stages and mechanical deformation stages. The high collimation of the incident beam gives this technique a high sensitivity to orientation type contrast but because of the white radiation beam the contrast will be of a different nature to that seen using a characteristic line source, since there will always be another wavelength able to satisfy the Bragg angle defined by a misorientated region. Two misorientated regions will give rise to a line of either increased or decreased intensity depending on the sign of misorientation.

There are two major problems associated with white radiation topography; harmonic contamination and a high background of scattered radiation. The former problem can be overcome for specific reflections by careful choice of diffraction planes and wavelength, such that unwanted higher or lower order reflections are forbidden or of very low intensity. The problem of high background can be reduced by careful collimation and shielding and by the use of filters to eliminate unwanted long wavelength components of the spectrum. The large source to sample distance allows an increased sample to plate distance without significant loss of spatial resolution, and since the scattered intensity will decrease approximately as a function of the distance squared from the sample, the signal to noise ratio on the plate will be increased. Even with the best collimation and shielding, this technique is limited to samples of a few cm^2 in area due to the high levels of background radiation which increase as a function of sample area.

2.2b Multiple Crystal Techniques

Double Crystal Topography

A diagram of a typical diffraction geometry is shown in Fig. 2.2d. This

technique can be used either with a characteristic tube source or an SR source. The first crystal acts, in the case of a tube source, as a collimator and in the case of an SR source as a monochromator. The once-diffracted beam is then diffracted from the sample crystal, either in the transmission or the reflection mode. Since the divergence of the beam incident on the sample crystal is very low and spatially uniform, this technique has a high sensitivity to small long range strains and misorientations, as well as short range lattice distortions.

A further reduction in the divergence and spectral width of the incident beam, and the elimination of harmonic contamination, can be achieved by successive reflections from 'perfect' crystals. Higher collimation increases the sensitivity to strain by enabling diffraction to occur under pseudo plane wave conditions. Several monochro-collimator systems have been developed (refs. 66-70) and it has been possible to reduce the angular divergence of the incident beam to 0.01 arc seconds. However, consideration should always be given to the reduction of usable flux imposed by higher monochro-collimation. A 'perfect' crystal has also been used after the sample crystal to do angularly resolved plane wave x-ray topography (ref. 71) in order to study image formation mechanisms.

2.3 X-ray Sources

For x-ray topography a source of high brilliance is required; high power is needed in order to reduce exposure times and small size to give good spatial resolution. During the production of x-rays by electron impact on a cooled elemental target almost all the electron energy is deposited in the anode in the form of heat and it is the rate of heat dissipation from the anode which limits the maximum flux of the electron beam and, hence, the x-ray output. The above requirement for an x-ray topography source is therefore unattainable and any source must be a compromise between good spatial resolution and short exposure time. The wavelengths available from characteristic line sources are

limited but essentially span the range of wavelengths useful for x-ray topography from Ag Kα at 0.559Å to Cr Kα at 2.289Å. They are, however, severely limited in their power output and the characteristic radiation emitted is almost randomly polarised, which makes exploitation of polarisation properties difficult. A typical sealed tube fine focus x-ray source has a focal spot of 10mmx0.4mm which can be viewed from two orthgonal directions, usually at a take-off angle of 6° from the anode surface. Thus, two effective source sizes are available, 10mm x 40μm and 100μm x 400μm a line and spot source respectively.

Recent years have seen the development of rotating anode sources with good reliability. This has been achieved by the use of turbo-molecular vacuum pumps and ferro-fluid seals on the anode shaft, both of which help eliminate hydrocarbon contamination of the filament and anode so increasing the time between system maintenance shut-downs. Brilliances are up to an order of magnitude greater than their sealed tube counterparts, but even with their improved reliability, rotating anode generators still require more maintenance and involve shut-downs of a few hours to change the anode.

In contrast to electron impact sources synchrotron radiation sources are almost 100% efficient in that almost all of the energy put into the electrons is converted into electromagnetic radiation. They produce typically three orders of magnitude more usable flux than a sealed tube source at the expense of three orders of magnitude more cost. The synchrotron source at Daresbury consists of a 30m diameter ring into which are incorporated 13 beam lines using the radiation from the 1.2T bending magnets and a beam line on the 5T superconducting wiggler magnet. The source operates at an electron energy of 2GeV and a current of typically 200mA. The lifetime of the beam is in excess of 24hrs and under good running conditions a new beam is injected once a day. The radiation from the 1.2T bending magnets is used from the infrared to the short wavelength cut-off of approximately 0.6-0.7Å. The spectrum of radiation

available at the topography station extends from 0.6–0.7Å to 4Å the limit imposed by the Be beam pipe windows. The spectrum is shown in Fig. 2.2 along with the fluxes available from sealed tube sources. In both cases the spectrum is vertically integrated and the bandpass is chosen to match the reflecting range of a typical crystal (imposed by the line width of the characteristic radiation for the tube source, and the first crystal rocking curve width for SR). SR offers a number of other advantages besides intensity over sealed tube sources; the wavelength is continuously variable between the cut-off limits, the beam is polarised in the plane of the electron orbit and the divergence of the beam is small.

The most important aspect of the source as far as the requirements of this study are concerned is the low beam divergence as explained in Section 2.5c. The high intensity is of secondary importance but is useful since exposure times are short, which negates the need for temperature control.

2.4 The Measurement of Lattice Strain and Tilt

This project requires a method to study long range lattice distortions and their relation to the defect structure in semi-insulating LEC GaAs. Initial topographic investigations indicated that lattice tilts and strain were both present in this material (see chapter 3). A method was thus required to distinguish between and measure these two components of any long range lattice distortion. X-ray diffraction is the only technique with the strain sensitivity necessary to measure both of the above parameters.

The most commonly used method for measuring lattice parameter is the Bond method (ref. 72). A highly collimated beam of characteristic x-rays is used to measure the angular separation between two diffraction peaks and permits determination of the absolute lattice parameter to a precision of 1 part in 10^6.

Each measurement relates only to the area of sample covered by the incident beam and lattice parameter maps can only be obtained by making measurements at different positions on the sample. Since each measurement may take tens of minutes, to map a 50mm diameter wafer would take several hours. The thermal expansion coefficient of GaAs is $6x10^{-6}{}^{\circ}C^{-1}$ so careful control of temperature is required throughout the whole experiment. This method can also provide information on tilt but with limited precision and only with the use of a stable X–Y scanning stage.

Various multiple crystal techniques have been developed (ref. 73) which permit absolute or relative lattice parameter measurements to a precision of typically a few parts in 10^8. Most methods involve the measurement of the angle separating two reflections from the same atomic planes or the angular difference between reflections from the standard crystal and the sample crystal. They all measure lattice parameters at a single point on the sample and repeated measurements using a scanning stage must be taken in order to produce a map of lattice parameter. This, again, is a very lengthy business and would be accompanied by problems of temperature and diffractometer stability, and would yield little information on lattice tilts.

The methods considered above use well collimated incident beams and rely on the measurement of Bragg angles using a detector rather than photographic film. They are good for studying homogeneous samples but are time–consuming and difficult to operate if maps of large inhomogeneous samples are required. Topographic techniques permit rapid measurement of relative lattice parameter and lattice tilt over large samples, as described below.

Most single crystal topographic methods are only sensitive to short range strain gradients as discussed previously. However, a technique has been used by Scott (ref. 74) which uses SR radiation at a wavelength corresponding to a strong

absorption edge of one of the elements in the sample crystal. In a crystal containing long range lattice distortions the wavelength of the diffracted x-rays from a point in the crystal will depend on the lattice parameter and lattice tilt at that particular point. At the absorption edge wavelength there is a sharp change in diffracted intensity which shows up clearly on a topograph even in the reflection geometry. Thus, if topographs are taken at a series of incident angles, images of the absorption edge sweeping across the deformed sample will be obtained. The topographs can then be combined to form a Bragg angle map of the crystal. If a second Bragg angle map is obtained with the sample rotated by 180° about an axis defined by the diffraction vector, it is possible to split the Bragg angle map into its strain and tilt components. The strain sensitivity of this technique is limited by the 'width' of the absorption edge, which for Ga is approximately 5eV (ref.75). This corresponds to a relative energy and thus relative wavelength spread of $\Delta\lambda/\lambda = 4.8\times10^{-4}$. The change in contrast across the absorption edge will thus occur over a relative lattice parameter change of $\Delta d/d = 4.8\times10^{-4}$ which sets a lower limit on the minimum strain that can be measured without making densitometry measurements on the film. The lattice tilt sensitivity is determined by the differential of Bragg's law

$$\Delta\theta = \frac{\Delta\lambda}{\lambda} \tan\theta \qquad (2.1)$$

which for the specified absorption edge width and a Bragg angle of 10°, is approximately 17 arc seconds. However, for the larger Bragg angles required for reflection work (θ>45°) the tilt sensitivity would be >100 arc seconds. Preliminary investigations suggested that distortions present over 50mm LEC GaAs are smaller than the sensitivity of this technique which therefore excludes it as a tool for this work. Being a white radiation technique, it would also cause problems due to the high background intensity, especially when using large crystals up to 50mm in diameter.

Double crystal topography can be used to measure long range lattice distortions in much the same way as the white radiation technique described above. If the beam incident on the sample crystal approximates to a plane wave and a high order reflection with a sharp rocking curve is used, then for a distorted sample crystal a narrow diffraction band will be observed in much the same way as the technique described above. The sensitivity will be better than the white radiation technique since the contrast change down the flank of a sharp rocking curve can occur over <1 arc second. It has the advantage that the background is low and large samples can be examined. The high intensity of an SR source enables the experiments to be carried out in a short time, thus making temperature control much easier. Great care must be taken, however, to ensure that the beam incident on the sample crystal approximates to a plane wave as closely as possible. A discussion of the x-ray optics of double crystal topography is presented in the next section, with particular reference to beam uniformity problems that must be addressed in order to achieve high strain and tilt sensitivity over a long spatial range.

2.5 Double crystal topography

The use of double crystal topography was first reported by Bond and Andrus in 1952 (ref. 76) and later developed by Bonse and Klapper in 1958 (ref. 77), who used the non-dispersive +- setting to detect long range strain variations. Since then many authors have developed variations on this technique to study long and short range strains in a variety of materials, particularly semiconductors and quartz (ref. 78). The high sensitivity to both long and short range strains stems from the high collimation of the beam incident on the sample crystal. However, strain sensitivity depends on the diffraction geometry used and varies markedly from case to case. The simplest way of understanding the strain sensitivities of the different settings is via the Du Mond diagram. The first part of this discussion assumes a characteristic line source is being used; the

discussion is later broadened to include an SR source, specifically station 7.5 at the SERC's SR source at Daresbury, UK.

2.5a Du Mond diagrams

The Du Mond diagram named after its inventor provides a semi-quantitative representation of the diffraction conditions in multiple crystal diffractometry. Assume a perfect crystal diffracting x-rays according to Bragg's law over an angular width $\Delta\theta$ defined by dynamical diffraction. If wavelength is plotted against Bragg angle then the conditions for which diffraction occurs lie in a narrow band of angular width $\Delta\theta$. The radiation diffracted from the first crystal of a double crystal diffractometer thus lies in this band but the spectral width is limited by the line width $\Delta\lambda/\lambda$ of the characteristic source being used. The diffraction conditions for the sample crystal can then be plotted on the same diagram for the three different diffraction geometries, the parallel non-dispersive setting, the ++ setting and the +- dispersive setting.

For the +- non-dispersive setting (fig. 2.3a) the planar spacing of the diffraction planes is the same for both crystals, the λ versus θ curves thus coincide. Diffraction can therefore occur for any wavelength if both crystals are parallel (thus the naming of this setting +- non-dispersive); in practice the angular range of the once diffracted beam is limited by the line width of the tube source. The high strain sensitivity of this setting can thus be understood since any slight change in planar spacing or tilt will move the sample crystal curve to higher or lower theta and result in only a partial overlap in the diffracting regions and thus a change in diffracted intensity. The non-dispersive nature of this geometry can be inconvenient when using a Kα line since both α_1 and α_2 components will diffract simultaneously at slightly different Bragg angles and produce two slightly misplaced images on the photographic plate.

Now consider the ++ setting shown in fig. 2.3b. Again the angular and spectral width of the once-diffracted beam is shown along with that for the sample crystal. Here the sample crystal curve is reversed since an increase in incidence angle on the first crystal corresponds to a decrease on the second crystal. If there is a small misorientation or strain in the sample crystal, the diffracted intensity will remain constant so long as the Bragg angle stays within the limits θ_1 and θ_2 defined by the spectral width of the once-diffracted beam. The strain sensitivity of this geometry is thus significantly less than the +- case and makes it more suitable for studying lattice defects rather than small long range strains or misorientations.

The geometry of the +- dispersive setting is shown in fig. 2.3c and is the most commonly used setting since, especially for III-V and II-VI compounds, it is not usually possible to obtain defect-free reference crystals of the sample crystal material. It is usual in these situations to use Si or Ge as a reference crystal. From the differential of Bragg's law (eqn. 2.1) the angular width $\Delta\theta_1$ of the once-diffracted beam is given by the line width of the source $\Delta\lambda/\lambda$

$$\Delta\theta_1 = \frac{\Delta\lambda}{\lambda} \tan\theta_1 \qquad (2.2)$$

where θ_1 is the Bragg angle of the first crystal. The angular width of acceptance of the sample crystal is similarly given by

$$\Delta\theta_2 = \frac{\Delta\lambda}{\lambda} \tan\theta_2 \qquad (2.3)$$

Thus the sample crystal may be rocked by an angle

$$\Delta\theta_2 - \Delta\theta_1 = \frac{\Delta\lambda}{\lambda} (\tan\theta_2 \mp \tan\theta_1) \qquad (2.4)$$

before a loss of intensity is observed. Where the - and + sign correspond to

the +− and ++ settings respectively, this may be regarded as an effective increase in rocking curve width of the sample crystal and consequently a lowering of the long range strain sensitivity. At angles below 45°, if the Bragg angle difference between the two crystals is only 3 or 4 degrees, the effective increase in rocking curve width is less than 10 arc seconds so the strain sensitivity is still high. One advantage of the dispersive setting is that diffraction of the α_1 and α_2 components no longer occurs for the same angular setting of the sample crystal and topographs are not confused by partially overlapping α_1 and α_2 images.

When using an SR source the limitations on the spectral and angular widths of the incident beam are significantly different. The angle subtended by the source at the sample in the plane of diffraction is only 4×10^{-6}rad (0.8 arc seconds) so the spectral width of the once-diffracted beam is limited by the beam divergence rather than the spectral width of the source. The spectral width of the once-diffracted beam is given by $\Delta\theta_S/\tan\theta$ where $\Delta\theta_S$ is the angle subtended by the source in the plane of diffraction at the monochromator crystal. The effective broadening of the sample rocking curve is thus

$$\Delta\theta = \Delta\theta_S \left[\frac{\tan\theta_2}{\tan\theta_1} \pm 1\right] \qquad (2.5)$$

Since $\Delta\theta_S$ is small for SR it is far less important to limit the difference in Bragg angle between the two crystals and consequently the +− dispersive setting has a higher strain sensitivity when used on an SR source. This effect can be seen in fig. 2.4 which shows two rocking curves taken in the same dispersive setting. A 440 surface symmetric reflection from an Si crystal was used for the first reflection (θ_B = 53.35) and a 440 reflection from a <111> orientated GaAs crystal for the second crystal (θ_B = 50.43). Curve (a) is taken on a conventional Cu source and (b) on an SR source at the same wavelength. For the Cu conventional tube source the collimation was sufficient to exclude

simultaneous diffraction of both $K\alpha_1$ and $K\alpha_2$ components. From eqns. 2.4 and 2.5 the effective broadening of the conventional tube and SR sources are 11.05 arc seconds and 0.08 arc seconds respectively and their experimentally measured half widths 19.7±0.2 arc seconds and 12.4±0.2 arc seconds respectively. The tube source rocking curve broadening due to the spectral width of the source must be added in quadrature to that of the SRS width, assuming that the diffraction profiles approximate to gaussians. This then gives the expected tube source rocking curve width of 16.6 arc seconds. The slit size used on the tube source experiment was four times that used on the SRS and since the sample was slightly curved (as seen on the double crystal topographs and the SRS rocking curve which is slightly broadened), this explains the discrepancy between the experimental and predicted widths.

2.5b Vertical beam divergence

The Du Mond diagram is only applicable to a beam with zero divergence in the plane normal to the plane of diffraction. In practice this is never achieved and particularly for a conventional tube source the divergence is high. Consider Bragg diffraction from a characteristic point source. Diffraction will occur over an annular region on the crystal surface defined by the intersection of the diffraction cone and the crystal surface (fig.2.5). The width of the annular region is defined by the spectral width of the source and the rocking curve width of the crystal. Two diffraction cones will exist, one for the radiation diffracted from the first crystal and one for diffraction from the sample crystal. Only when the intersection of these two cones coincides with the sample surface will diffraction occur from the sample crystal (fig. 2.5). If the Bragg angle of both crystals is the same (ie the vertex angles of the two cones are equal) then diffraction will occur from the whole annular region so long as the two crystals are parallel. Thus the image height in the +- non-dispersive case is only limited by the diameter of the diffraction cone which can be increased by

increasing the source to sample distance. If the two crystals are tilted with respect to one another, the projection of the first crystal cone on the sample crystal surface becomes elliptical, the image height is restricted to the area of overlap and the diffraction conditions vary as a function of height on the sample crystal. A theoretical treatment of the effects of vertical divergence was first presented by Swartschild in 1928 (ref. 79) but a more complete treatment has since been undertaken by a number of authors (refs. 80, 81). Fig. 2.6 shows the effect of sample tilt on image height in the +− non−dispersive setting based on the equations developed by Yoshimura (ref. 80). The graphs show a plot of vertical height against the deviation from Bragg angle of the second crystal for a number of different tilt angles (assuming diffraction in the horizontal plane). The three curves, W = −1, 0, +1, represent the two extremes and centre of the sample crystal reflection peak. Moving along a line parallel to the x−axis at a particular height represents a measurement of the rocking curve at that height. A line parallel to the y−axis represents the image height between the limits $-1<W<1$. Graph (a) represents the case for a typical laboratory source and graph (b) the case for an SR source. This clearly demonstrates the necessity for tilt control on double crystal diffractometers used on tube sources and the lack of tilt control required for those on SR sources.

For the +− dispersive setting, the vertex angles of the diffraction cones are different and therefore the maximum image height will always be limited by the vertical beam divergence and the difference in Bragg angle of the two crystals. Graphs of vertical height on the sample crystal against deviation from the Bragg angle are also shown for this geometry in fig. 2.7. For a tube source (source to sample distance 0.5m) using a strong, broad asymmetric reflection such as that which might be used to image lattice defects, the image height has a maximum of approximately 50mm. For the same diffraction geometry on an SR source the maximum image height is 3.9m! For a high order narrow reflection such as that which might be used for studying long range strains, the

tube and SR source maximum heights are respectively 26mm and 1.26m and, as can be seen from fig. 2.6, the tube source image is very sensitive to sample crystal tilt. In order to image a whole 50mm wafer using a tube source it would be necessary to have a minimum source to sample distance of 1m which would lead to lengthy exposures. Besides this there would be an effective Bragg angle change between the top and centre of the crystal corresponding to the rocking curve width of the sample crystal, plus the dispersion broadening. For an SR source the corresponding change of diffraction conditions over the height of a 50mm wafer is less than 0.1 arc seconds.

A fundamental requirement for measuring long range strains is that the beam incident on the sample crystal is uniform and approximates to a plane wave. For a conventional tube source, because of the high vertical beam divergence, this is clearly not the case and the effective Bragg angle varies as a function of the vertical height on the sample and as a function of sample tilt. For a synchrotron source the vertical beam divergence is two orders of magnitude lower, which results in a much more uniform pseudo plane wave of x-rays incident on the sample crystal. It is therefore necessary to use an SR source if accurate measurements are to be made of small lattice distortions amounting to strains of a few parts in 10^5 and tilts of a few tens of arc seconds over a large sample (eg 50mm in diameter). The high intensity of the SR source is also useful since many topographs must be taken to form a detailed Bragg angle map and thermal stability must be maintained over this period.

c. Lattice strain and tilt measurements

The double crystal topographic technique used to measure the lattice distortions in GaAs is similar to that reported by Kikuta et al (ref. 82) to study lattice distortions in bent Si crystals. The simple theory of the technique is shown below, first for the case of a plane wave, then further developed to account for

beam divergence in the diffraction plane and the non-dispersive setting.

Consider surface symmetric Bragg diffraction of a plane monochromatic wave occurring from a single crystal slice of material which has small variations of lattice strain and tilt (fig. 2.9). Let the lattice spacing of the diffracting planes at position r on the slice be d(r) and the Bragg angle of the diffracting planes at an arbitrary reference point r_o be θ_o. Let the angle of tilt, measured in the plane of diffraction between the diffraction planes at r_o and those at r be $\Phi(r)$. Then Bragg's law position r can be written as

$$\lambda = 2d(r)\sin(\theta_o + \Phi(r) + \rho_1(r)) \tag{2.6}$$

where $\rho_1(r)$ is the angle through which the crystal must be rotated to move the diffracting region from position r_o to position r. If the crystal is now rotated through 180° about an axis defined by the diffraction vector g, then the angle $\Phi(r)$ changes sign with respect to the incident beam direction and we may write

$$\lambda = 2d(r)\sin(\theta_o - \Phi(r) + \rho_2(r)) \tag{2.7}$$

Thus, by combining these two equations, the lattice tilt and lattice parameter at position r relative to those at position r_o may be written respectively as

$$\Phi(r) = \frac{\rho_2(r)-\rho_1(r)}{2} \tag{2.8}$$

and

$$\frac{\Delta d(r)}{dr_o} = \frac{-(\rho_1(r) + \rho_2(r))}{2\tan\theta_o} \tag{2.9}$$

$\rho_1(r)$ and $\rho_2(r)$ are measured by taking two series of topographs at a succession of angular settings to produce a Bragg angle map for each 180° rotation about the diffraction vector. The precision of $\Phi(r)$ and $\Delta d(r)/dr_o$ will depend on the

angular increment used in obtaining the Bragg angle map, ie on the precision of $\rho_1(r)$ and $\rho_2(r)$. It is therefore important to use a narrow high order reflection in order to ensure sharp contrast changes so that small angular increments can be used when measuring the Bragg angle maps.

An added advantage of this technique is its insensitivity to temperature variations. Since relative lattice parameters are measured it is only necessary that the sample is of uniform temperature and temperature variations between consecutive measurements are inconsequential. This alleviates the requirement for a temperature controlled environment and it is only necessary to shield the sample from draughts and temperature variations on a timescale comparable with that required to measure a Bragg angle map.

The above derivation assumes a plane monochromatic wave but in practice for SR there is a beam of low divergence from a distant source as described below. Consider diffraction relative to that from a central reference point on a monochromator crystal. In the direction on the crystal surface, normal to the plane of diffraction, conditions have been discussed in section 2.5b and for SR remain essentially constant across a 50mm diameter sample crystal. In the perpendicular direction (parallel to the plane of diffraction in the crystal surface) the wavelength of the diffracted beam varies as a function of distance from the central point and imposes variations in diffraction conditions for the sample crystal. Consider the situation shown in fig. 2.10 for an asymmetric reflection from a monochromator crystal, a distance s from the SR source. The variation in Bragg angle as a function of distance x is given by

$$\Delta\theta_1 = \frac{-x\beta}{s} \qquad (2.10)$$

where $\beta = \dfrac{\sin(\theta-\Psi)}{\sin(\theta+\Psi)}$

Ψ = angle between the diffracting planes and the crystal surface

The corresponding variation in wavelength of the diffracted radiation is given from eqn. 2.1 as

$$\frac{\Delta\lambda_1}{\lambda} = \frac{\Delta\theta_1(x)}{\tan\theta_1} = \frac{x\beta}{s\tan\theta_1} \qquad (2.11)$$

where λ is the wavelength of the diffracted radiation from the central reference point. So the variations in wavelength $\Delta\lambda/\lambda$ and direction $\Delta\theta_1$ of the radiation incident on the sample crystal are given by eqns. 2.10 and 2.11 respectively. Given that the variation in wavelength is $\Delta\lambda_1/\lambda$ then the requirement for diffraction from the sample crystal is

$$\begin{aligned}\Delta\theta_2 &= \frac{\Delta\lambda_1}{\lambda}\tan\theta_2 \\ &= -\frac{x\beta}{s}\frac{\tan\theta_2}{\tan\theta_1}\end{aligned} \qquad (2.12)$$

However, the variation in incidence angle as a function of x is determined by the monochromator crystal and is given by eqn. 2.10. So the deviation from the exact Bragg reflection condition on the sample crystal as a function of x is given by

$$\Delta\theta = \Delta\theta_1 - \Delta\theta_2 = \frac{x\beta}{s}\left[1 - \frac{\tan\theta_2}{\tan\theta_1}\right] \qquad (2.13)$$

Putting the above expression into equations 2.6 and 2.7 yields, respectively,

$$\lambda = 2d(r)\sin(\theta_0+\Phi(r)+\rho_1(r)-\Delta\theta)$$

and (2.14)

$$\lambda = 2d(r)\sin(\theta_0-\Phi(r)+\rho_2(r)+\Delta\theta)$$

which in turn gives an expression identical to eqn. 2.9 for the strain but yields for the relative lattice tilts

$$\Phi(r) = \frac{(\rho_2(r)-\rho_1(r))}{2} + \Delta\theta \qquad (2.15)$$

The value of $\Delta\theta$ across the diameter of a 50mm wafer for the diffraction geometry used to measure the lattice distortions in GaAs (800 reflection from <110> orientated Si monochromator, 800 reflection from <100> orientated GaAs sample, λ = 1.2Å) is 6 arc seconds. Since the lattice tilts present in the material could typically amount to 100 arc seconds, this correction is ignored for most of the samples studied. It would, however, be significant for more uniform samples with smaller lattice tilts.

d. Reference crystal perfection

Double crystal topographs are essentially a superposition of topographs of the reference crystal and the sample crystal. When using a tube source defects present in the reference crystal are not normally visible on the topograph because of the large distance from the first crystal to the photographic plate relative to the distance from the first crystal to the source. This results in a very poor spatial resolution for images from the first crystal. For a typical source to first crystal distance and first crystal to plate distance of 0.25m and 0.25m respectively the resolution in the vertical and horizontal planes is 400μm and 70μm respectively. Thus only large scale non-uniformities would be visible on the topograph but there would be a loss of strain sensitivity due to an increase in the divergence of the beam incident on the sample. When using a synchrotron source, however, the resolution from the reference crystal in the directions parallel and normal to the diffraction plane on the photographic plate is 3μm and 0.15μm respectively, principally because of the very small beam divergence. Thus, for SR topography a reference crystal which is homogeneous over both long and short ranges is essential. This phenomenon was observed on the Daresbury SR source when using a double crystal Si monochromator (ref. 23) to topograph a <111> orientated GaAs crystal. Fig. 2.11a shows a topograph taken using the above monochromator and fig. 2.11b a topograph of

the crystal with the same reflection taken using a tube source and Si reference crystal. The only feature clearly seen on both topographs is the scratch in the top right-hand corner. The dislocation images clearly visible in (b) are present in (a) but without direct comparison of the two topographs it would be difficult to ascribe these images in (a) to dislocations. The growth striations clearly visible in (b) are totally obscured in (a) by the contrast ascribed to the damage in the monochromator.

Topographs taken of the output beam from the monochromator are shown in figs. 2.11c and d. The two topographs were taken for different sample-to-plate distances. The difference in the two images indicates that the contrast arises from orientation type contrast since changes in the image can only occur if rays are travelling in different directions. (The spatial resolution in the vertical direction is such that on both topographs it is almost an order of magnitude less than the resolution of the photographic plate.) The size of the damage features in (a) is larger than in (c) or (d) because of the asymmetric reflection used from the GaAs crystal which expands the beam. The effects of orientation contrast are slightly different on an SR source compared with a characteristic line source. Consider the double crystal arrangement shown in fig. 2.12 with a reference crystal containing a small misorientated region. On an SR source the diffracted beam from the misorientated region diverges from the normally diffracted beam by an angle of $2\delta\theta$ where $\delta\theta$ is the misorientation angle. If the angle $\delta\theta$ is significantly less than the rocking curve of the sample crystal, then the misorientated beam will still diffract from the sample crystal but will be spatially misplaced as shown in fig. 2.12. Thus there is a significant misplacement contrast as well as a misorientation contrast. On a tube source the diffracted beam from the misorientated region would diverge from the normally diffracted beam by an angle of $\delta\theta$ and the misplacement contrast would be less significant, besides being blurred by the poor spatial resolution from the first crystal. The above situation is much simplified since the SR

beam has a finite divergence and misorientations may be continuous rather than step functions. Nevertheless, fig. 2.11 clearly shows both that this effect occurs and the importance of monochromator perfection for SR work.

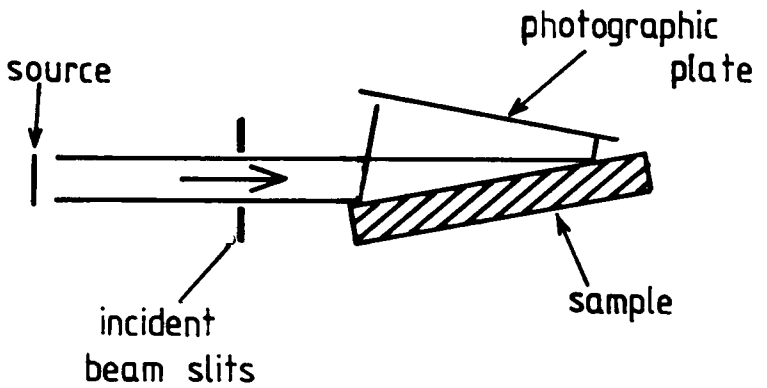

Fig.2.1a: Line diagram showing the diffraction geometry of Berg Barrett topography

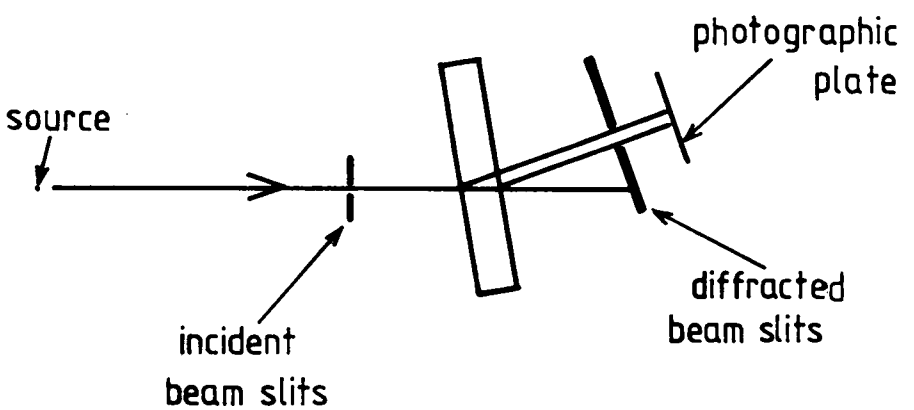

Fig. 2.1b: Line diagram showing the diffraction geometry of section topography

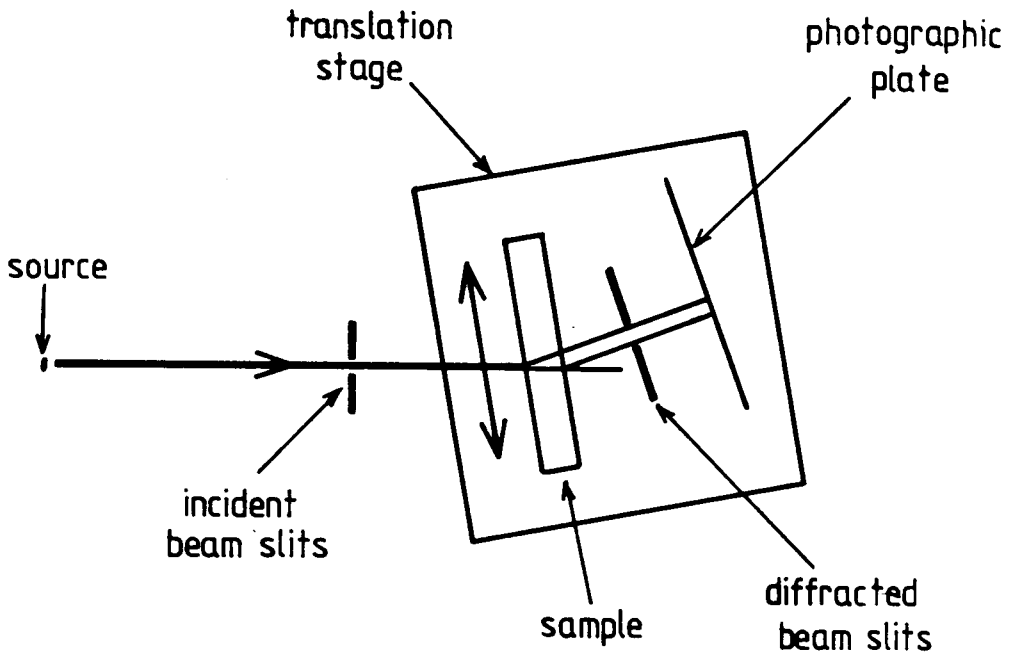

Fig. 2.1c: Line diagram showing the diffraction geometry of Lang topography

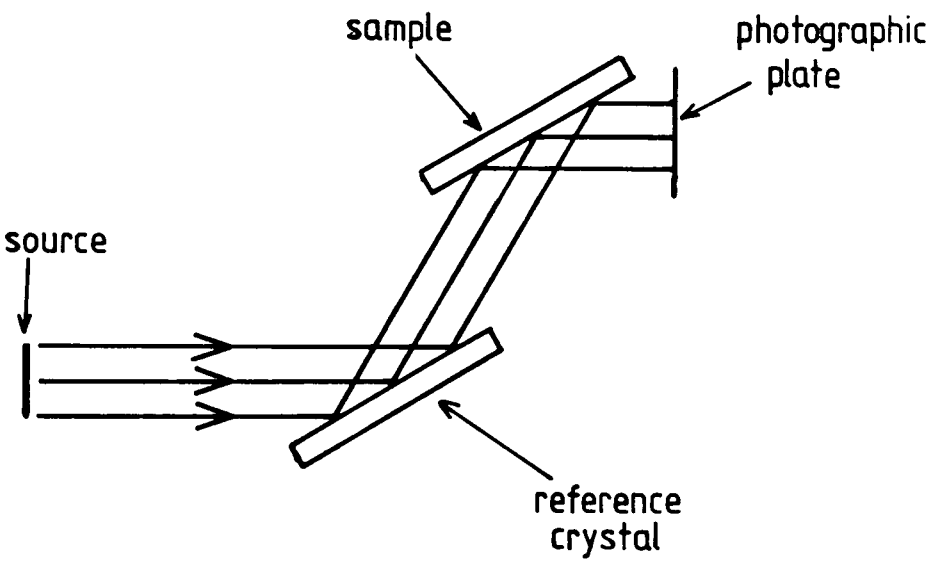

Fig. 2.1d: Line diagram showing the diffraction geometry of double crystal topography in the +− case

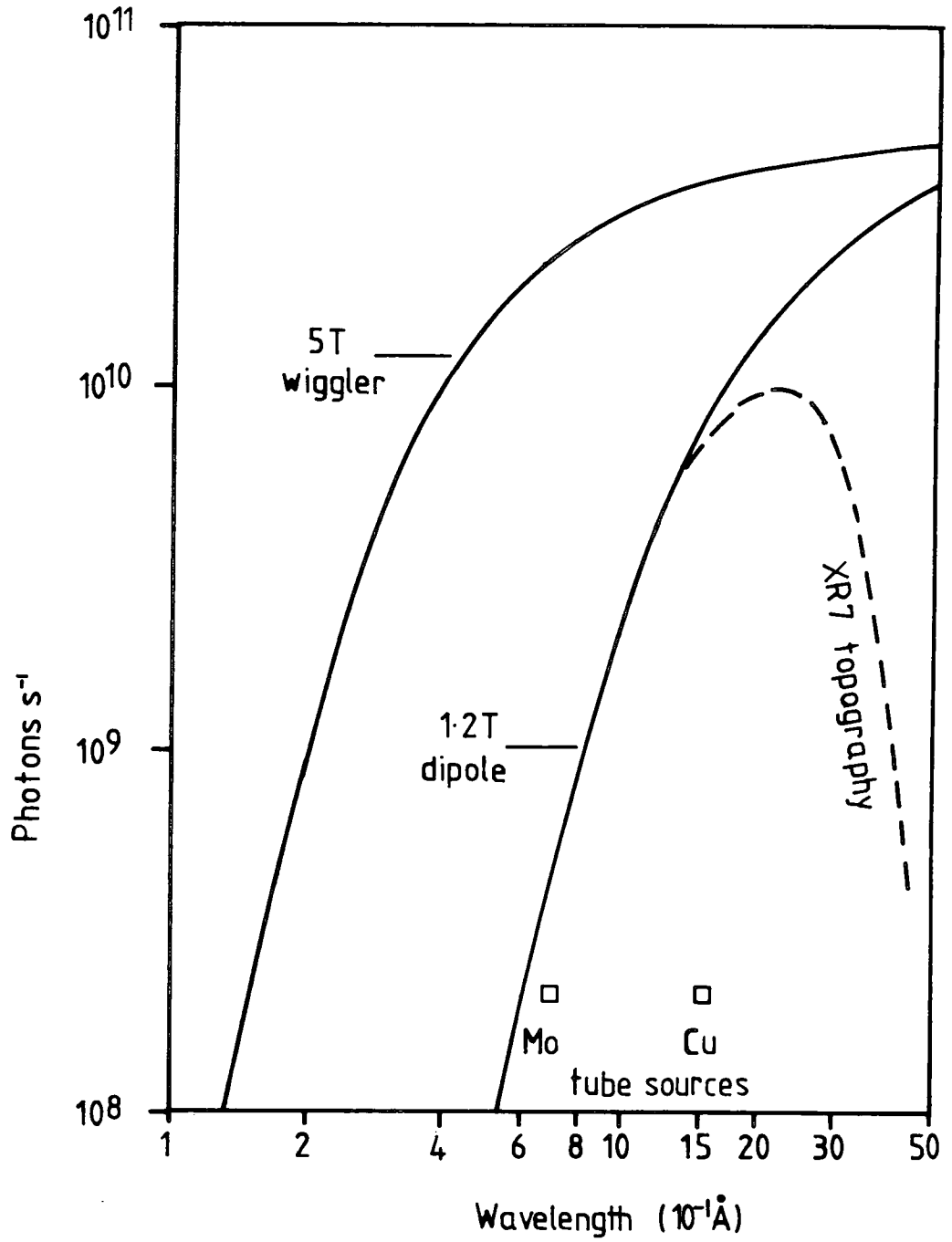

Fig. 2.2: Radiation spectrum from the standard 1.2T dipole bending magnet on the Daresbury synchrotron radiation source shown relative to some standard electron bombardment sources. In both cases the spectra are vertically integrated and the bandpass is chosen to match the reflecting range of a typical crystal.

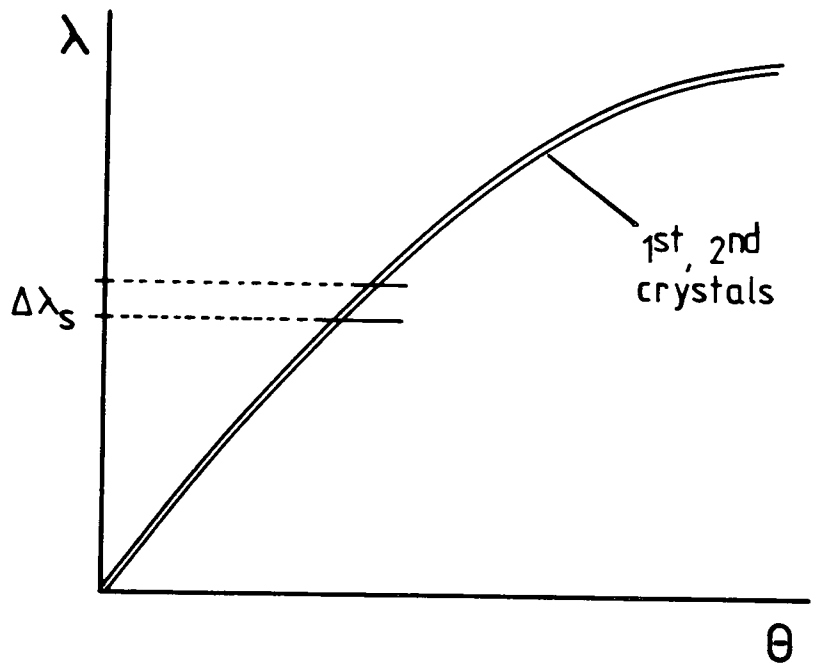

Fig. 2.3a: Du Mond diagram for the +− non-dispersive diffraction geometry

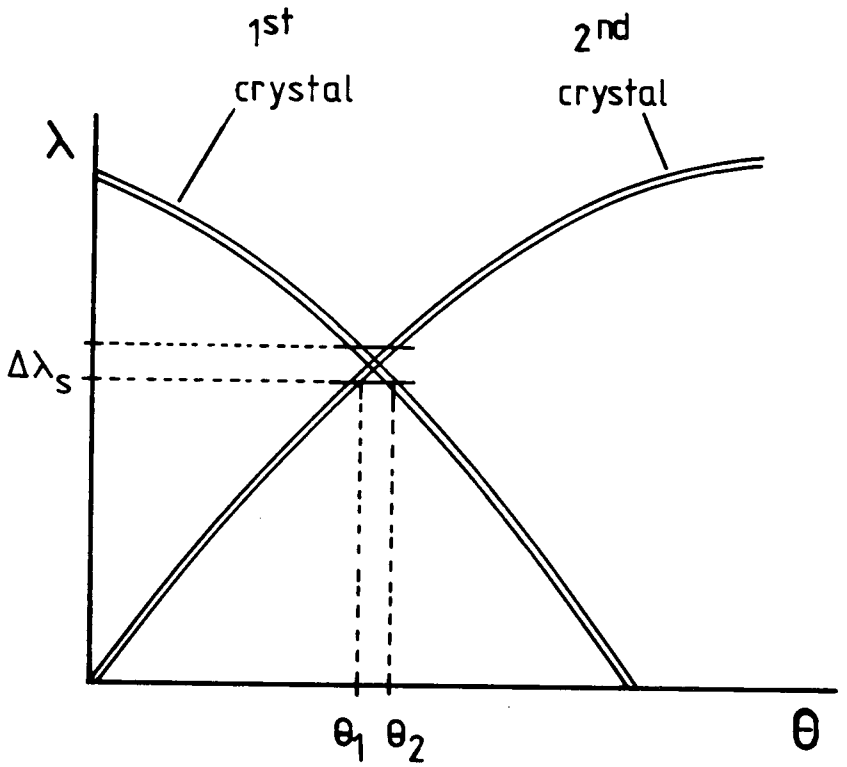

Fig. 2.3b: Du Mond diagram for the ++ diffraction geometry

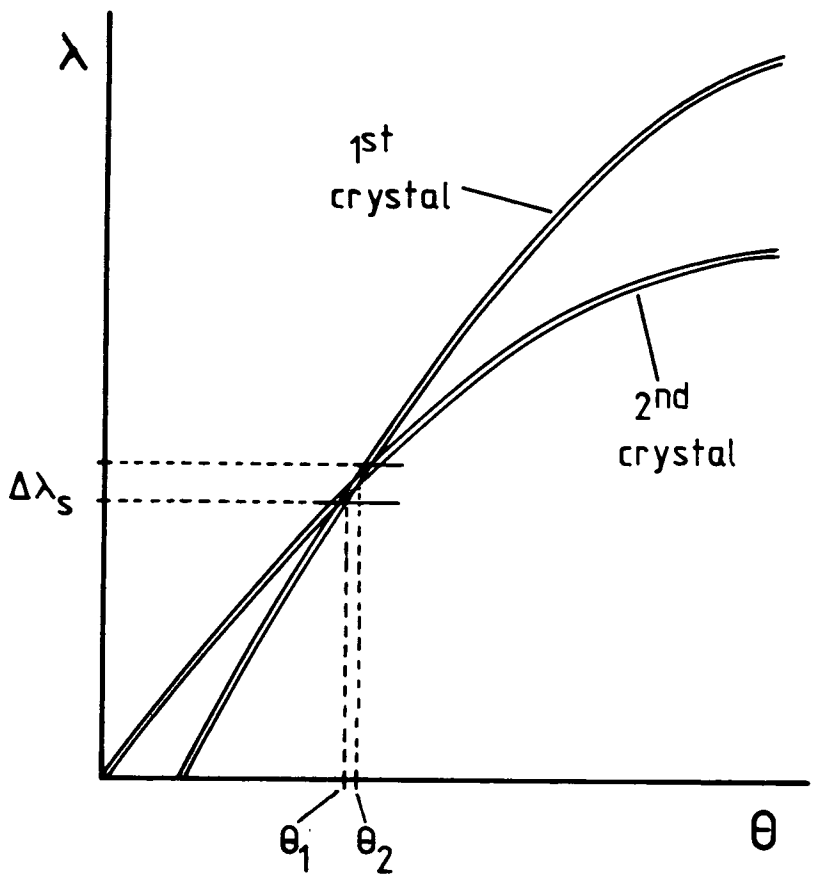

Fig. 2.3c: Du Mond diagram for the +− dispersive diffraction geometry

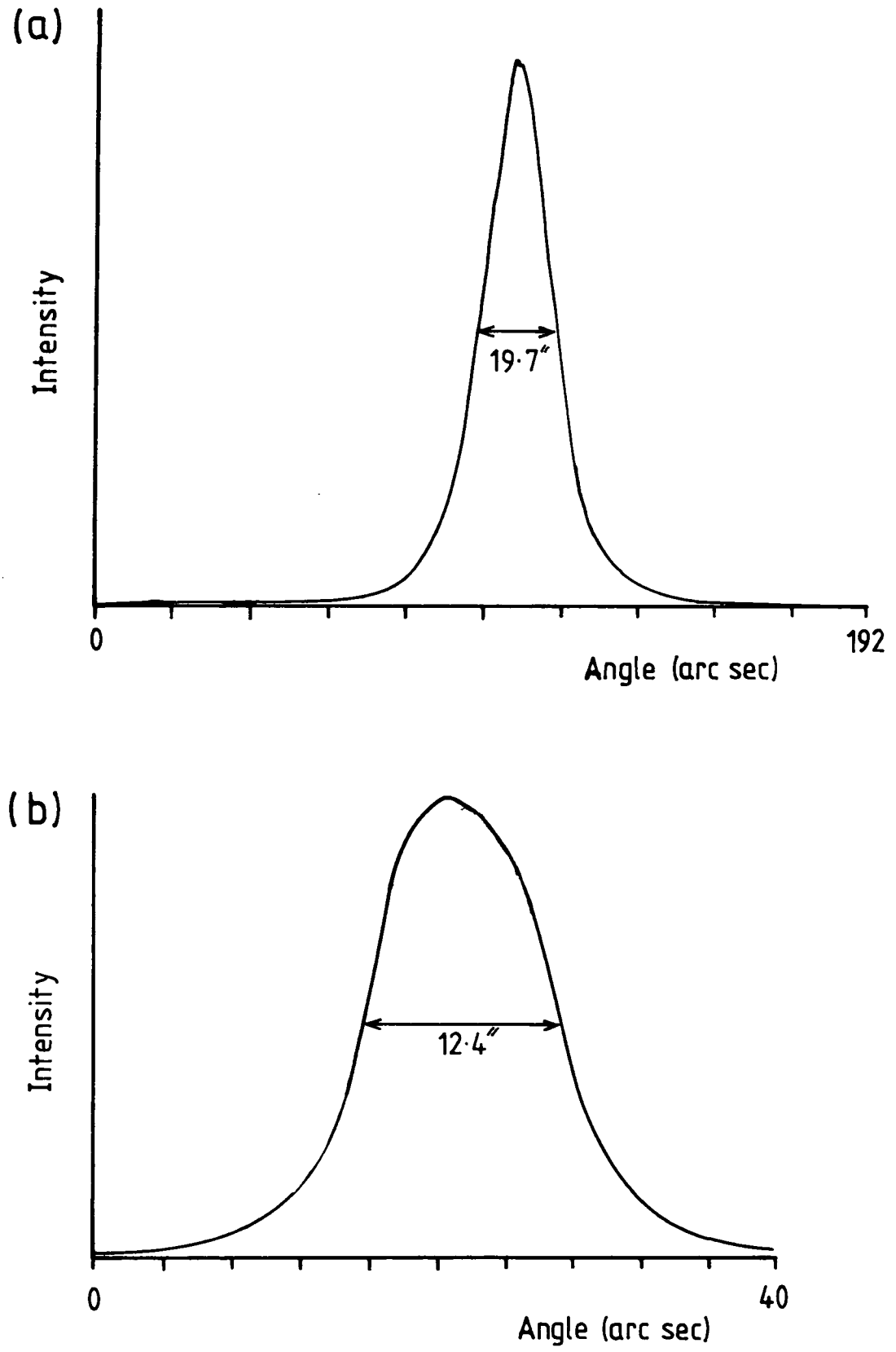

Fig. 2.4: Double crystal rocking curves using the 440 reflection from a <111> orientated GaAs sample at 1.54A with a Si 440 surface symmetric monochromator reflection: a) taken on a conventional tube source; b) taken on a SRS

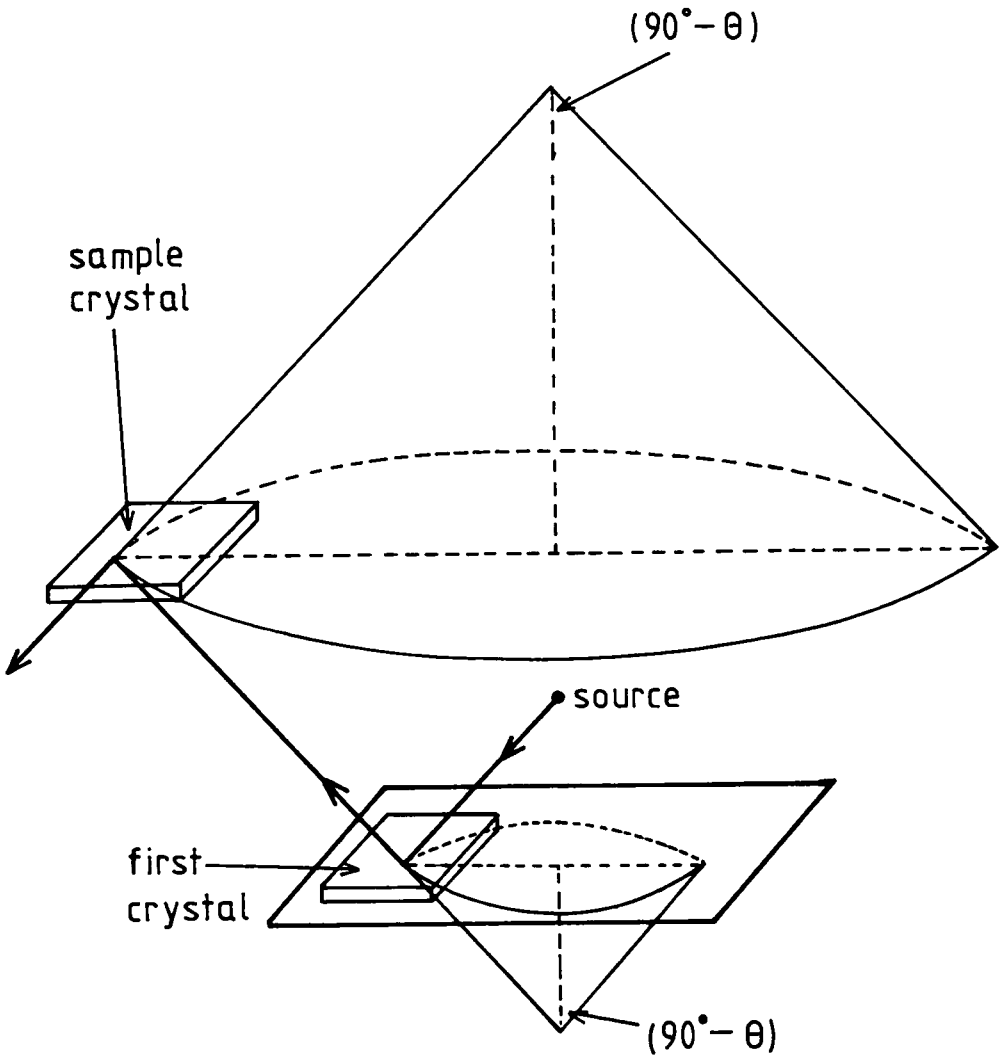

Fig. 2.5: Diagram showing the intersection of monochromator and sample diffraction cones in the non-dispersive geometry

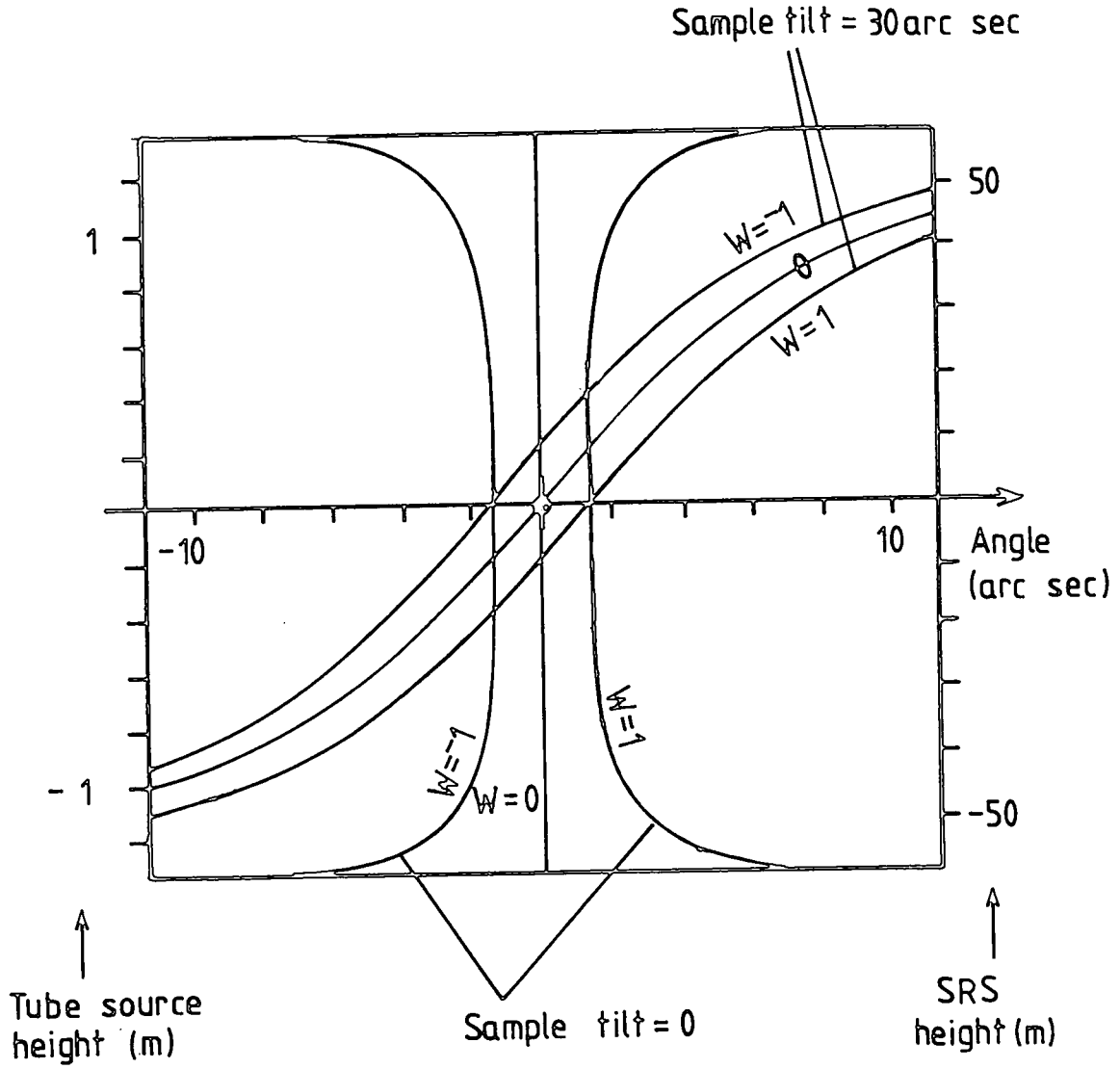

Si 333 reflection
Cu $K\alpha_1$

Fig. 2.6: Graphs of vertical height against deviation from the Bragg angle for conventional tube source and SRS +- non-dispersive geometry

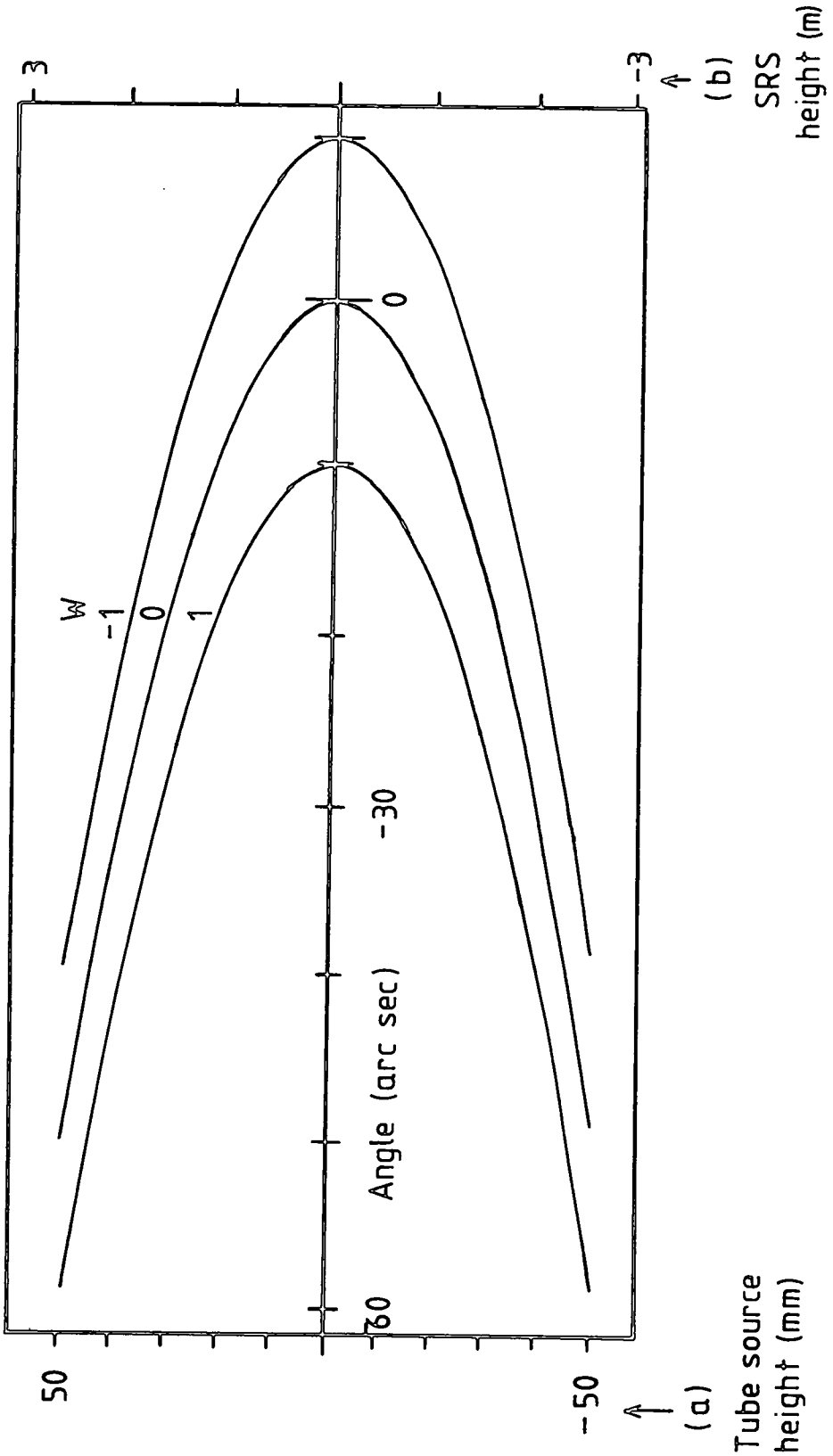

Fig. 2.7: Graphs of vertical height against deviation from the Bragg angle, for the 422 reflection from <100> orientated GaAs at 1.54A a) for a conventional tube source and b) for an SRS

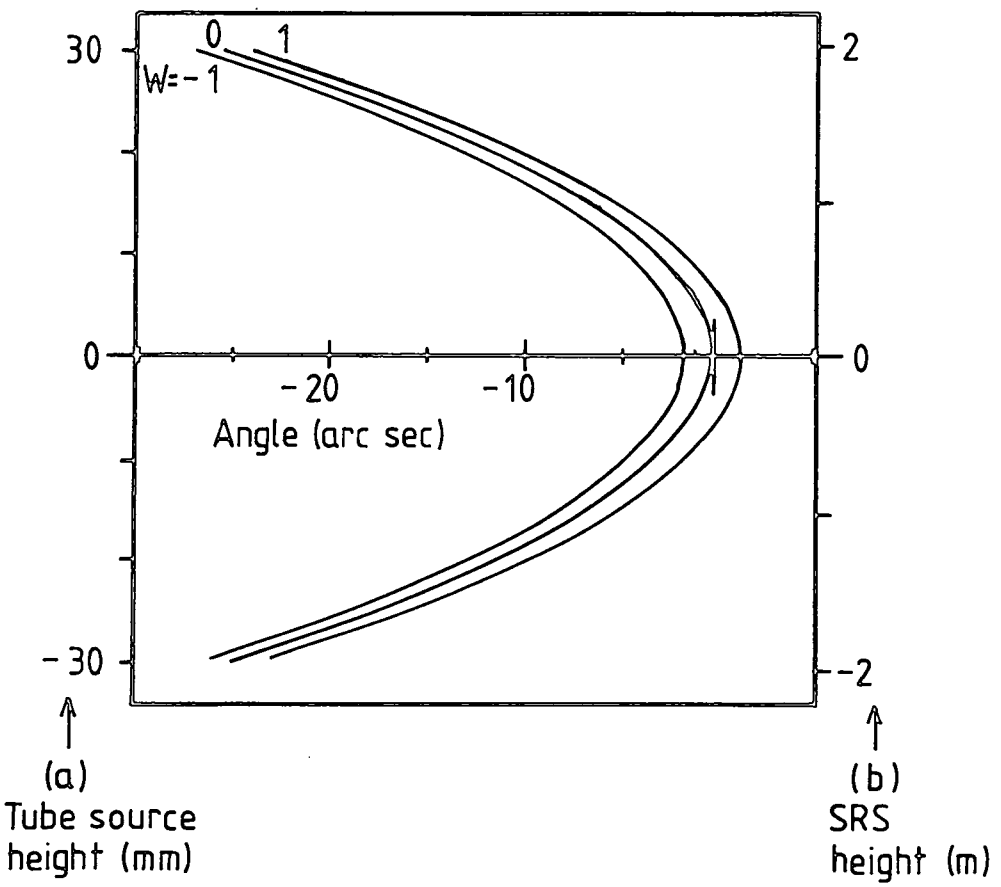

Fig. 2.8: Graphs of vertical height against deviation from the Bragg angle for the surface symmetric 800 reflection from GaAs at 1.2A a) for a conventional tube source and b) for an SRS

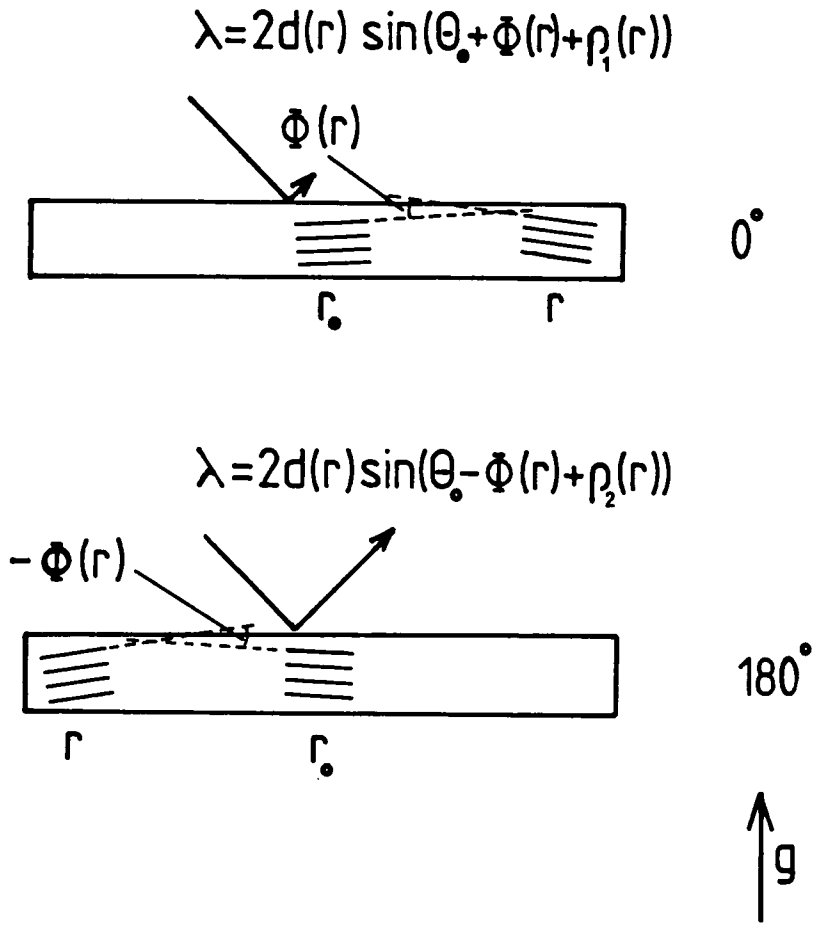

$$\Phi(r) = \frac{\rho_2(r) - \rho_1(r)}{2}$$

$$\frac{\Delta d}{d} = \frac{-(\rho_2(r) + \rho_1(r))}{2 \tan \theta}$$

Fig. 2.9: Diagram of diffraction geometry of a crystal containing lattice distortions for the two 180° rotations of the sample about the diffraction vector g

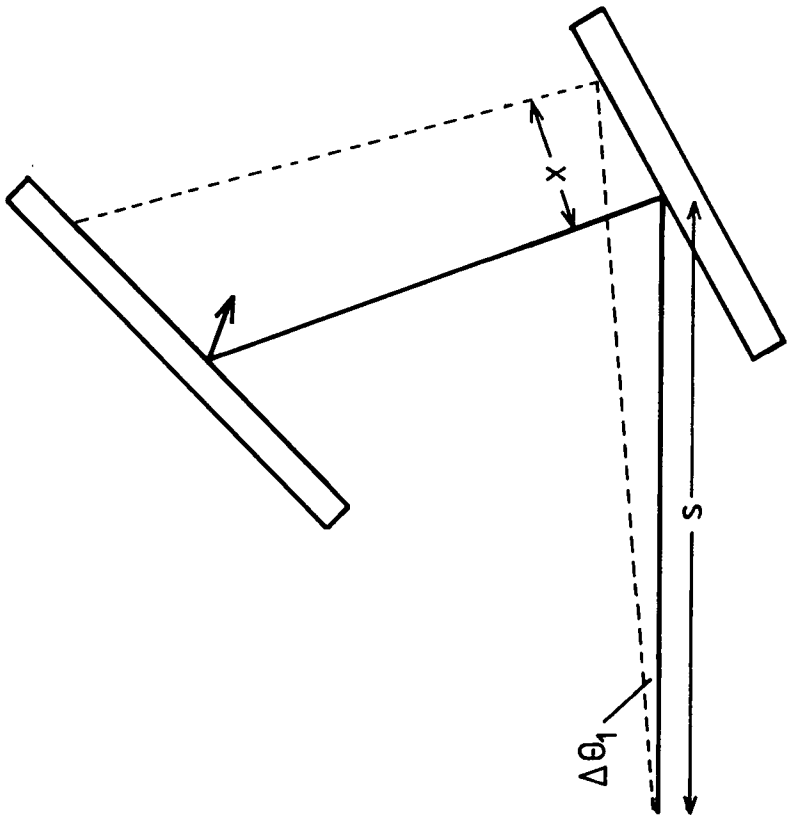

Fig. 2.10: Line diagram showing the variation in Bragg angle as a function of position in the plane of diffraction on the sample surfaces for the SRS

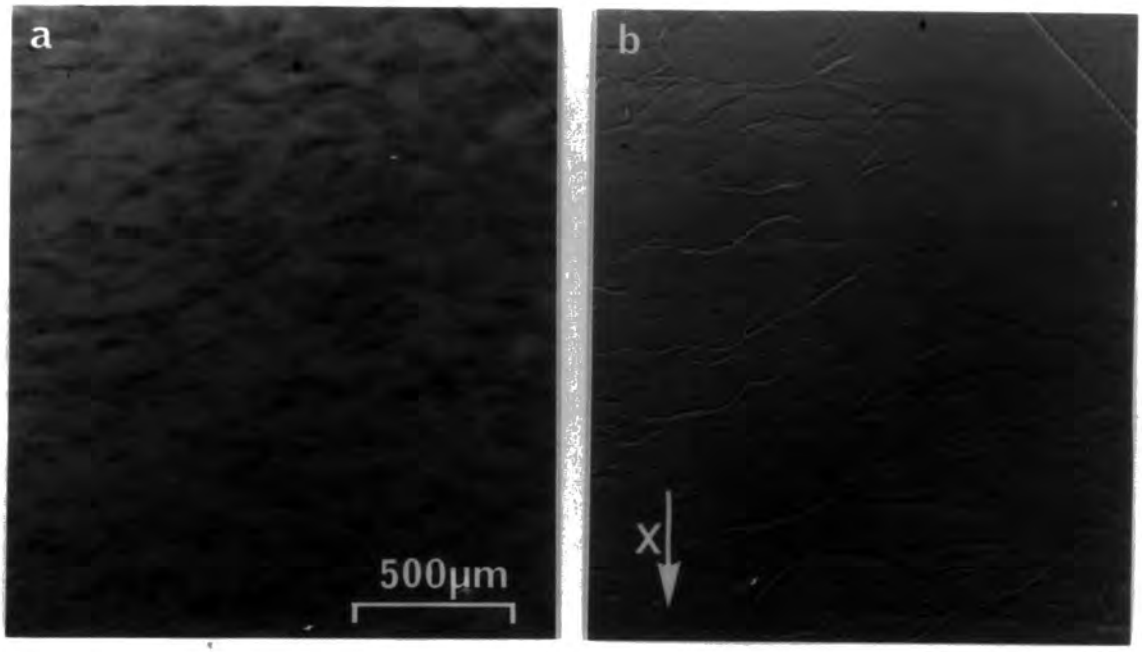

Fig. 2.11a: Double crystal topograph of a <111> cut slice of GaAs from the seed end of a boule, 422 reflection 1.54Å taken on the synchrotron source using a double reflection Si <111> beam conditioner

Fig. 2.11b: Topograph of the same sample using the same 422 reflection taken on a CuKα_1 tube source using the 422 reflection <111> cut Si reference crystal

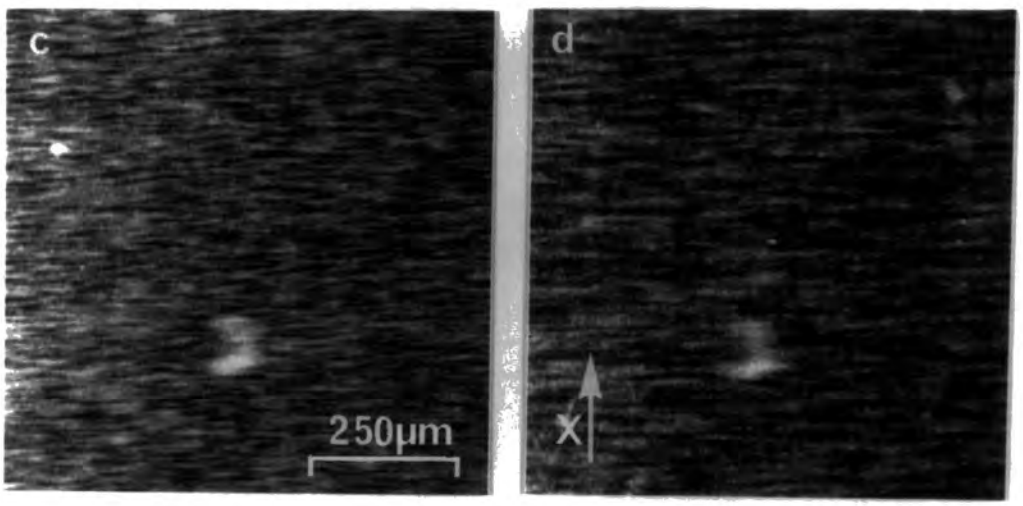

Fig. 2.11c,d: Synchrotron radiation topographs of the output from the Si <111> double reflection beam conditioner: c) sample to plate distance ~5cm, d) sample to plate distance ~15cm

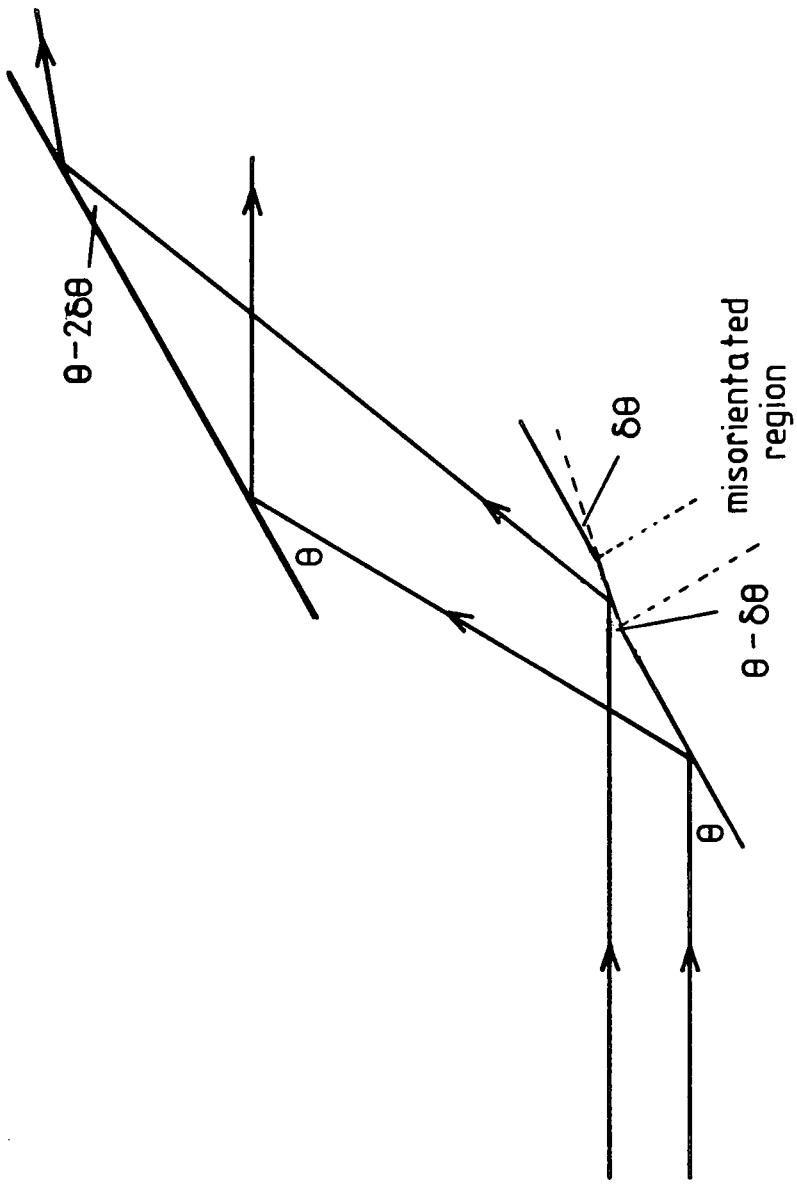

Fig. 2.12: Diagram showing the concept of misplacement contrast on double crystal synchrotron topographs

3. GaAs - LATTICE DISTORTION STUDIES

3.1 Experimental equipment and procedures.

3.2 Initial topographic studies.

3.3 Lattice strain and tilt measurements.

a) Feasibility study.

b) Main study.

   i. Experimental procedure

   ii. Results

c) Discussion

3. GaAs - LATTICE DISTORTION STUDIES

Chapter 3 begins with a description of the equipment and experimental procedures common to all the topography undertaken during this study. The initial investigations are then described followed by a presentation of the data relating to the long range lattice distortions in semi-insulating GaAs.

3.1 Experimental equipment and procedures

The double crystal diffractometer at the SERC's Daresbury laboratory is located in a safety interlocked hutch 65m from the radiation source (ref. 83). The x-ray beam travels from the source down a stainless steel beam pipe approximately 15cm in diameter containing a rough vacuum in order to reduce air scatter and absorption. Once inside the hutch the beam-pipe is terminated by a beryllium window measuring approximately 12.5cm horizontally and 2cm vertically. From this point the beam emerges into the atmospheric environment of the hutch and is aligned with the first axis of the double crystal diffractometer.

The double crystal diffractometer (ref. 84, fig. 3.1) consists of a cast aluminium casing into which are incorporated two precision bearings 300mm apart which form the two axes of the diffractometer. Each axis is driven by the linear motion of a micrometer pushing a spring loaded lever attached to the axis. The micrometers are driven by stepper motors through an anti-backlash gearbox. Although the maximum angular scan of this system is only 7.5 degrees the angular resolution is 0.2 arc seconds and the backlash is less than one arc second provided the system is well aligned and lubricated. The whole diffractometer is mounted on a bearing coaxial with the first axis which is stepper motor driven and allows automatic setting of the two theta angle so that the once diffracted beam passes through the second axis. This system is

mounted on a cradle which in turn is kinematically mounted on tungsten carbide balls and may be manually rotated about an axis parallel to the incident beam in order to make full use of the polarisation properties of the synchrotron source. The whole system is mounted on a thick steel base plate 2m by 1m and 0.5m above the ground. Coaxial with the second axis is a further axis which is used to manipulate any of the following detector systems; photographic plates, scintillation counters, ion chamber, energy sensitive Si detector, or TV imaging system. The whole system is massively constructed to allow mounting of large heavy sample stages and to give good stability when subject to the attention of experimenters (particularly after returning from the 'Ring o Bells'). Experience showed that when left for several hours on a Bragg reflection it was stable to within a few seconds of arc.

All the stepper motor driven axes are controlled by a PDP11/04 computer through a CAMAC interface system. The CAMAC system consists of a rack containing a series of addressable slots into which are placed cards capable of input and/or output of the signals necessary to control the stepper motors and other diffractometer requirements. The outputs from scintillation counters and ion chambers can be read by pulse counters and analogue to digital converters respectively mounted in the CAMAC rack. The control program was written in the CATEX control language specifically designed to control the CAMAC interface system. The program was menu driven and incorporated several options which ranged from simple routines to move an axis through a specified angle to routines that collect and display rocking curve data with a specified precision. For many of the experiments undertaken during this project these routines were adequate but for certain applications extra software was written which is described along with each application.

When setting up the diffractometer for a specific experiment the usual procedure was as follows. With the diffractometer set to diffract in the vertical plane a

precision spirit level was used to set the line joining the two axes in the horizontal plane. This defined the zero two theta position of the diffractometer which was then rotated by an angle two theta for the wavelength and reflection required. The monochromator system (either single or double reflection) was then mounted on the first axis at the approximate Bragg angle as measured using a variable set square. A sharp stainless steel reference point was then mounted in the second axis for use in the alignment procedure. A Polaroid film was placed behind (when viewed from the source) the reference point and with slits a few millimetres square in the centre of the incident beam a topograph was taken. The scattered white radiation from the first crystal produced a shadow image of the reference point on the film along with the image of the once diffracted monochramatic beam. The relative positions of the two images were then measured and the first axis rotated through the correct angle under computer control to achieve exact alignment of the once diffracted beam with the second axis.

The sample crystal was mounted with low temperature wax onto a perspex backing plate attached to an aluminium rod which was inserted into the second axis and set at the approximate Bragg angle. In order to find the sample reflection a low resolution TV imaging system was used. The system consisted of a fluorescent screen placed in front of an image intensifier which was viewed by a standard surveillance type TV camera. The system had a field of view of 2.5cm, a resolution of approximately 2-300μm and was sensitive enough to image sample reflections even when the sychrotron was operating at low energies and currents (e.g. 1.8GeV, <100mA). The TV system was placed in a position to view the sample diffracted beam, the sample axis was then rotated systematically to scan lower and higher incident angles until a diffracted beam image was seen on the imaging system. Once the diffractometer was aligned the process of finding the sample reflection, for the first sample, typically took 30 minutes, principally because of the slow scanning speed of the second high

precision axis and uncertainties of the exact sample orientation. For subsequent samples this time was reduced to typically 5–10 minutes since the sample holder was fixed in its orientation with respect to the second axis and the only uncertainty was in the exact sample orientation. All GaAs samples were bromine methanol polished before topography to remove any damage associated with the wafer lapping process.

To record topographs at high resolution ($<1\mu m$) Ilford L4 $25\mu m$ thick nuclear emulsion plates were used. They were processed at domestic refrigerator temperatures in the following sequence:–

a) soak in water for 10 minutes

b) developer 10 minutes (Kodak D19 stock solution diluted 1:3 parts water)

c) fixer 30 minutes room temperature (Kodafix, max concentration 1:6 parts water)

d) wash in water for 3 hours.

The processed plates were then dried at room temperature and the images enlarged by normal photomicroscopy methods in order to produce, as is usual in x–ray topography, positive prints of the original plate.

Low resolution topographs were recorded on either polaroid film or Agfa Structurix D7 film which was processed using Kodak D19 developer (1:3), Kodafix fixer (1:3) and a 10 minute wash. On all reflection topographs in this thesis the direction of the incident beam in the plane of the photographic plate is shown by the arrow marked 'X'. For transmission topographs the component of the diffraction vector in the plane of the photographic plate is indicated by an arrow labelled 'g'. All reflection topographs of (001) LEC GaAs are of the seed face and the <110> direction marked on the topographs lies parallel to the major flat for which the EJ flat convention is used.

3.2 Double crystal x-ray topography of GaAs - initial studies

The initial studies had two distinct aims-

a) to determine the feasibility of double crystal topography of large samples using the synchrotron radiation source, and

b) to set a base level for future investigations of semi-insulating LEC GaAs.

The first experiments aimed to record good quality high resolution topographs of 50mm diameter samples of GaAs. To monochromate the incident beam a <110> orientated float zone Si crystal was used which had been neutron transmutation doped (phosphorus doped). Float zone material is homogeneous and free from the oxygen and carbon striations which are present in Czochralski grown material and which manifest themselves as lattice parameter fluctuations. The presence of a phosphorus dopant was inconsequential since the neutron transformation doping would ensure a homogeneous distribution of the dopant. The surface symmetric 440 reflection from the monochromator was used to select a wavelength of 1.5A. From the <100> orientated sample crystal the 422 reflection was used for which the diffracted beam emerges from the surface at an angle of 75.8° and produces only a small image distortion. The first topographs suffered from very poor signal to noise ratio due to the large beam cross-section and a lack of effective shielding. The images obtained showed a non-uniformity in Bragg angle but detailed structure was unclear and emphasised the need to reduce the high background of scattered radiation.

The background radiation imaged on the plate was judged to be primarily a result of white radiation scattered from the monochromator crystal and secondly from air and equipment scattered radiation. In order to achieve effective

shielding three sets of slits were constructed. The first set attached to the end of the beam-pipe limited the size of the incident beam to one slightly larger than that required on the first crystal, this reduced the general background level due to air scatter and scatter from equipment. The second set placed before the monochromator crystal merely reduced the beam to the required size.

Between the first and second set of slits the beam passed along a lead pipe to prevent air scatter from reaching the photographic plate. The third set of slits were mounted on the diffractometer casing between the monochromator and sample crystal. This last set prevented a direct line of sight path between the monochromator crystal and the photographic plate. The slits were manually operated and adjustable from 0-125mm horizontally and 0-20mm vertically (the third set 0-100mm vertically). The slit material was 2mm thick lead sheet mounted on 2mm thick stainless steel backing plates which ran in tufnol runners. With this slit system in place the signal to noise ratio on the plate was such that the background level was unobservable.

The initial topographs showed the presence of Bragg angle variations across the sample, the next stage was to investigate these variations in more detail for different samples. The set of samples studied were supplied by Cambridge Instruments Ltd and grown in a high pressure puller using a boric oxide encapsulant and PBN crucibles. Five 50mm diameter samples were studied; an unannealed sample, one from the same boule annealed for 15 hours at 950°C and three samples grown from melts of different stoichiometry. The samples were mounted, using low temperature wax, at three points on their circumference onto a perspex backing plate which was attached to a rod inserted into the second axis of the diffractometer. All samples were at least 3mm thick to avoid any distortions due to the mounting procedure. For each sample a series of topographs was taken as a function of increasing incidence angle. The topographs were recorded on Polaroid type 52 film and exposures were 5

minutes with the synchrotron operating at 1.8 GeV and 50 mA.

The series of topographs for each sample is shown in fig. 3.2. It is clear that all samples show Bragg angle non-uniformities which range from 40-120 arc seconds. There is no evidence of distortions of the diffracting region near the mounting points and no three fold symmetry was seen as a result of the three point mounting; it was therefore assumed that the samples were unstrained by the mounting procedure. The topographs fig. 3.2a of samples 747, 767 and 759 grown from As rich stoichiometric and Ga rich melts respectively all show a two fold symmetry about the <110> directions lying in the crystal surface. This is more clearly seen in fig. 3.3 which shows the sequence of topographs of sample 767 traced onto the same image to give a Bragg angle map. It is not obvious however, whether lattice strain or tilt or a combination of the two is responsible for the Bragg angle variations. If lattice tilt plays the dominant role, it may be due to an elastic distortion caused by sample warpage or the atomic planes may be tilted elastically and/or plastically as a result of the defect structure in the material. Studies of wafer warpage on samples grown by the same method (refs. 85,86) have shown saddle shaped bow with a two fold symmetry about the <110> directions, this, however, was only observed in wafers less than 1mm thick and was thought to be a consequence of the polishing process. Fig 3.4 shows a warpage map of sample 767 determined by the laser scanning method using a Canon LSF500. The sample exhibits saddle type bow with a maximum peak to valley distance of 7.5 μm, the symmetry however, is rotated by approximately 45° to that reported by Obokata et al (ref. 85). The Bragg angle map fig. 3.3 is unlikely to represent just sample warpage since its symmetry is different to the warpage map. The lattice planes in the sample cannot lie parallel to the sample surface unless there is a two-fold lattice strain distribution which adds to the lattice tilt caused by the sample warpage to produce the observed two fold Bragg angle map, a highly unlikely situation.

The Bragg angle maps do, however, bear a striking resemblence to the

distribution of the deep level EL2 as mapped by Holmes et al (ref. 29). It is thus speculated that there is a significant component of lattice strain in these maps which might reflect stoichiometry variations.

The Polaroid topographs of the annealed and unannealed samples, fig. 3.2b, exhibit a less clear two fold symmentry but are generally more uniform with a larger area of sample diffracting at any one time than those in fig. 3.2a. Comparison of the two samples, annealed and unannealed, reveals that the annealed sample is more uniform but still exhibits sharp Bragg angle changes across both <110> and <100> directions in the sample surface.

High resolution topographs recorded on L4 nuclear emulsion plates using the same reflection geometry reveal the presence of individual dislocations arranged in various configurations as previously observed in the etching studies of Holmes and Chen (ref. 16). Dislocations are observed in cellular or polygonised structures, linear arrays (lineage) which tend to be aligned along <110> directions and slip bands. An example of each of these features is shown in fig. 3.5. Cells are typically 150–250μm across and it can be seen in fig. 3.6 which shows topographs of cell structure taken at different positions on the rocking curve, that there are small discrete changes of Bragg angle associated with the cell walls. These changes are only observed on the flanks of the rocking curve where the strain sensitivity is the highest which suggests that Bragg angle variations of less that 2 arc seconds are involved. Lineage features on the other hand, exhibit much larger Bragg angle changes, for example in fig. 3.5b the area above the lineage feature is on the peak of the rocking curve and that below shows almost zero diffracted intensity. This situation corresponds to Bragg angle variations in excess of 10 arc seconds. A topograph taken of the same lineage feature using another 422 reflection with the sample rotated by 90° about its surface normal shows no sharp change of contrast and only the dislocation images can be observed. This means that the Bragg angle change

observed at lineage features has no measureable component parallel to the lineage feature. It is unlikely that a lattice strain is responsible since it would cause a contrast for both orthogonal orientations of the diffraction vector. A lattice tilt with a tilt axis parallel to the direction of the lineage feature on the sample surface is a more likely explanation.

Fig 3.7a shows a double crystal topograph of a <100> slice of GaAs taken on a tube source using Cu radiation with the 422 reflection and the 440 reflection from a <110>orientated Si reference crystal. The $K\alpha_1$ and $K\alpha_2$ components are both visible but are spatially separated due to the slight dispersive nature of the diffraction geometry used. The central region of the topograph, arrowed, contains a typical lineage feature extending along one of the <110> directions. In order to measure the magnitude of the Bragg angle change across this feature a rocking curve was recorded using a beam collimated to 85μm wide and approximately 10mm long which was allowed to span the lineage feature with its larger dimension. The measurement was made using the SRS to avoid any confusion associated with the $K\alpha_1$ and $K\alpha_2$ lines. The surface symmetric 400 reflection was used at a wavelength of 1.5Å and the incident beam was conditioned by a double reflection Si monochromator. The rocking curve fig. 3.7b consists of two distinct peaks, one from each side of the lineage feature, separated by an angle of 36 arc seconds (0.01°). The difference in intensity of the two peaks is probably due to an asymmetry of the central point of the slits relative to the lineage feature. The widths of the larger and smaller peaks are 35 arc seconds and 25 arc seconds respectively (cf. theoretical 400 peak width 10 arc seconds). This bears out the previous assumption of slit position since the larger broader peak, corresponding to the side of the lineage feature with the larger slit area, will cover more cell structure and specifically cross more cell walls, across which small Bragg angle changes have already been observed. The measured peak separation of 36 arc seconds represents the average Bragg angle difference for the areas covered by the slit either side of the lineage

feature. The usual contrast associated with the lineage features fig. 3.2 suggests a gradual change of Bragg angle of the same sign as a function of distance on either side of the lineage line with an abrupt change at the lineage feature itself. The rocking curve, since it represents an average tilt is an upper limit of the tilt associated with the lineage feature itself. An infrared transmission micrograph, at a wavelength of 1 μm, of the above sample reveals an increased concentration of the deep level EL2 associated with the cell structure and the 4 lineage features lying along the <110> directions as has previously been observed (refs. 27, 28). There is however, no contrast associated with the slip bands observed in the x-ray topograph which would suggest the lack of an enhanced level of EL2 at these features. If the sample is sectioned along a {110} plane normal to the wafer surface and an infrared micrograph taken then the slip bands are clearly visible, fig. 3.8 and correspond to enhanced 1 μm IR absorption. The reason no contrast was observed on the <100> orientated sample was that the slip bands lie in the {111} slip planes which are inclined to the sample surface and the contrast is smeared out when viewed from the <100> direction. It is shown that all areas of high dislocation density as observed by x-ray topography, i.e. cell walls, lineage and slip bands exhibit an increased concentration of EL2. This finding casts doubt on the theory put forward by Weber et al (ref. 87) and Stirland et al (ref. 88) that dislocations getter EL2 as they climb into the cell and lineage configurations. If this were the case then enhanced absorption at slip bands would be much smaller since (a) the dislocations have not undergone extensive climb and (b) they have all moved along the same path in the slip plane and have been unable to getter EL2 from a large volume of crystal as the motion of the first dislocation would deplete the surrounding crystal of EL2 and the following dislocations would play only a minor role in the gettering process. A more likely explanation for the enhanced EL2 concentration is an electrostatic or strain interaction between the dislocations and the EL2 centre as suggested by the AB etching and cathodoluminescence work of Warwick and Brown (ref. 30).

The topographic studies so far undertaken strongly suggest the presence of lattice tilts which are associated with the dislocations arranged in cell walls and lineage features. There is no evidence, however that the Bragg angle variations observed are solely due to lattice tilt variations. The similarity of the Bragg angle maps to EL2 maps (ref. 29) suggests a lattice strain component possibly related to the EL2 concentration. The need to resolve clearly the lattice tilt and strain components is thus apparent. It is already clear that lattice tilts are the primary component of the Bragg angle variations which puts an upper limit on the strain variations of approximately 50ppm. The method chosen to measure these variations is described in section 2.5 and is based on that first used by Kikuta (ref. 82) to study distorted Si wafers.

3.3 Lattice strain and tilt measurements

(a) Feasibility Study

The first 50mm wafer studied using this technique was supplied by Wacker and was grown using a low pressure puller. The crystal was pulled from a quartz crucible with a wet boric oxide encapsulant to remove the dissolved Si from the melt. In order to achieve the required strain sensitivity the 800 reflection at 1.2Å was used. The previously mentioned <110> orientated float zone Si crystal was used to monochromate the incident beam using an asymmetric 800 reflection. This asymmetric reflection expanded the beam to cover the 50mm sample crystal and also reduced the divergence of the beam incident on the sample. The diffraction geometry is shown in fig. 3.9. The success of this technique depends partly on the uniformity and flatness of the Si monochromator so this was rigorously tested by taking a topogaph using a similar <511> orientated Si monochromator. The resulting topograph was completely uniform and the rocking curve half width was that expected for the

diffraction geometry used. Because of the sharp rocking curves obtained from Si the strain sensitivity is estimated as parts in 10^7, an order of magnitude better than those required for the GaAs sample crystals. The sample mounting procedure had already been tested for the previous less strain sensitive settings but for these settings it was necessary to do further more rigorous tests. The sample was mounted at three points in the normal way with low temperature melting point wax to secure it to the perspex backing plate. A series of low resolution topographs using the 800 reflection were taken as a function of increasing incidence angle. The sample was then remounted with the wax at different positions on the sample circumference and the experiment repeated. Both sets of topographs showed identical Bragg angle distributions thus proving the sample mounting procedure and the reproducibility of the diffractometer axis drive mechanism. For the Bragg angle maps to be used in the strain/tilt measurements, a step size of 2 arc seconds was chosen and topographs were recorded on Agfa Structurix D7 film with and exposure time of 40 secs. while the synchrotron was running at 2.0GeV and 150mA. Two series of topographs were taken as described in section 2.5 and care was taken to ensure exact alignment of the sample after the 180° rotation about the diffraction vector.

Analysis of the topographs to resolve lattice strain and tilt components of the Bragg angle variations began with the superposition of each series of topographs onto a single image. A photographic enlarger was used to magnify each topograph by a factor of four. The leading edge of the diffracting region on each topograph was then traced onto a single image. The exact position of the leading edge was well defined because of the large intensity gradient on the side of the sharp 800 rocking curve. The two composite Bragg angle maps, one from each sample orientation, were then photographed and reproduced on one print. The areas defined by each map were numbered to represent the lattice tilts and strain, using the theory described in section 2.5. Fig 3.10 shows a colour coded representation of the lattice tilt map where all values are relative

to the position marked r_o. The strong lattice tilt change associated with the two diametric <110> orientated lineage features is clearly seen. There is no evidence of any orthogonal lineage features even though they are clearly visible on the 1μm infrared absorption micrograph (fig. 3.11). Since x-ray diffraction is only sensitive to tilt in the plane of diffraction this experiment reveals that any tilt associated with the lineage features has no component parallel to the lineage feature in the (100) plane of the sample surface. The corresponding lattice strain map is shown in fig. 3.12. This map is slightly misleading and bears a striking resemblence to the tilt map, this is because both tilt and strain maps are produced from the same composite Bragg angle map and as the lattice tilt component dominates the Bragg angle variations, the area boundaries are primarily defined by the lattice tilt variations. If one concentrates on the shading rather that the area outlines the proper strain variations can be observed. Fig 3.13 shows an averaged representation of the strain data, each figure represents the average strain in that area relative to position r_o. The total lattice strain is approximately 20ppm and in general there is a smaller lattice parameter at the sample edges relative to the centre but superimposed on this is a decrease in lattice parameter from left to right.

Measurements by several authors (refs. 32-34, 39, 40) in lattice parameter suggest an increase with respect to As melt concentration. For this sample the periphery would be less As rich than the centre. In view of the well documentated "W" shaped EL2 profiles (refs. 2, 29) and the commonly held belief that the EL2 defect is related to an increased As concentration it is unlikely that the lattice strains observed represent stoichiometry fluctuations. Fig. 3.12 shows that the sample centre is uniform to within 8ppm but that larger strains of 20ppm are present at the periphery. It is more likely that these lattice strain variations are related to the dislocation density which increases from 8 x $10^3 cm^{-2}$ in the central region to 6 x $10^4 cm^{-2}$ at the periphery, as measured by counting KOH etch pits.

This experiment demonstrates the usefulness of double crystal topography for the mapping of lattice strain and tilt variations over large area samples. The data obtained substantiates the previous results which suggested strong tilts associated with the lineage features which are superimposed onto more gradual tilt variations across the sample. The Bragg angle variations of 26 arc seconds across the sample were found to be mainly composed of lattice tilt variations amounting to 20 arc seconds the remainder being strain variations of approximately 24ppm. Having shown the presence of the above lattice distortions in semi-insulating material grown from a low pressure puller a more systematic study of the more technologically relevant high pressure pulled material was thought desirable. In order to reduce both the experimental time and the data analysis time a number of improvements were made to the system to allow automated data acquisition and computerised data analysis. The improvements, experimental procedure and results are presented below.

b. Main Study

(i) Experimental Procedure

The experimental procedure adopted for the initial strain and tilt measurements was adequate for a single sample but for many samples would be time consuming and prone to error. The two major drawbacks involved the manual data acquisition process and the inflexibility of the data analysis. During the initial studies the Bragg angle maps were obtained from a series of individual topographs taken by a repeated manual process of changing the photographic film, stepping the sample axis to the next position, searching and interlocking the experimental hutch and finally exposing the topograph. This process was time consuming (~ 3-5 mins per topograph) and great care had to be taken to avoid disturbing the sample crystal. The data acquisition process was improved

by the use of a stepper motor driven automatic multiple film cassette holder which carried ten films and greatly reduced data acquisition times. Software was written which automatically advanced the multiple plate holder and sample axis after a specified exposure time. The shutter was not closed between each topograph since the process of changing film and moving the sample axis took only 1–2 seconds compared with exposure times of 45 seconds. In this way ten topographs could be recorded in only 5–6 minutes without entering the hutch. The data analysis process was improved by digitising the Bragg angle maps and analysing the digitised data using a BBC micro-computer. The Bragg angle maps for each sample were produced in the manner previously described and digitised into pixels corresponding to a 1mm x 1mm square on the sample surface. The digitisation process involved overlaying a rectangular grid onto the Bragg angle map and manually inputting the data for each pixel into the BBC keyboard. BBC software was written such that only three input keys were required; two keys to increment the pixel value, one up one down and a third key to register the value for a pixel and move onto the next pixel. In this way a complete Bragg angle map for a 50mm diamter wafer could be digitised and checked in 45 minutes. Once stored on floppy disk the data could be accessed by software which allowed rotation of maps by 90° about the sample centre, calculation of tilt, displacement and strain and output of the data in the form of grey level images or plots across a chord of the circular sample crystals. Various methods of data presentation were tried the most successful of which are used below.

In all six samples were studied; an In doped sample grown from a melt containing 1 at. % In, samples taken from the seed and tail ends of a boule and samples annealed at 950°C for 5 hours. All samples were at least 3mm thick in order to avoid mounting strains and to ensure the sample represented a true picture of the lattice distortions present in the ingot, rather than sample warpage strains often introduced by the wafer polishing process for commercial

450 μm thick wafers (refs 85,86). The angular increment between topographs in the Bragg angle maps varied between 2 and 6 arc seconds depending on the magnitude of the lattice distortions in the sample. This increment resulted in a final error in the lattice strain data which varied between ± 2–4ppm. In order to permit calculation of the two orthogonal components of lattice tilt of the (001) planes four series of topographs were recorded for each sample with the sample rotated by 90° about the diffraction vector 'g' between successive series. For each sample orientation approximately twenty topographs were recorded. A picture of the diffractometer set up for those experiments is shown in fig. 3.14. The same reflection conditions were used as in the previous study (i.e. surface symmetric 800 sample reflection, 800 reflection from <110> orientated Si reference crystal and λ = 1.2Å) and exposure times were typically 30 seconds with the synchrotron running at 2GeV and 200mA. In order to permit a comparison of the long range lattice distortions with the defect structure each sample (after the topographic studies) was etched in molton KOH at 370–390°C for 15 minutes.

The data for each of the samples studied are presented below.

(ii) Results

In doped GaAs

Fig 3.15 shows a composite topograph of the sample with an angular increment of 10 arc seconds between successive topographs. The contrast associated with In concentration striations is clearly visible, particularly at the centre of the sample. The map does not show any four-fold or eight-fold symmetry usually observed in undoped material, instead there is a gradual change of Bragg angle, across the diameter of the crystal, which is perturbed by features such as those marked by the arrows. Fig 3.16 shows a picture of the KOH etched surface of

this sample, the discrete changes in direction of the contrast bands indicated by A in fig. 3.15 can be seen to correspond to isolated slip bands.

A lattice strain map of the same sample is shown in fig. 3.17, this map was produced on a dot matrix printer driven by the BBC microcomputer. The BASIC software used to drive the printer generated a bit image for each element in the 50 x 50 element strain map (approximately 125,000 bits for a 50mm diameter sample). For each dot on an 8 x 8 dot pixel (corresponding to a single element on the strain map) a random number was generated on a scale equal to the total range of strain values in the map. A dot was then printed if the strain value for that element exceeded the random number for the dot. In this way the image was built up in rows of 8 x 8 dot pixels and printed as user defined characters. To calculate and plot an image for a 50mm diameter wafer map digitised in 1mm square pixels took approximately 45 minutes. An alternative representation of the above strain map is shown in fig. 3.18, here the image is generated by a plotter using pre-programmed grey levels for each map element. Constraints imposed by the plotter pen widths limit the number of levels in the grey scale to six but as a result contrast changes are more apparent (compare the features marked A on each map).

The lattice strain maps of the In doped sample fig. 3.17 and fig. 3.18 exhibit an axially symmetric 'W' shaped profile on which are superimposed discrete areas of reduced lattice parameter associated with the isolated slip bands such as those marked (A). Under higher magnification the feature marked (A) on the KOH etch picture, fig. 3.16, can be seen to consist of three closely spaced slip bands each with a dislocation spacing of approximately 25μm. These three slip bands correspond to an area of reduced lattice parameter of approximately 7ppm. The periphery of the sample, where there is a high density of slip dislocations, has approximately the same lattice strain as the central region, except in isolated areas very close to the sample edge.

The vector nature of the lattice tilt excludes grey level images as a method of output representation. Fig 3.19 shows a grey level map of the lattice displacement for the In doped sample; here the lattice tilt data is integrated between the limits of the central zero reference position and the position r to give the displacement of the (001) lattice planes in the [001] direction. This displacement map reveals an axially symmetric displacement field with the lattice planes at the centre of the sample being displaced in the direction of crystal growth with respect to those at the periphery. (On all the lattice displacement maps the data presented are relative to the centre of the sample and the outward pointing surface normal is the positive direction). Fig. 3.20 shows a representation of the lattice tilt for the central part of the In doped sample, the length of the arrows represents the magnitude of the tilt and the arrow direction that of maximum slope of the (001) planes out of the plane defined by the (001) planes at the centre of the sample. The slip bands marked (A) on the KOH etch map fig. 3.16 and the lattice strain maps figs. 3.17 and 3.18 are seen to correspond to a discrete change in lattice tilt as are the other isolated slip bands the position of which are shown by the solid lines. These isolated perturbations to the lattice tilt are not visible on the lattice displacement map since they correspond to less than one increment in the grey scale of the displacement map. Fig 3.21 shows a picture of the KOH etched In doped sample alongside a line scan of the lattice strain and lattice tilt, the correlation of the data is clearly illustrated.

Undoped GaAs

KOH etched surfaces, 1μm IR absorbtion micrographs, lattice strain, tilt and displacement maps for samples taken from the seed, 'MMT 76 T2', and tail 'MMT 76 B2', ends of an undoped boule are shown in figs. 3.22 and 3.23. The seed end sample shows uniform lattice strain to within 10ppm in its central

region and only in isolated areas at the sample edge are there larger deviations corresponding to areas of positive strain, fig. 3.22c. The corresponding lattice tilt and displacement maps fig. 3.22d,e, exhibit a four fold symmetry about the two <110> and <100> directions in the sample surface. The lattice planes, towards the sample edge, lying along the <100> directions are displaced in the growth direction relative to those at the sample centre, while those along the <110> directions are displaced in the opposite sense. The KOH etch picture fig. 3.22a and the 1μm IR absorption micrograph fig. 3.22b reveal the presence of lineage features lying mainly along the <110> directions in the sample surface, i.e. both exhibit the same symmetry as the lattice tilt and displacement maps. The tail end sample MMT 76 T2 reveals a less uniform lattice strain distribution but over a similar range of values which may reflect the less uniform dislocation distribution fig. 3.23a. The lattice displacement map of this sample fig. 3.23e shows a two fold symmetry about the <100> directions which can be correlated with the presence of lineage features along these directions and their absence in the more usual <110> directions as revealed by the KOH etch fig. 3.23a and the 1μm IR micrograph fig. 3.23b.

Data from the annealed, 'MMT 65a an', and unannealed 'MMT 65a un' samples (both from the seed end of a boule) are presented in figs. 3.24 and 3.25 respectively. Both samples reveal a lattice strain distribution which is uniform to within 10ppm in the sample centres and increases by approximately 20ppm at the edges of the samples. The corresponding lattice displacement maps fig. 3.24c and fig. 3.25c both show the usual four fold symmetry with lattice displacements of the same sense as previously observed for seed end crystals. The KOH etch picture for the annealed sample fig. 3.24a shows the usual lineage feature distribution (mainly along the <110> directions) but that for the unannealed sample fig. 3.25a does not reveal the presence of any lineage features. It is, thus, interesting to note that the lattice displacement map for the annealed sample shows a much more pronounced symmetry than

that for the unannealed sample a feature connected with the large lattice tilts already shown to be associated with lineage features. The lack of lineage features in the unannealed sample compared with the annealed sample is unlikely to be associated with the annealing process, the unannealed sample came from the very top of the boule where the grow-out was not quite complete and would therefore have been subject, during growth, to a different thermal stress pattern to the lower annealed sample.

Another annealed sample 'MMT 65 Z an' from the tail end of the same boule as the above two samples showed the typical lattice strain distribution and a four fold symmetry on its lattice displacement map fig. 3.26b. The four fold symmetric lattice displacement map does however differ from those previously observed, here the sample centre is the highest point with the lattice planes along the <110> directions being lower and those along the <100> directions lower still. The KOH etched picture, fig. 3.26a revealed a very high dislocation density, the absence of lineage features along the <110> directions and their presence along the <100> directions.

c) Discussion

Of all the samples studied, the In doped material exhibited the largest variations in both lattice strain (91ppm) and lattice displacement (12μm). Sharp changes in lattice strain (-7ppm) and lattice tilt were observed at slip bands sitting in areas of low background dislocation density. Although there is no clear macroscopic correlation between dislocation density and lattice strain it is interesting to note that the areas of largest lattice strain round the sample edge correspond to the highest dislocation densities. This is particularly so in the <100> directions where there is a high density of slip dislocations (greater than $5x10^4cm^{-2}$ in some areas) and the highest strain values occur. A possible explanation for the observed strain distribution is that it corresponds to

variations in In concentration. The magnitude of the observed 'W' shaped strain profile is approximately 45 ppm with only isolated areas primarily along the <100> directions near to the sample edge having a larger lattice strain. Since In dilates the GaAs lattice the In concentration profile would also be 'W' shaped with an absolute In concentration variation of 0.031 at. % In (assuming InGaAs obeys Vegards Law). This amounts to a relative fluctuation of 20% assuming the average In concentration in the crystal to be 0.15 at. % (and the segregation coefficient of In in GaAs to be 0.15). Other measurements of In concentration fluctuations in 75mm In doped LEC GaAs have been undertaken by Yu et al (ref. 58), who measured the photoluminesence shift in the C_{As} bound acceptor exciton $A^{\circ}X$ transition at 2K. For several samples they found a vague 'W' shaped In distribution with the sample edges always having a In concentration larger by approximately 0.015 at. % (the samples were grown from a melt containing 1 at. % In) and similar values were obtained regardless of sample position in the ingot. Other PL measurements by Kitahara et al (ref. 57) have indicated In density variations of 10–20% on a wafer. The present data may reflect In concentration variations of the same magnitude to those previously reported but a direct detailed comparison is unjustified since concentration variations will depend upon the growth conditions employed.

Unfortunately corroborative evidence in support of the above supposed In concentration variations cannot be gained from the observed dislocation density distribution, which, assuming In hardens the GaAs lattice, might be expected to vary inversely as a function of the In concentration. If, however one considers only the randomly distributed dislocations <u>not</u> lying in slip bands then the diametric distribution is indeed 'M' shaped (see fig. 3.16). (The slip band dislocations are not considered since, for each set of slip band dislocations, there is probably a single source usually at the sample edge which produces dislocations which glide towards the sample centre and are unaffected by the variations in In concentration).

Unfortunately other work using Lang transmission topography suggests that these randomly distributed dislocations are not affected by the In concentration (ref. 56) and identifies three distinct types of dislocation in In doped (001) orientated LEC material:

a) Type A dislocations form from seed dislocations or due to a lattice mismatch between the seed and growing crystal (arising from a difference in In concentration) and tend to grow down the (001) growth direction.

b) Type B dislocations form at the crystal surface during the grow-out stage and again propagate down the (001) growth direction.

c) Type C dislocations are generated due to thermally induced stresses and lie in slip bands, they generally exhibit a 'W' shaped diametric distribution profile and a four fold symmetric distribution in the (001) wafer surface.

The density of types A and B dislocations are unaffected by the In concentration since they are formed and propagate at the growth interface. Measurements of the CRSS in material with typical In concentrations show a doubling compared to the undoped value, this is not sufficient to explain the reduction in dislocation density achieved in In doped material (ref. 56) and it is thought that In merely increases the critical stress for dislocation motion and therefore only affects the slip band dislocations (ref. 56). If this situation is the case the previous In concentration explanation of the lattice strain cannot be substantiated by the distribution of type A and B dislocations. The 'M' shaped dislocation profile would merely indicate a lack of type A dislocations presumably because of a well lattice matched and low dislocation density seed crystal and a somewhat higher density of type B dislocations due to the

grow-out conditions.

The slip band dislocation density increases at the sample edges and has a four fold symmetry and maximum dislocation density along the <100> directions in agreement with the thermal stress models of Jordan et al (ref. 21). The strain distribution observed in this In doped sample relative to that in the undoped samples might then be explained in terms of the magnitude of the dislocation density profiles in the two types of sample. In the undoped samples there is a lattice parameter increase of typically 20ppm at the sample periphery where the dislocation density is highest, and the dislocation density (averaged over a few square millimetres) varies from 2×10^4 cm^{-2} to 7×10^4 cm^{-2} over a typical sample crystal. For the In doped sample the spread of dislocation density is significantly larger, from $2 \times 10^3 cm^{-2}$ to $5 \times 10^4 cm^{-2}$ and so is the magnitude of the lattice strain variations. At the periphery of the In doped sample the dislocation density shows a direct correlation with the lattice strain with areas along the <100> directions from the sample centre having the largest dislocation density and the largest strain. The correlation between strain and dislocation density does not, however extend over the whole sample, the region within 15mm of the sample centre does not exhibit the classical 'W' shaped profile. This is probably due to the average In concentration in the crystal and the growth conditions used (ref. 56) which can result in a more 'U' shaped profile.

The lattice tilt data from the In doped sample reveals the tilt associated with isolated slip planes but the strain associated with these areas is opposite to that for the high dislocation density periphery of the sample. The overall lattice tilt produces a lattice displacement which is vaguely symmetric about the centre of the sample with the sample centre being displaced in the direction of crystal growth with respect to the periphery. Since the effect of isolated slip bands is clearly seen on the lattice tilt it is likely that the observed tilt distribution is

due to the dislocation structure and indeed along the <100> directions at the bottom of the sample where the dislocation density is highest the largest tilts and displacements are seen.

In summary; for the In doped sample neither In concentration variations nor a strain associated with the dislocations (either from the dislocation induced strain field or segregation of point defects around dislocations) can be explained by the observed dislocation distribution. In the light of photoluminescence measurements on other 75mm material (refs. 85, 86) it is likely that In concentration variations do exist in this sample and are reflected in the strain measurements. The strain data also show the effects of isolated slip bands. It is probable, therefore that both the above parameters (In concentration variations and dislocation density) are correlated with the lattice strain, but the lattice tilt is primarily determined by the dislocation structure.

All the undoped material studied was more uniform in both lattice strain and displacement than the In doped sample. Most samples exhibited maximum strain values of typically +20ppm around the periphery and all samples showed tilts to be associated with the lineage features. The two samples 'MMT 76' 'T2' and 'B2' from the seed and tail ends of an annealed ingot showed different lattice tilt and displacement patterns which reflects the difference in their lineage feature distributions. The lineage features in 'MMT76 T2' all propagated in the <110> directions in the central region of the sample and towards the edges along the <110> directions the cell walls running in a radial direction were elongated with respect to those in the tangential direction. In the tail end sample 'MMT 76 B2' there was a lack of lineage features running along the <110> directions, those present being along the <100> directions. Also in contrast with the seed end sample, in the tail end sample, in regions close to the sample edge along the <110> directions the cell walls are elongated in the tangential direction rather than the radial direction. This

difference in dislocation distribution is seen to have a direct effect on the lattice tilt. The lattice strain data from the seed end sample exhibits the usual distribution with the high dislocation density periphery having the highest strain values. This, however, is not the case for the tail end sample where the lattice strain distribution is far less homogeneous and may possibly reflect the larger spread in dislocation densities present in this sample.

The annealed and unannealed samples from the seed end of an ingot ('MMT 65 A an' and 'MMT 65 un') both exhibit the usual strain distribution and symmetry in their lattice displacement maps. This similiarity in lattice strain is noteworthy since EL2 is known to redistribute homogeneously on annealing. This result suggests that the lattice strain is unrelated to the EL2 concentration and may instead be correlated with the dislocation distribution. The common symmetry in the lattice displacement maps is interesting since the unannealed sample contains no lineage features. The symmetry of the unannealed sample displacement map is only apparent close to the sample edges and probably reflects the magnitude of the thermally induced stress pattern imposed on the crystal during growth. A more pronounced symmetry in the annealed sample displacement map reflects the presence of the lineage features possibly present because of the slightly larger diameter of this sample with respect to the unannealed sample which would result in larger thermal stresses during growth.

Sample 'MMT 65 Z an' (from the tail end of the same ingot as the above two samples) shows the usual strain distribution with a similar four fold symmetric lattice displacement map to those usually observed. This sample is heavily dislocated and the only lineage features present are aligned along the <110> directions. Although this is a tail end sample it does not show the same elongation of the tangential cell walls (near the periphery along the <110> directions) as sample 'MMT 76 B2' and therefore might not be expected to show the same lattice distortions.

The strains observed in the above undoped samples are of similar magnitude and distribution to those measured using double crystal x-ray topography by Kitano et al (ref 50), but they fail to state the sample diameter so a direct comparison is not possible. They arrive at the same conclusion regarding lattice tilt (i.e. that it is primarily determined by the dislocation structure) but they have not analysed both orthogonal components of tilt in the same manner as is done herein. The detailed lineage and cell structure have been examined topographically by Matsui et al (ref 49) and they found similar lineage feature formation and elongation of the radial cell walls along the <110> radial directions. They, however, have only looked at samples from the seed end of boules and consequently always observed the same symmetry which agrees with the symmetry model proposed by Kitano et al (ref 57). The tail end samples observed in this study ('MMT 76 B2', 'MMT 65 Zan') clearly indicate a lack of this predicted symmetry which may be due to a different thermal stress pattern induced in the tail of the ingot or perhaps related to the different point defect environment caused by the gradual change in stoichiometry down the boule which arises if the starting melt is not exactly stoichiometric (ref 40).

A collection of all the above data for undoped samples suggests a correlation between lattice strain and dislocation density, but a comparison of unannealed and annealed samples exludes EL2 (which usually correlates with dislocation density in unannealed material) as the primary cause of lattice strain. The lattice tilts in the material show a good correlation with the dislocation distribution, the primary cause of lattice tilts being lineage features. The presence of a four fold symmetric displacement field is observed even in the absence of lineage features which reflects the thermal stress pattern experienced by the growing crystal and the crystallographic symmetry of the material.

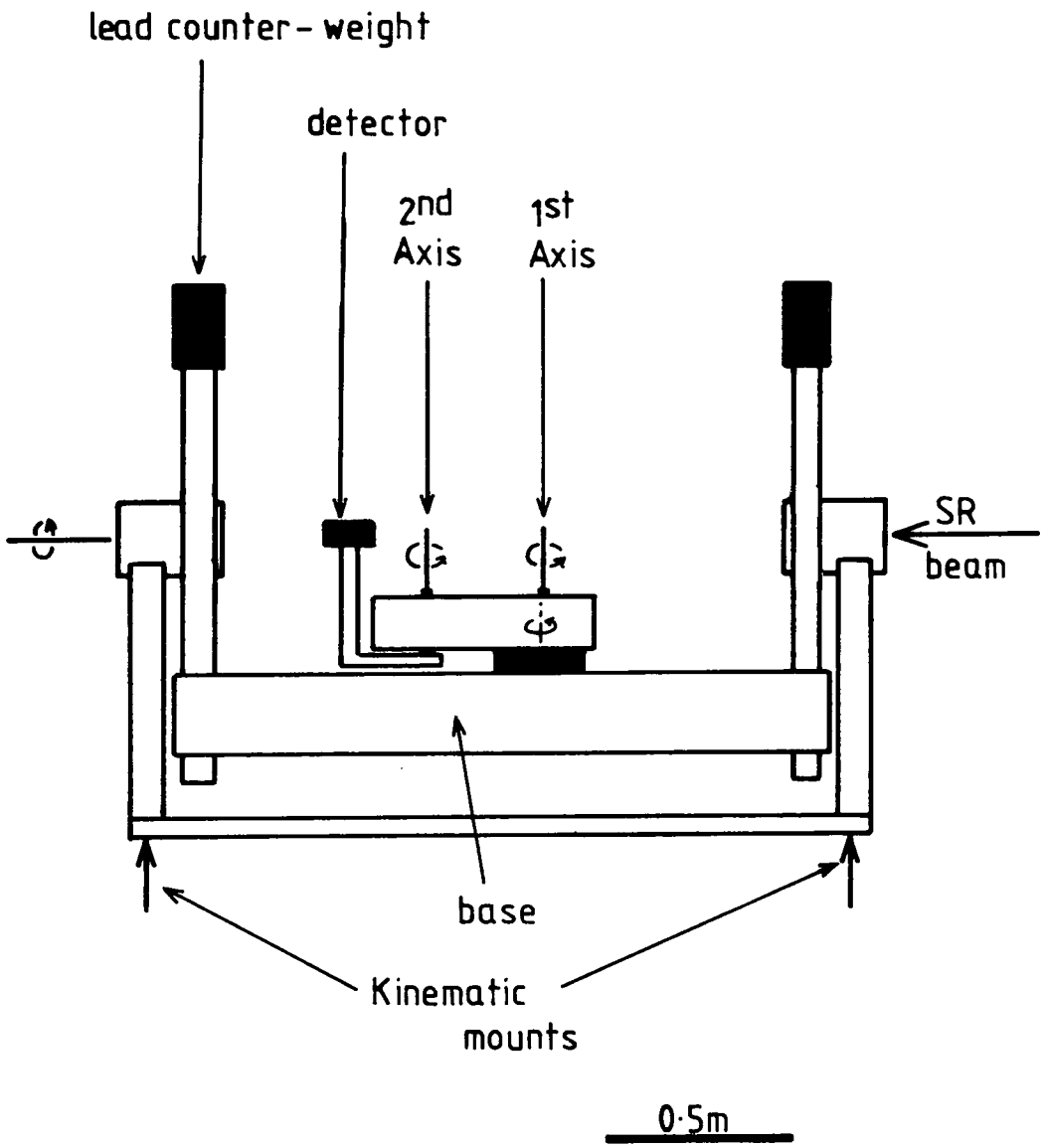

Fig. 3.1: Line diagram of the double crystal diffractometer on station 7.5 of the Daresbury SRS

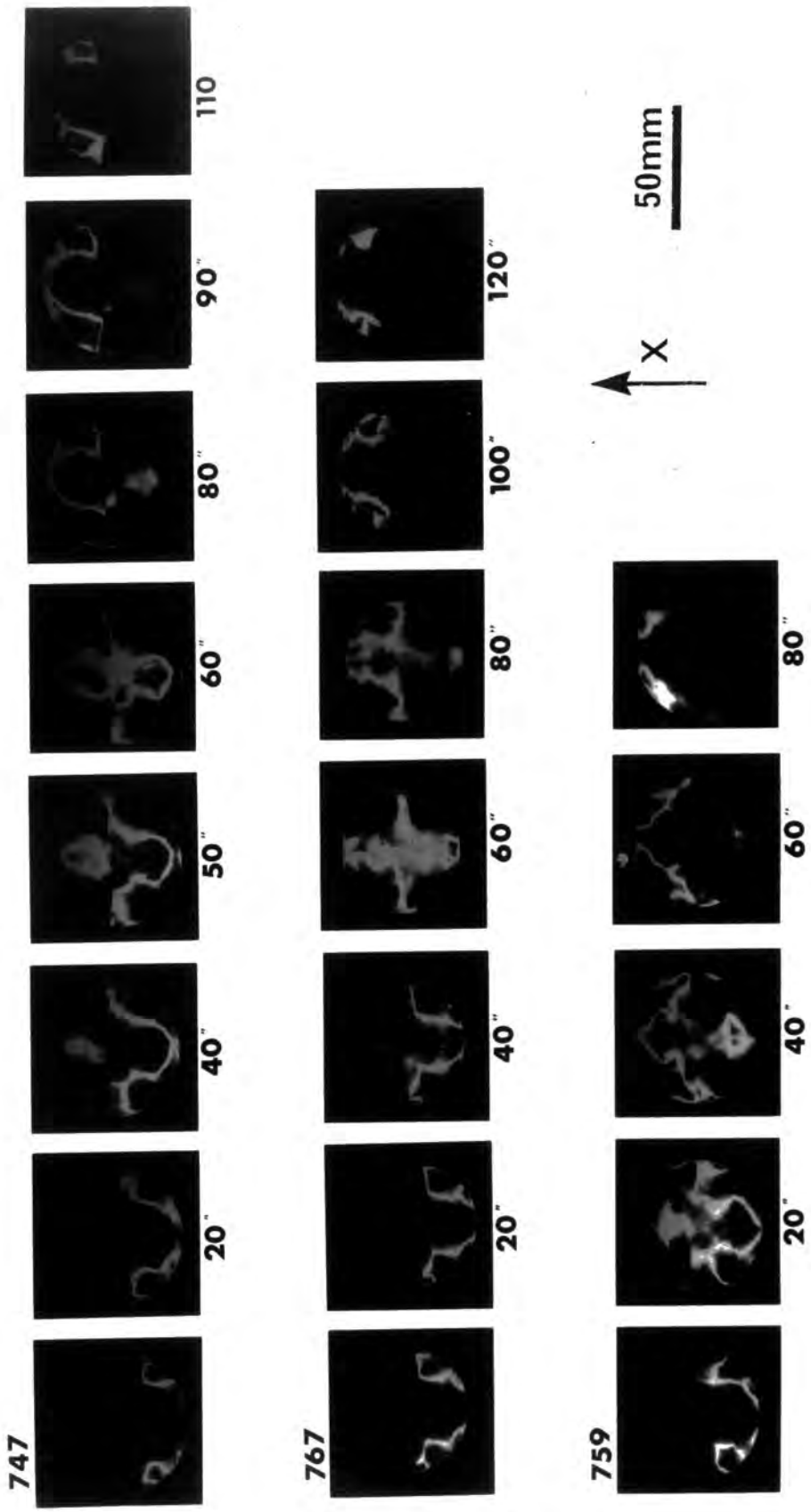

Fig.3.2a: Sequence of double crystal topographs of samples 747, 767, 759 (422 reflection at 1.5A)

Fig. 3.2b: Sequence of double crystal topographs for annealed and unannealed samples (422 reflection at 1.5A)

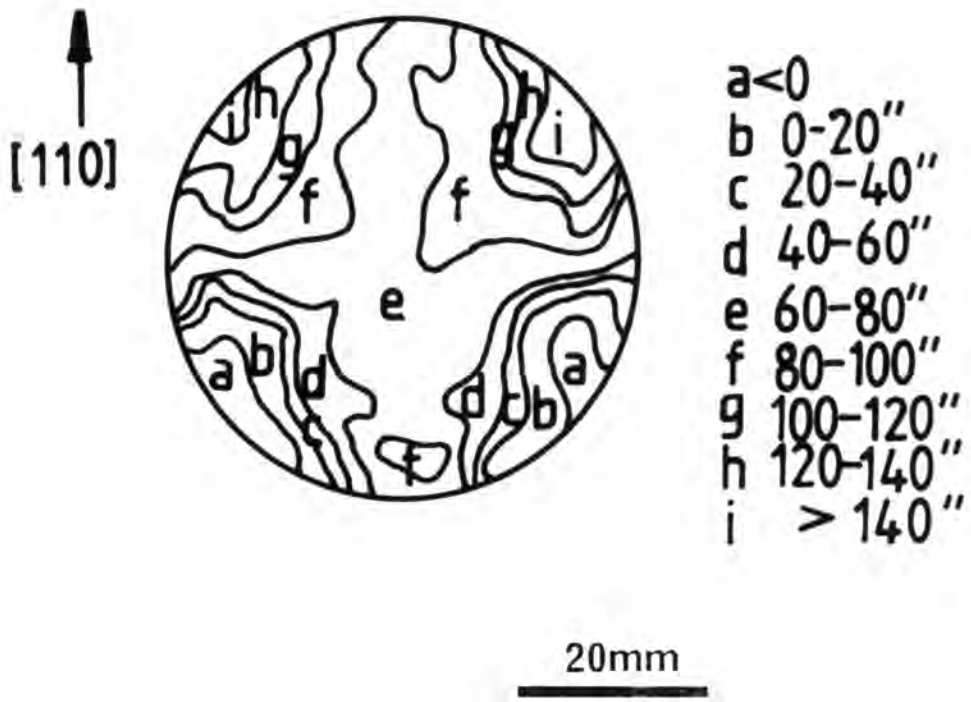

Fig. 3.3: Bragg Angle map of sample 767 taken from the series of topographs in Fig. 3.2a

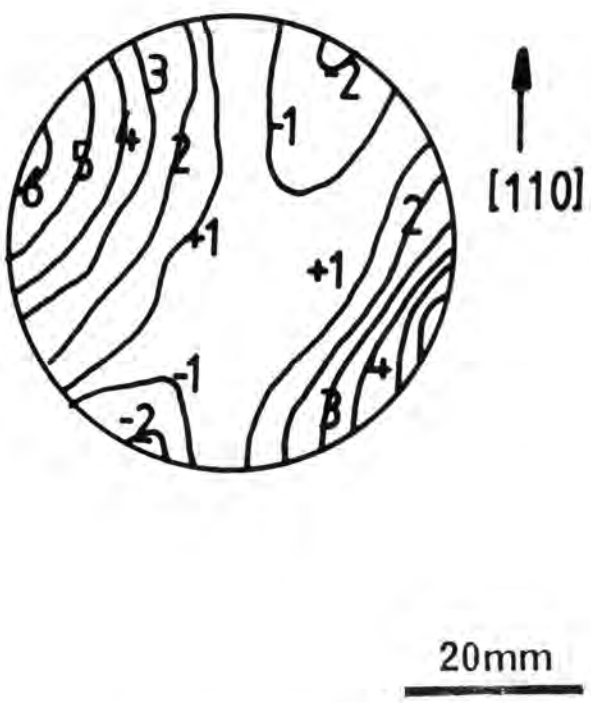

Fig. 3.4: Map of the warpage present in sample 767, in units of 1 μm

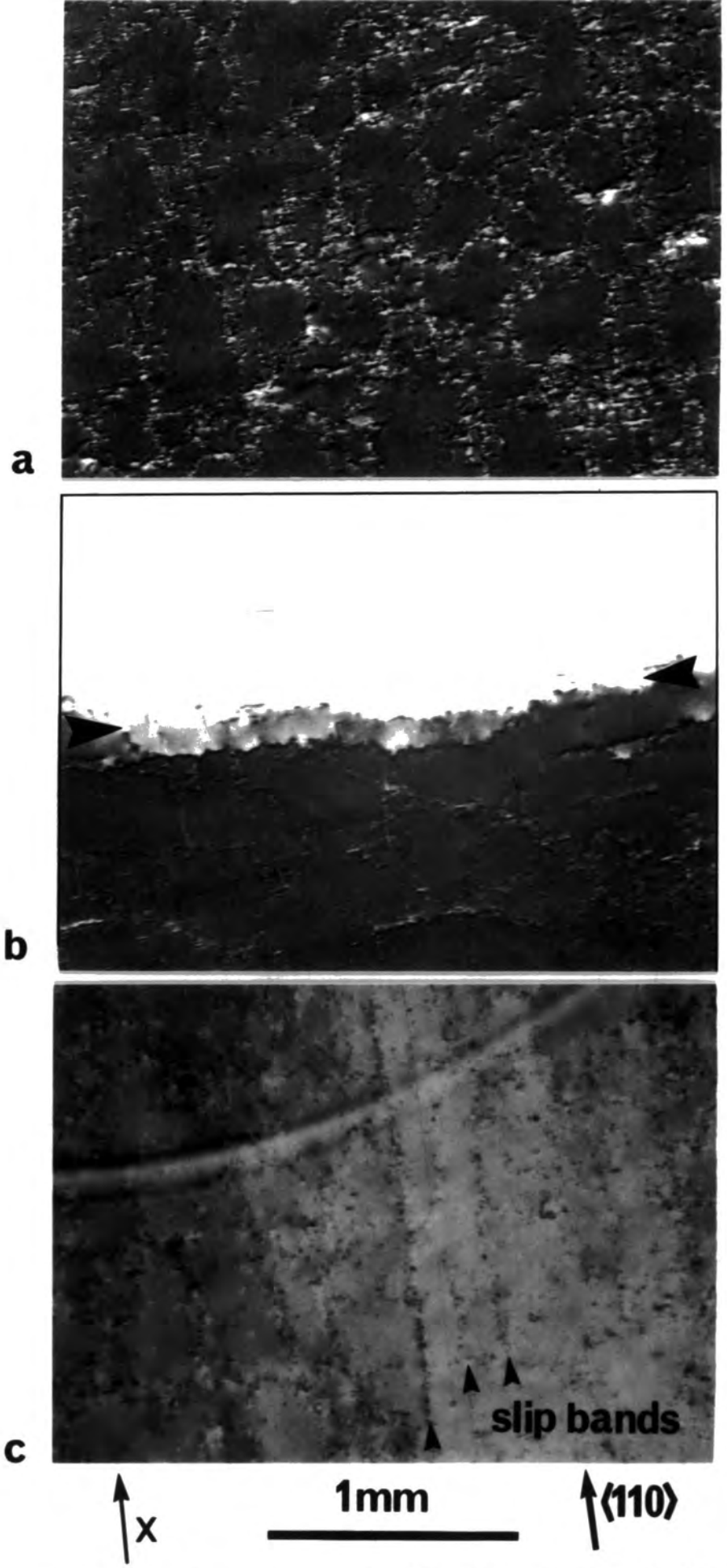

Fig.3.5: Double crystal topographs using 422 reflection at 1.5A showing typical examples of a) cell structure, b) lineage featuere, c) slip bands

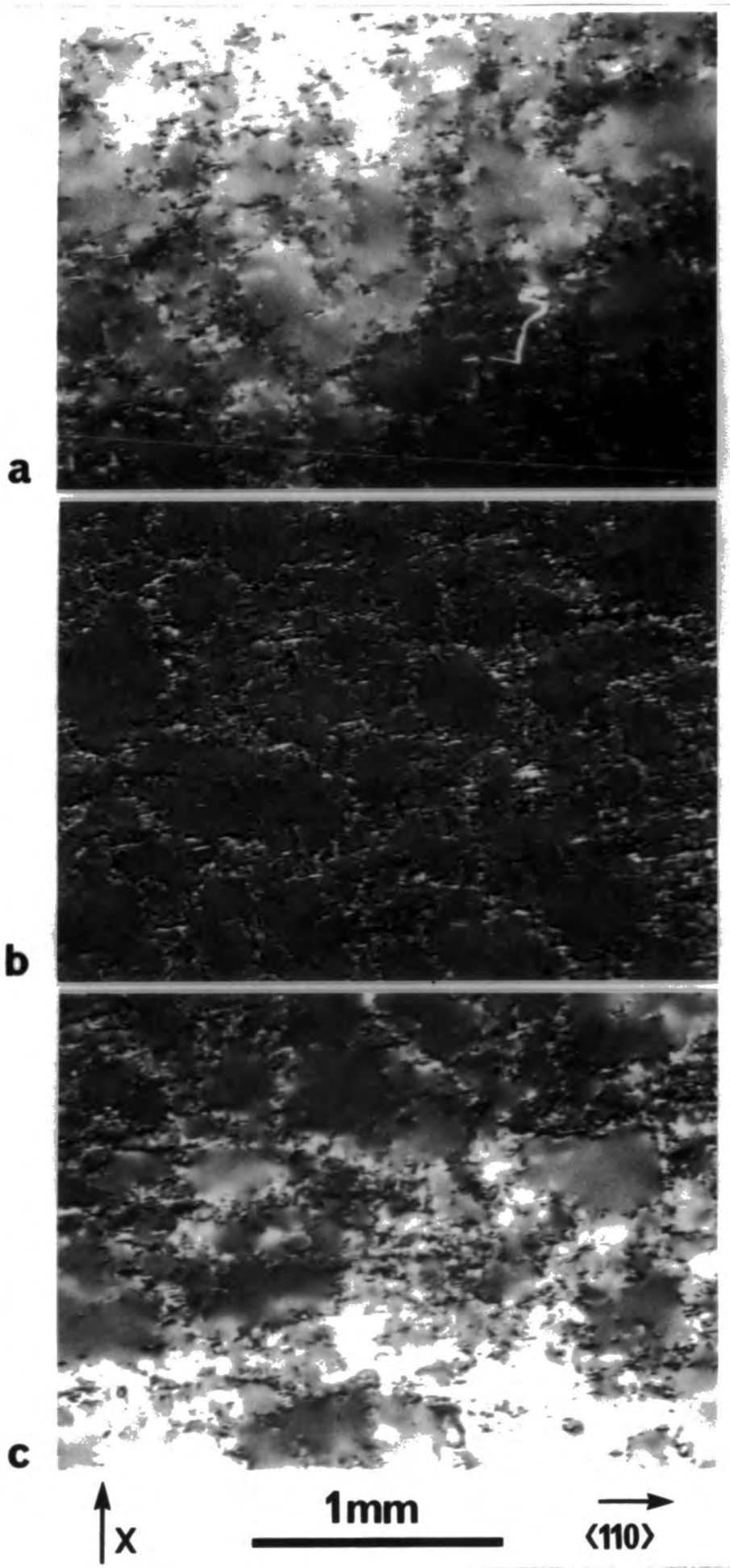

Fig. 3.6: Topographs of typical cell structure taken at three different points on the rocking curve: (a) high angle flank; (b) peak; (c) low angle flank

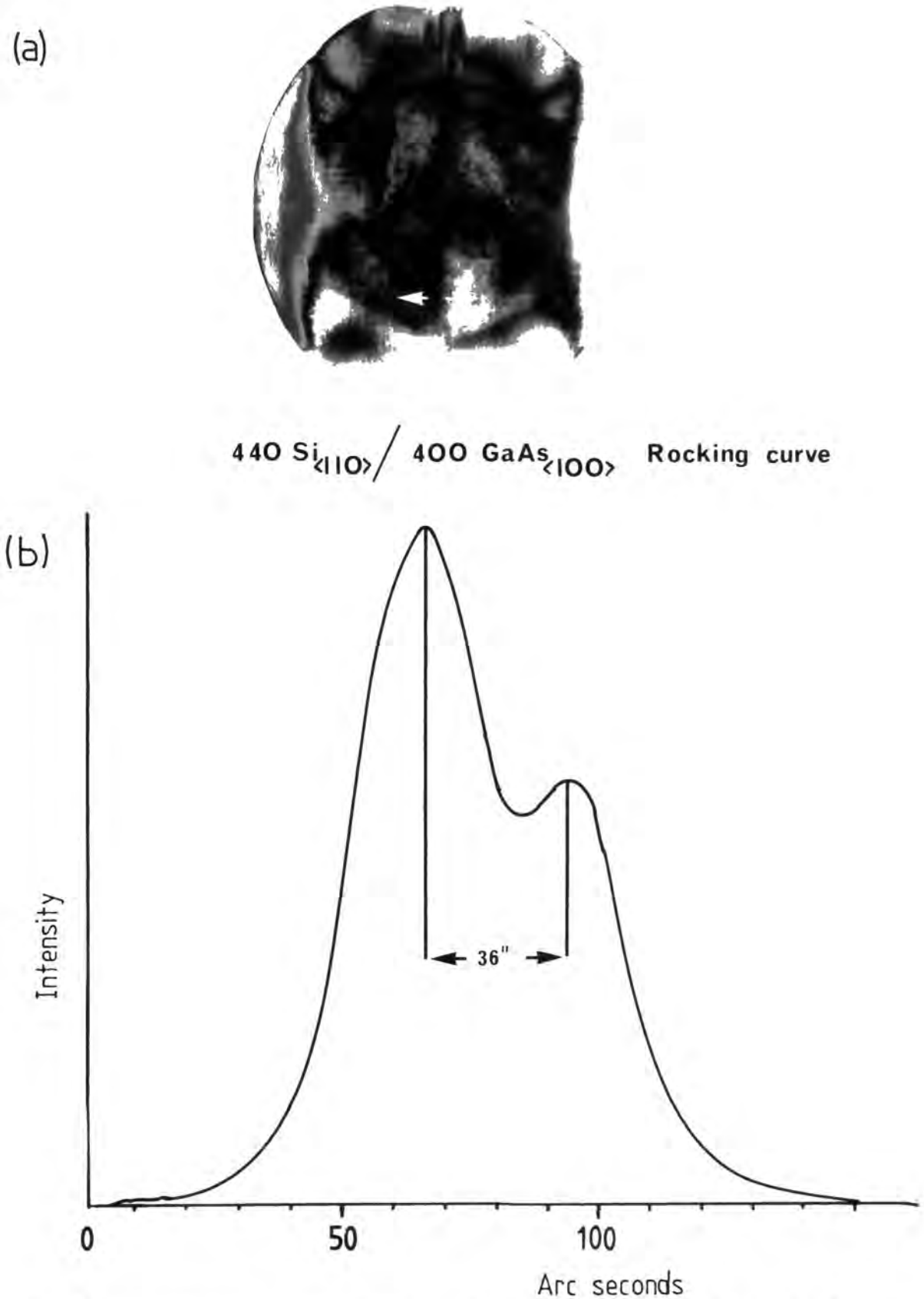

Fig. 3.7: a) double crystal topograph of the 50mm GaAs slice used for the rocking curve experiment, 422 reflection using Cu Kα radiation. The line across the lineage feature shows the position of the beam used for the rocking curve measurement; b) Rocking curve taken using the 400 reflection at 1.5Å and the double crystal Si monochrometer on the SR source

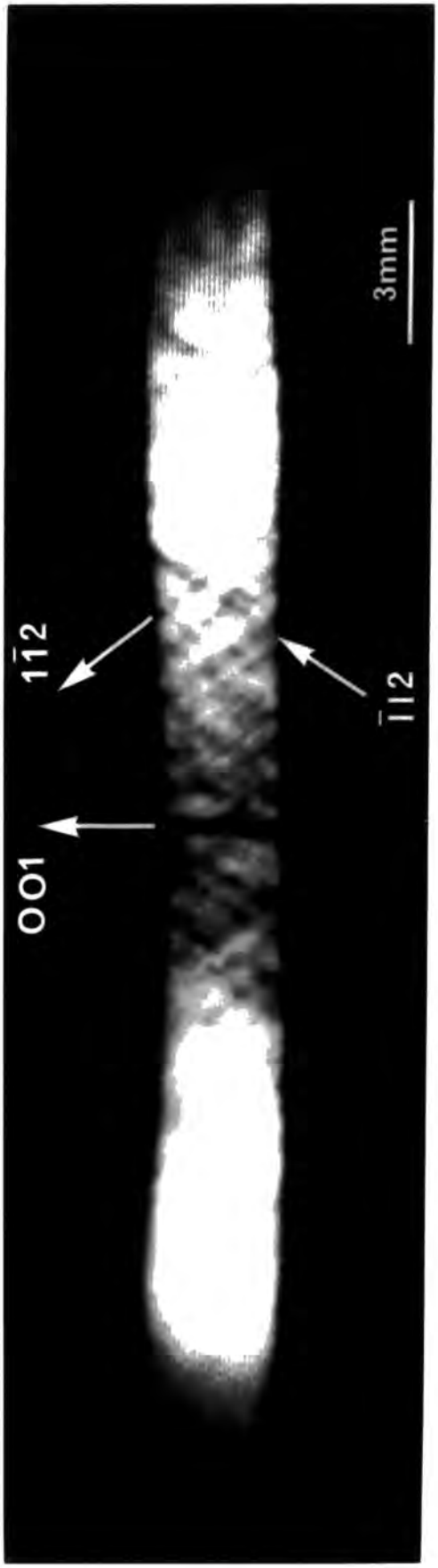

Fig. 3.8: Transmission IR micrograph of a <110> cross-section cut normal to the growth axis. Dark contrast indicates increased IR absorption.

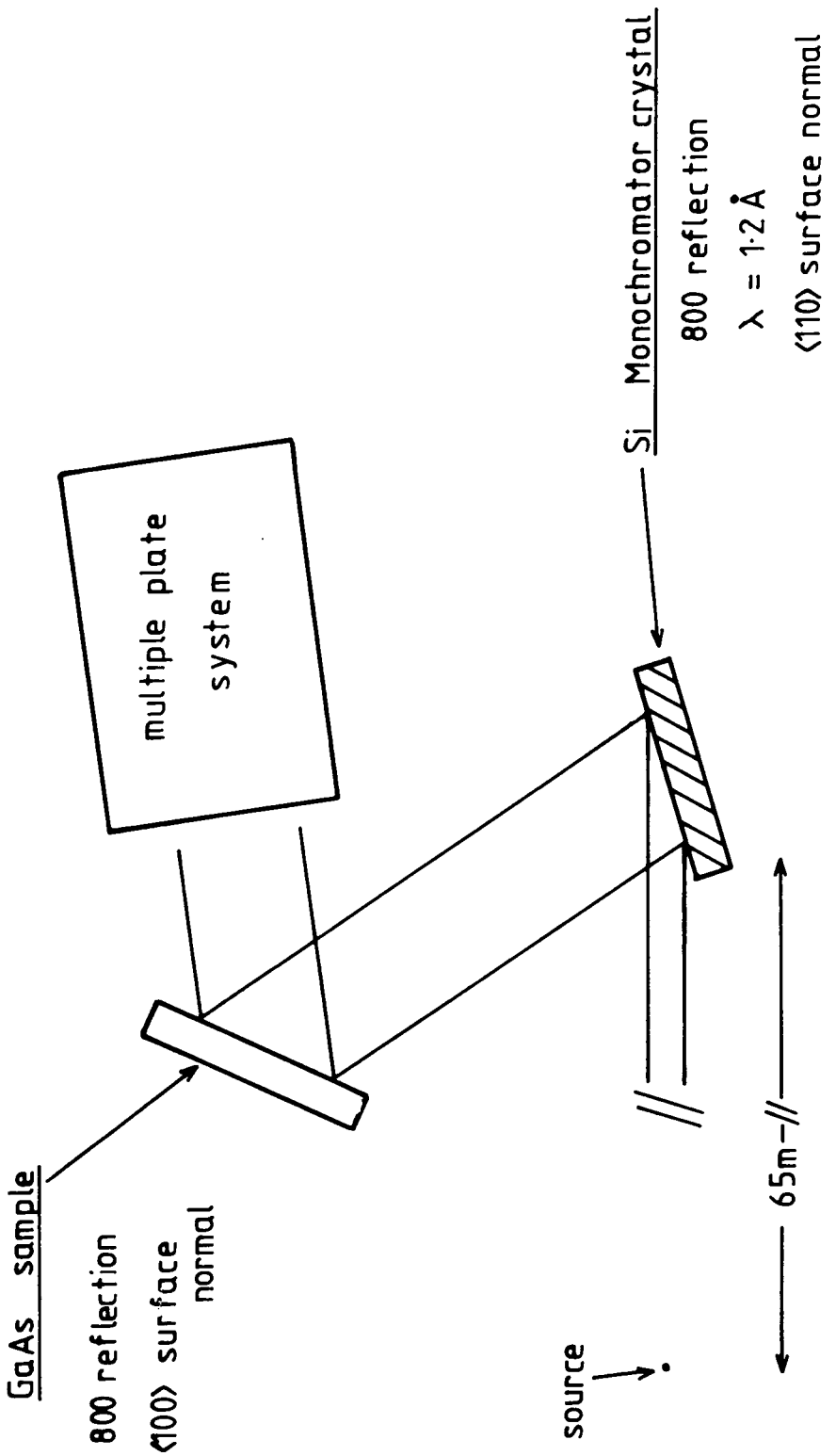

Fig. 3.9: Diffraction geometry used for the relative lattice tilt and strain measurements

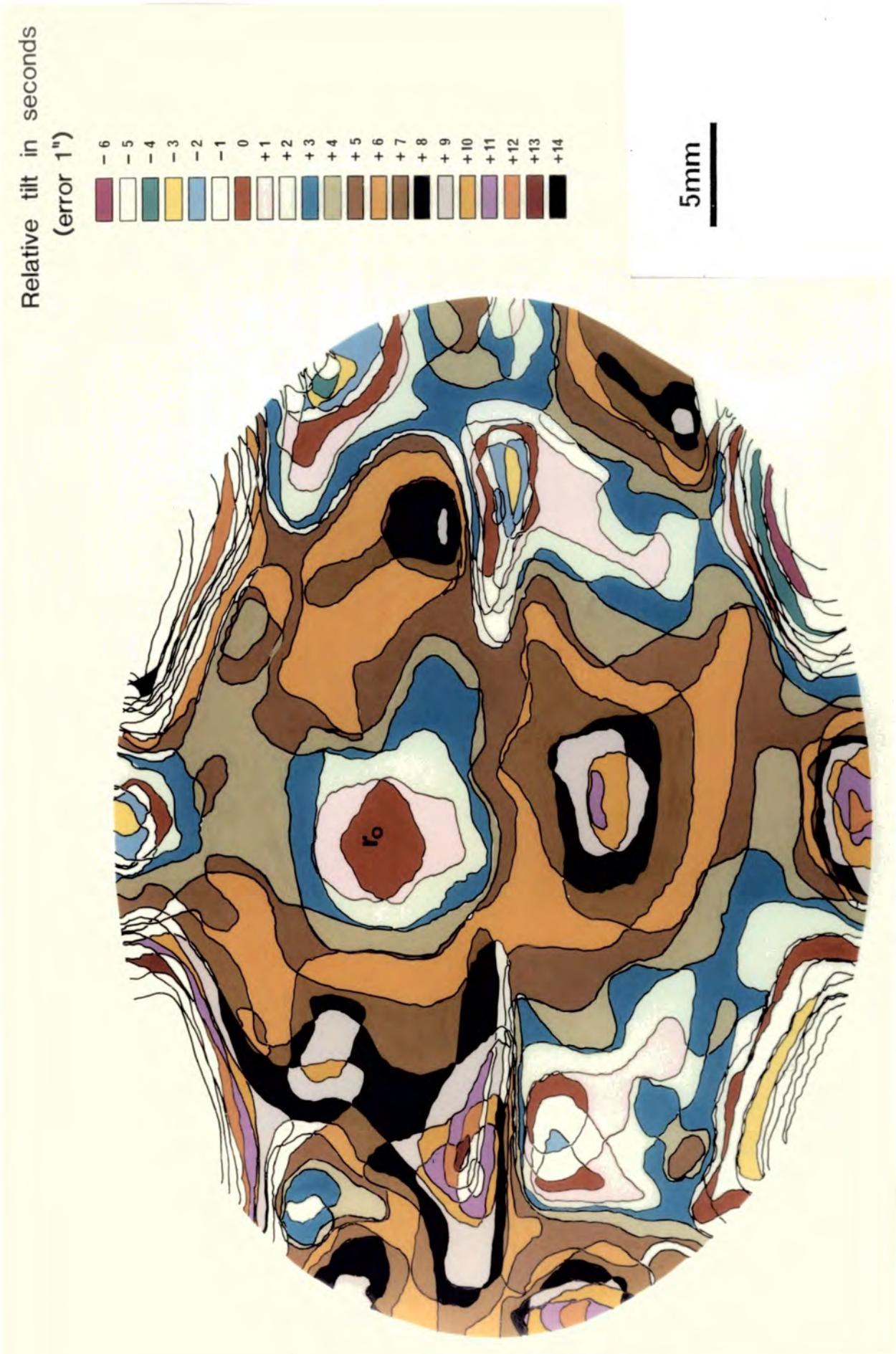

Fig. 3.10: Relative lattice tilt map of the Wacker low pressure GaAs sample. All values are relative to position r_o

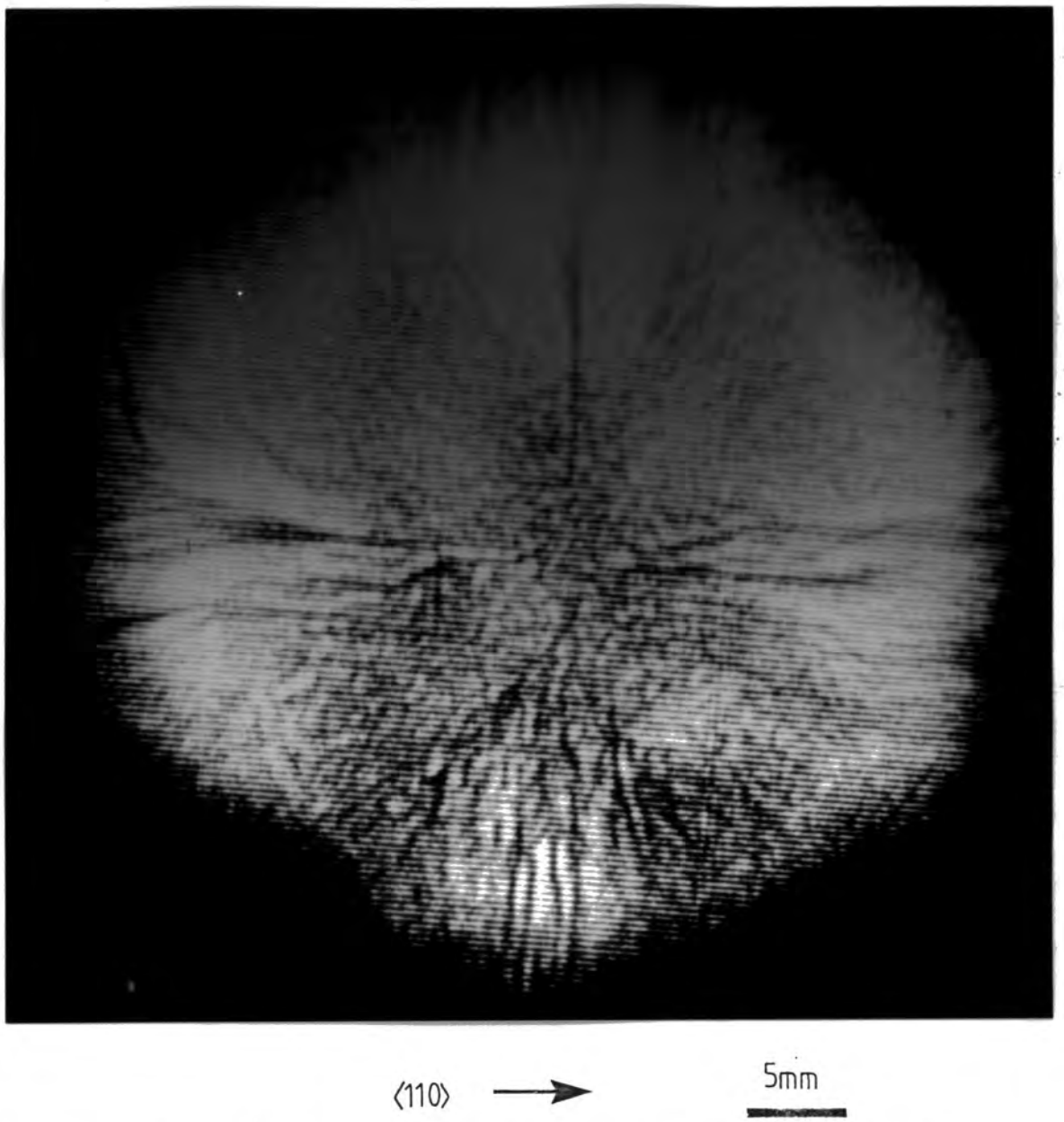

Fig. 3.11: Transmission IR micrograph of the Wacker low pressure GaAs sample. Dark contrast indicates increased absorption

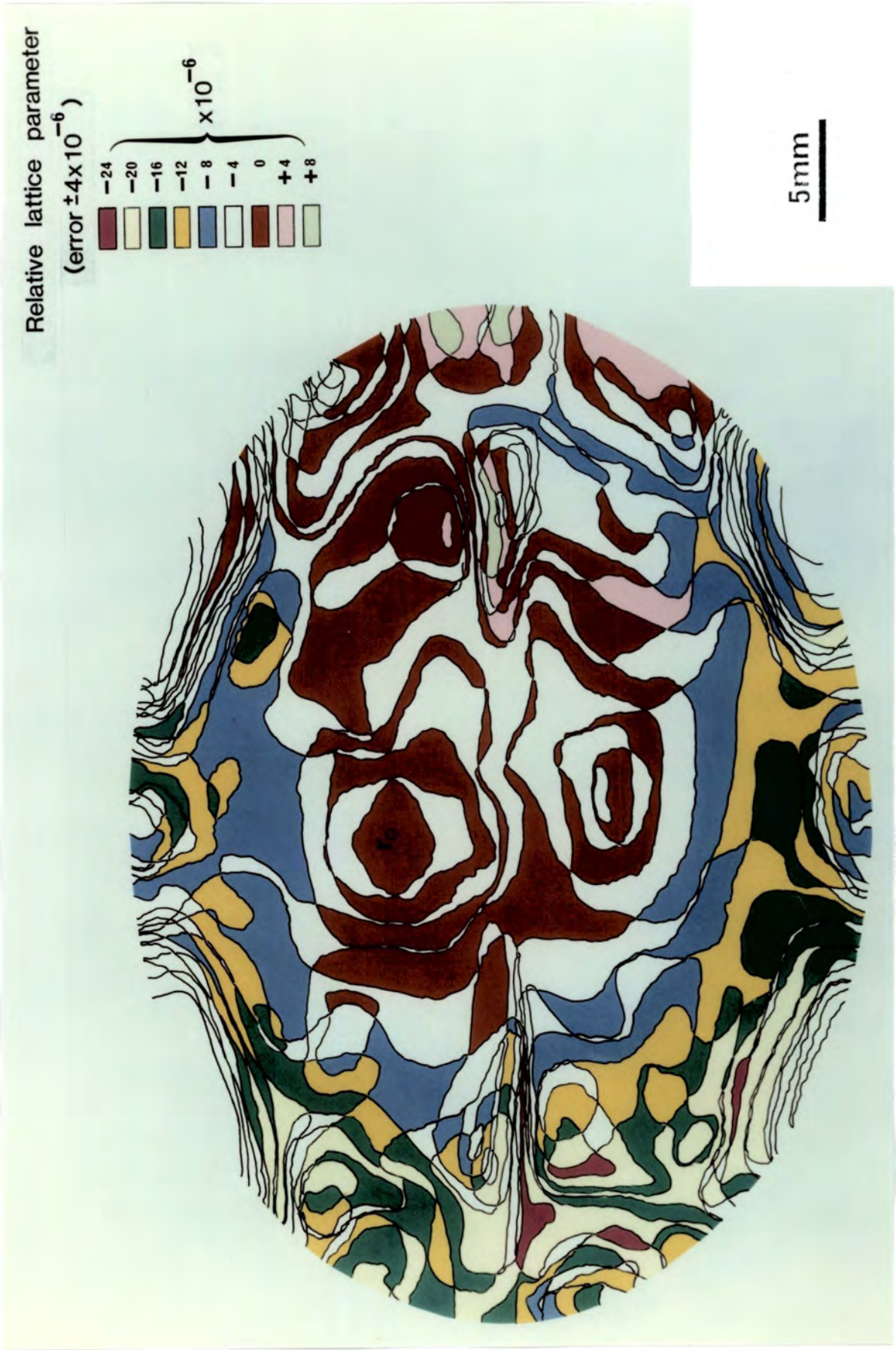

Fig. 3.12: Relative lattice strain map of the Wacker low pressure GaAs sample. All values are relative to position r_o

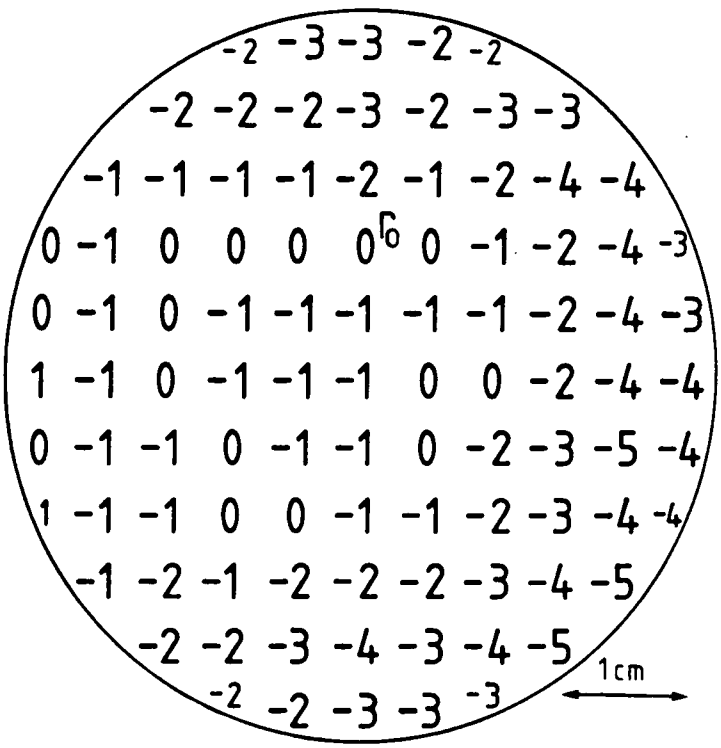

Fig. 3.13: Averaged lattice strain values for the map shown in Fig. 3.12 in units of 3.9×10^{-6}

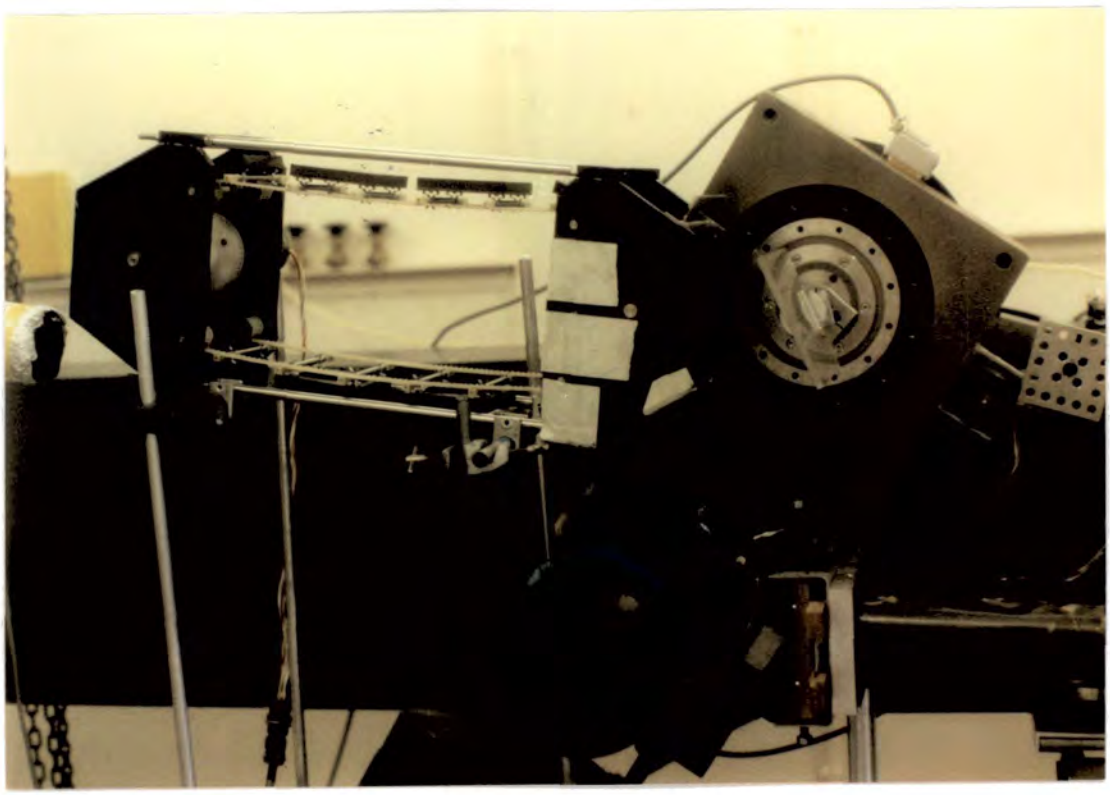

(i) – double crystal diffractometer
(ii) – incident beam pipe
(iii) – <110> cut float zone Si monochromator
(iv) – sample crystal
(v) – automatic multiple plate camera
(vi) – low resolution TV imaging system

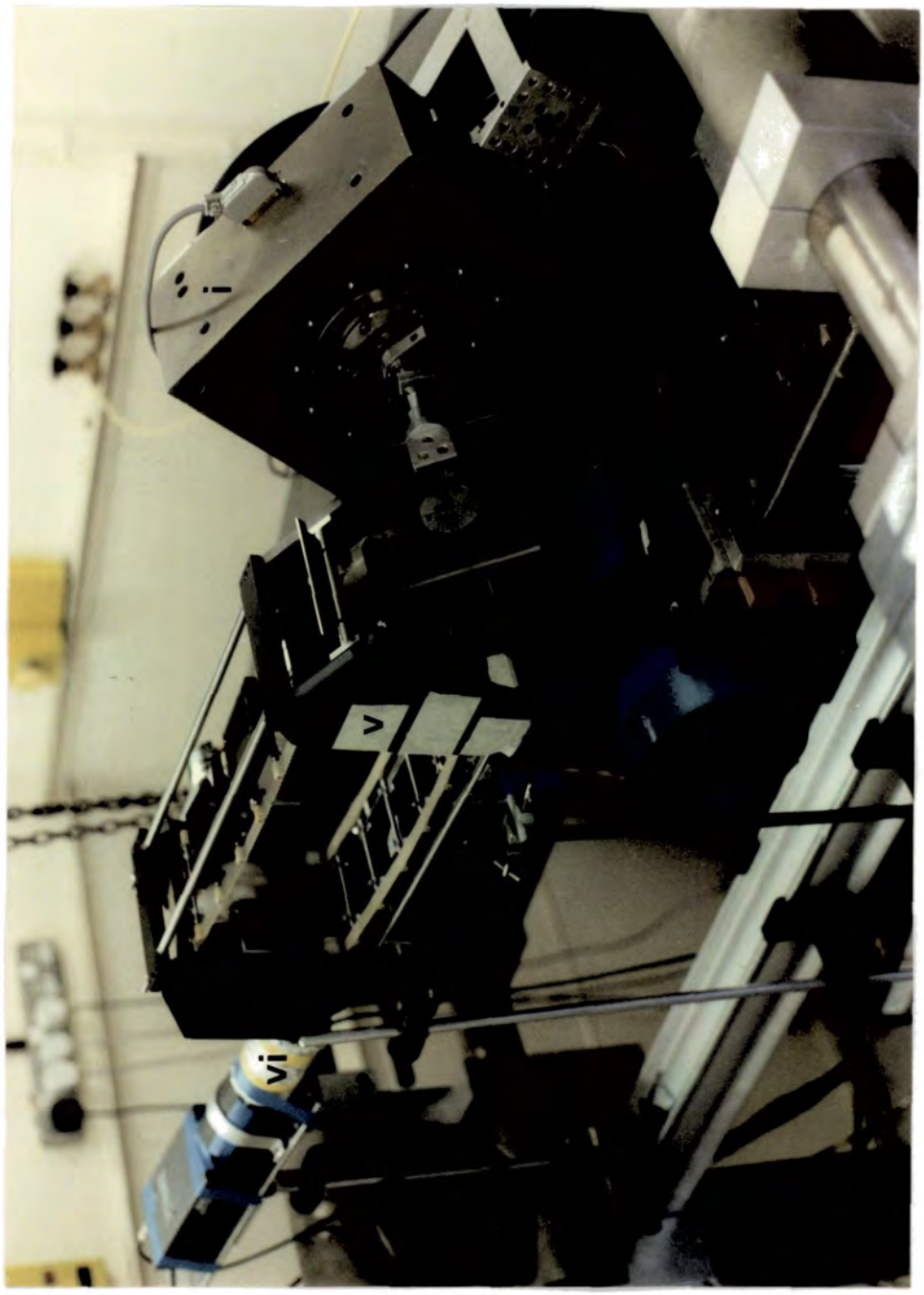

Fig. 3.14: Picture of the double crystal diffractometer as used for the lattice strain and tilt measurements

Fig. 3.15a: Composite double crystal topograph of the In-doped GaAs sample. 800 reflection at 1.2Å. The angular increment between each diffraction band is 10 arc seconds

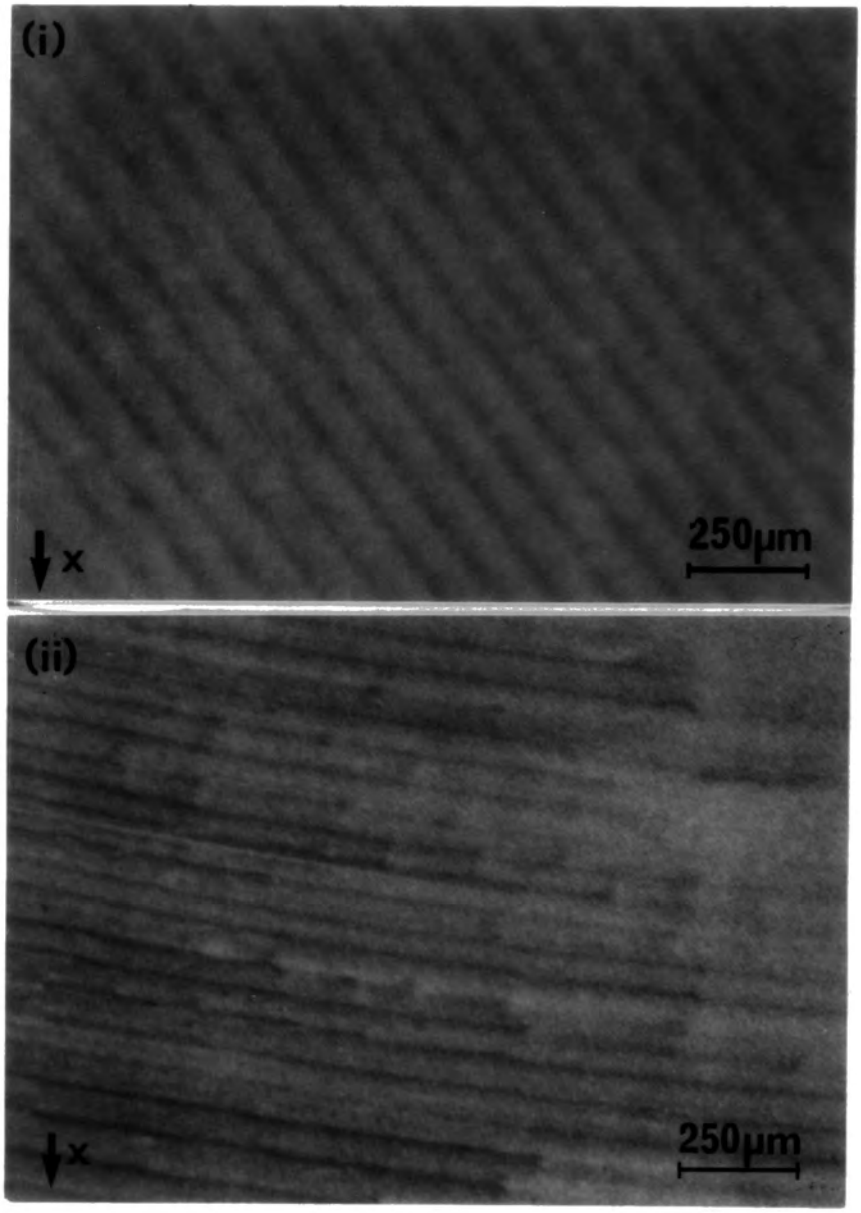

Fig. 3.15b: Enlargement of regions (i) and (ii) of Fig. 3.15a showing the contrast due to In-concentration striations.

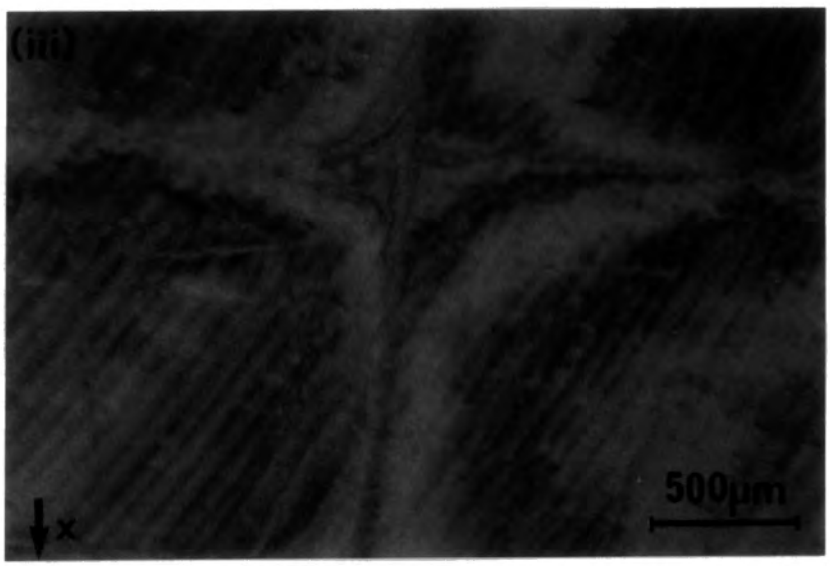

Fig. 3.15c: Enlargement of region (iii) of Fig. 3.15a showing the deformation of the diffraction contrast bands close to slip dislocations

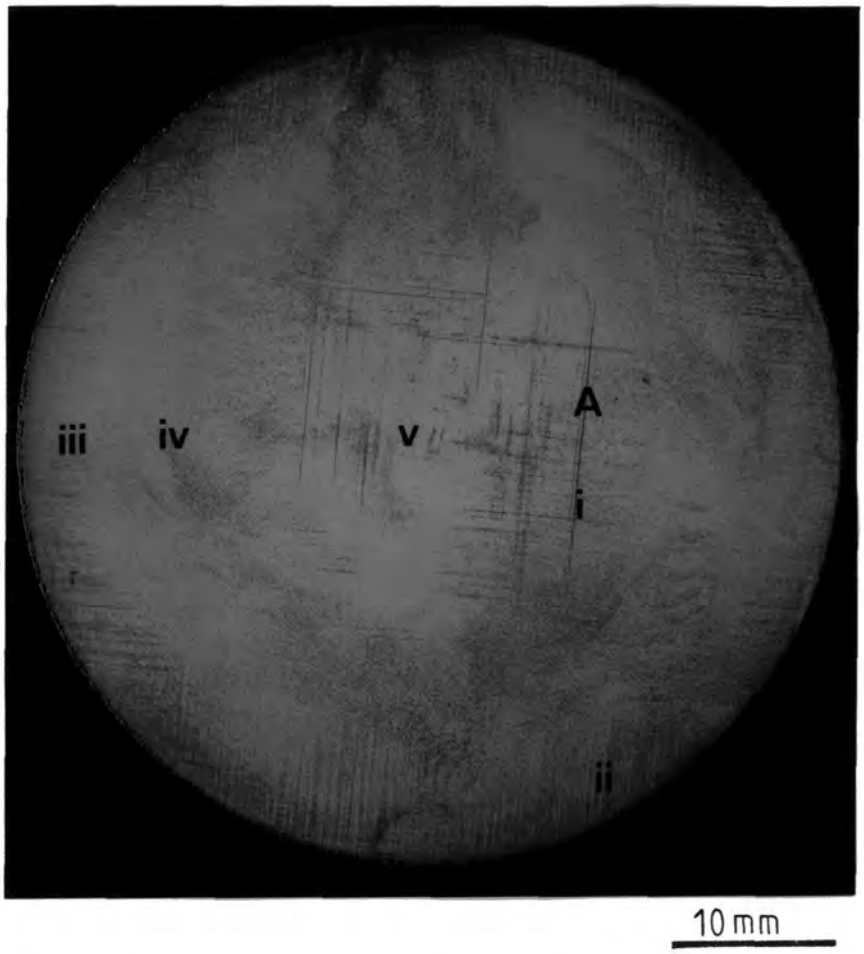

Fig.16a: Picture of the KOH etched surface of the In-doped sample

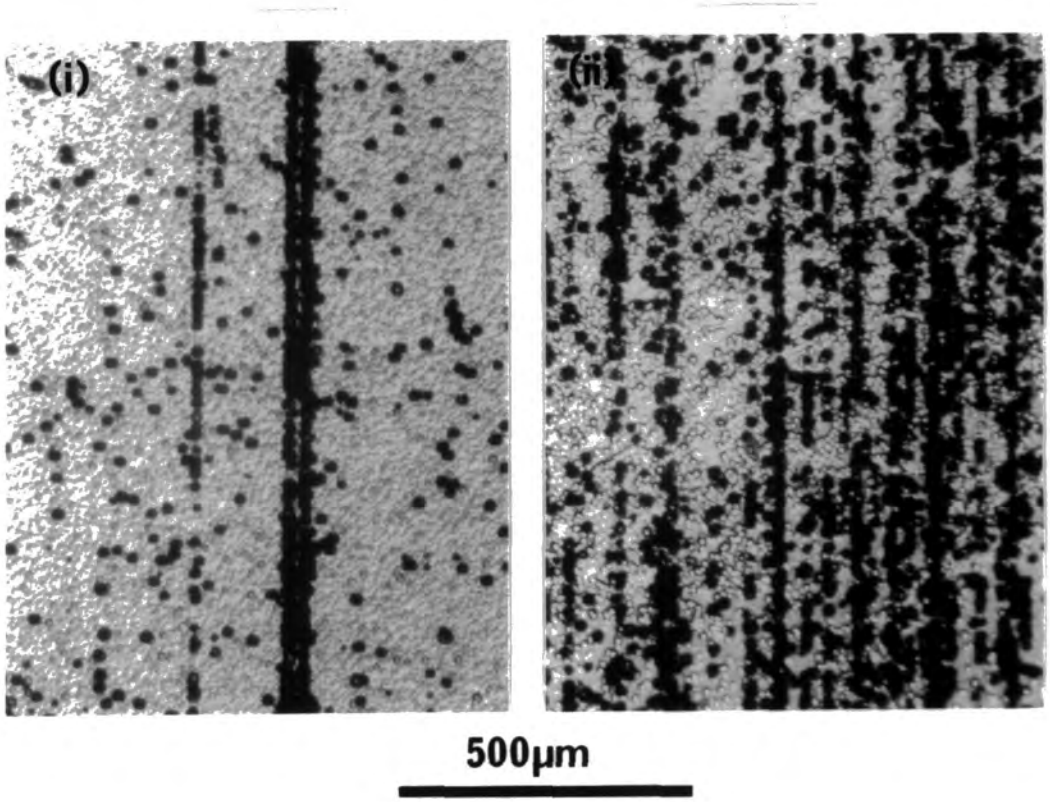

Fig.16b: Enlargement of regions (i) and (ii) of fig.3.16a.

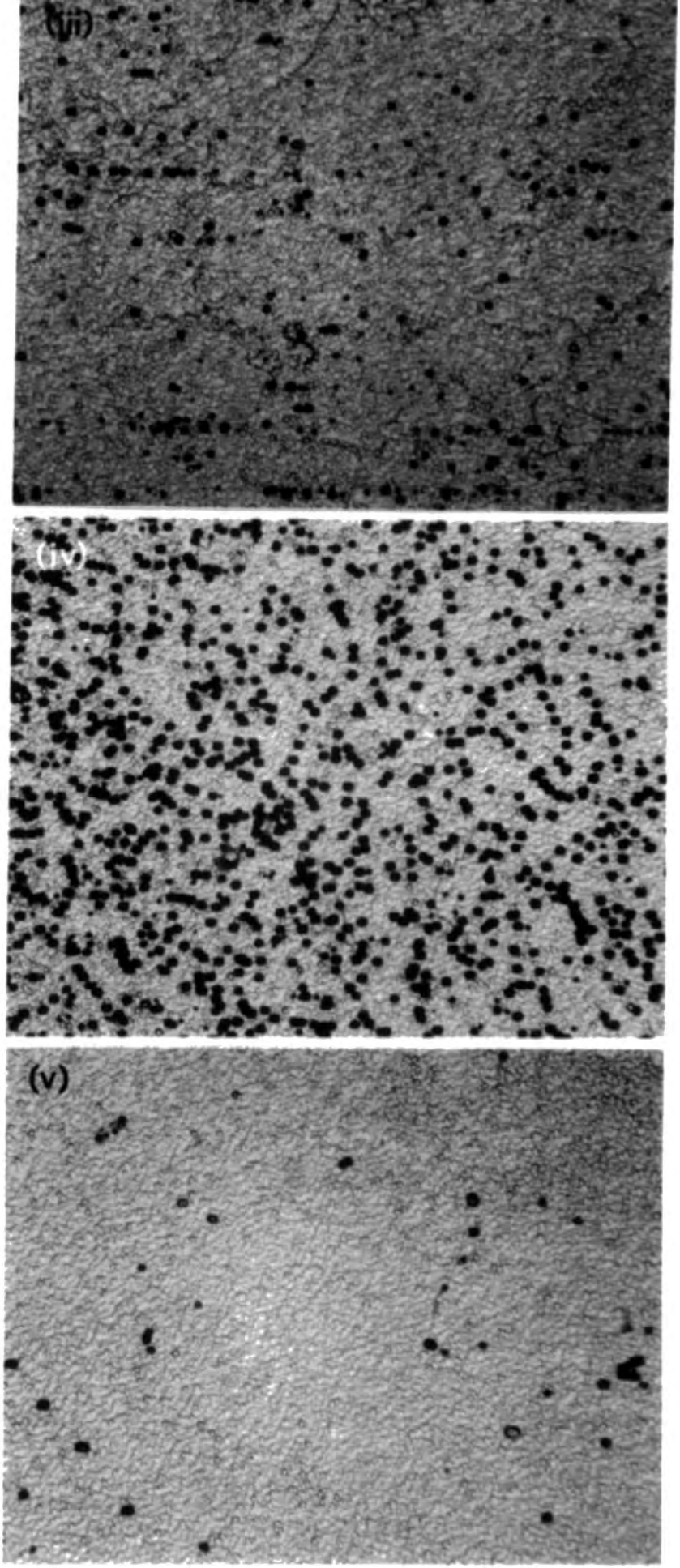

Fig.3.16c: Enlargement of regions (iii), (iv) and (v) of fig.3.16a.

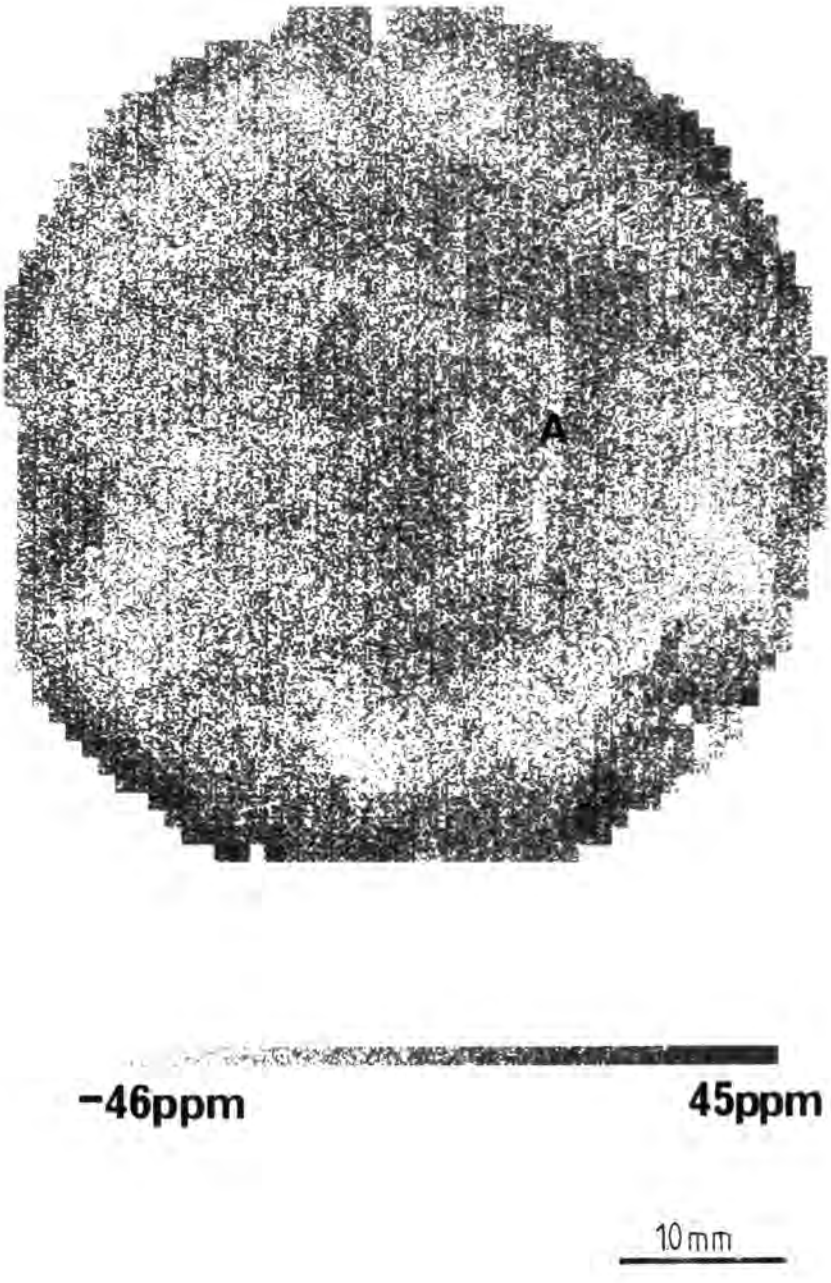

Fig. 3.17: Relative lattice strain map of the In-doped sample produced from a bit image representation on a dot matrix printer

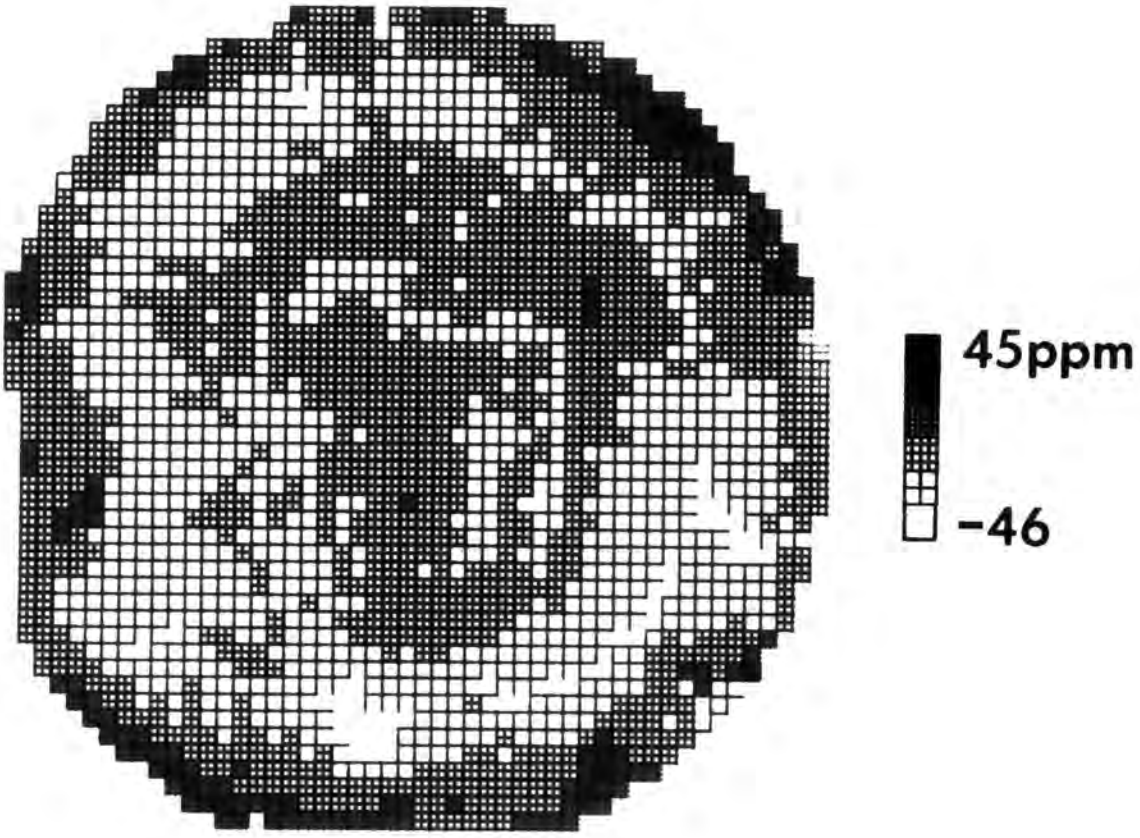

Fig. 3.18: Relative lattice strain map of the In-doped sample produced on an Epson plotter

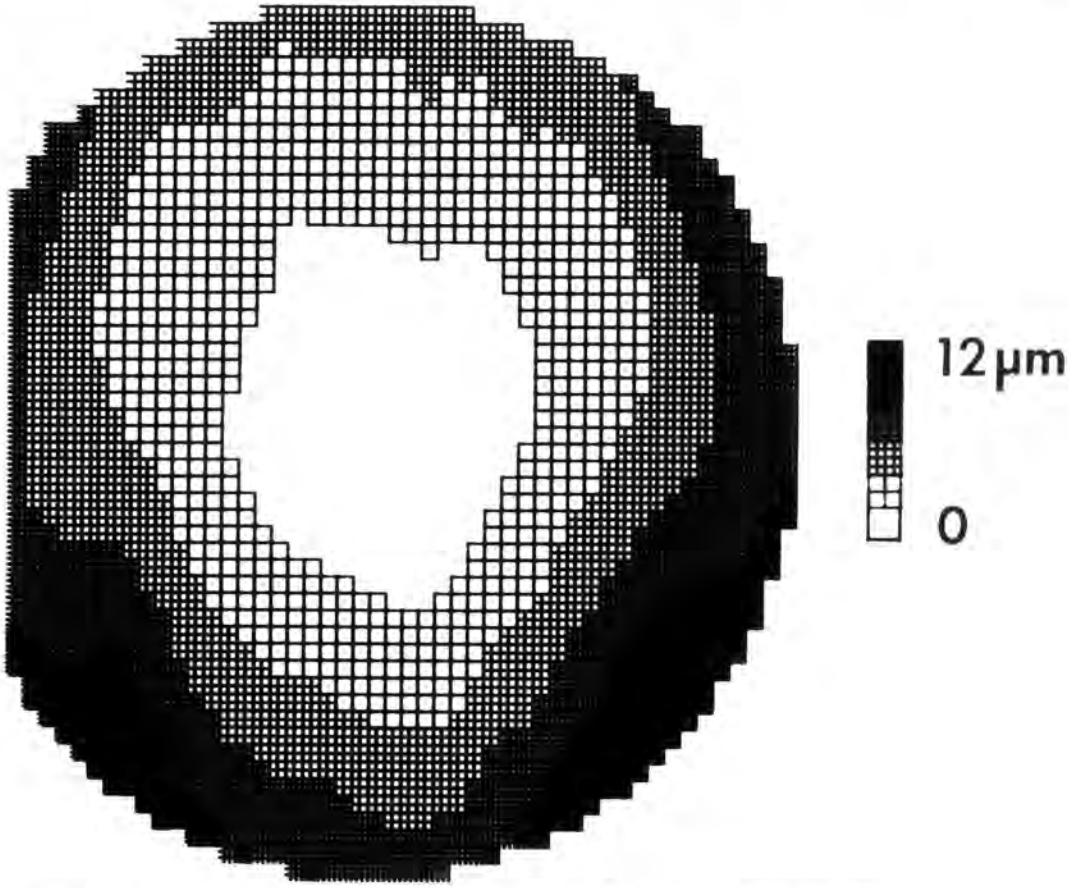

Fig. 3.19: Relative lattice displacement map of the In-doped sample

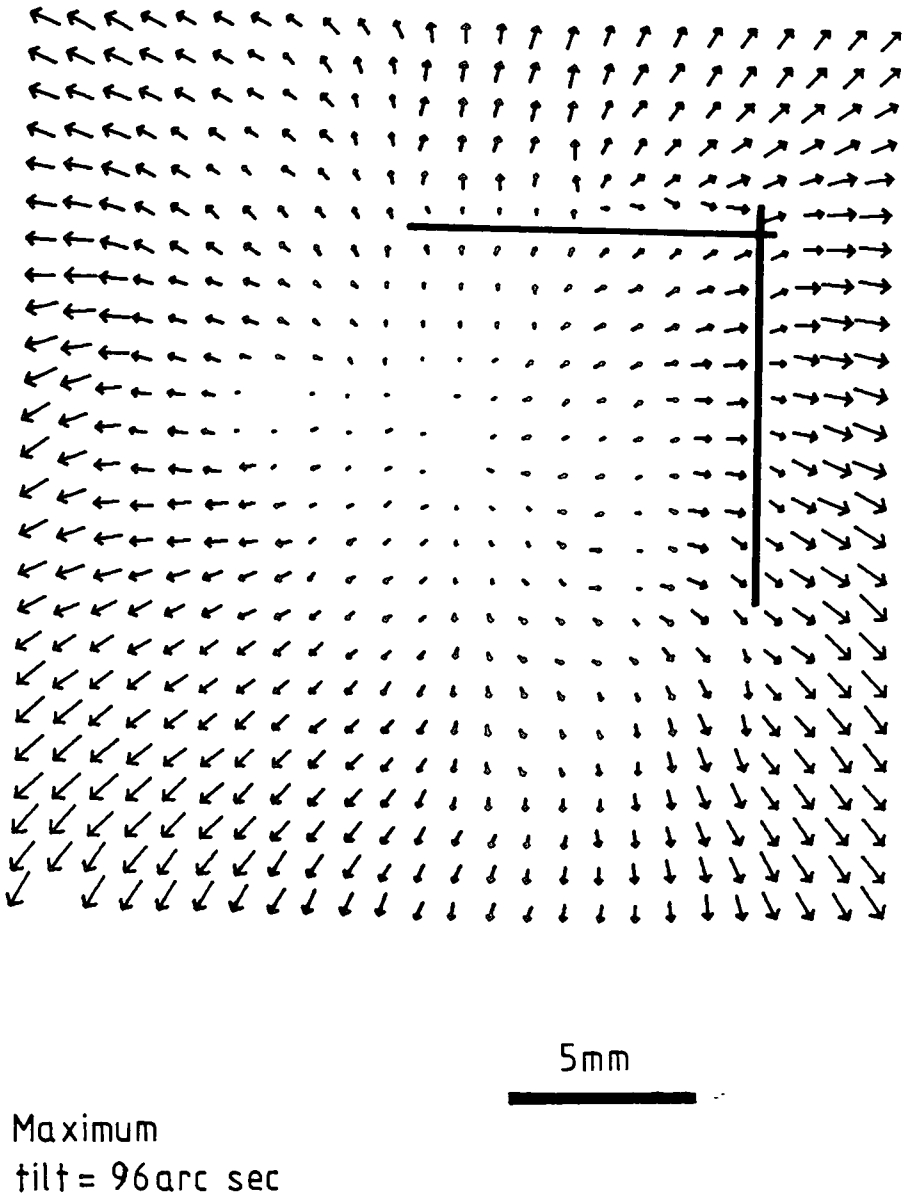

Fig. 3.20: Relative lattice tilt map of the central region of the In-doped sample. The lines show the position of isolated slip bands.

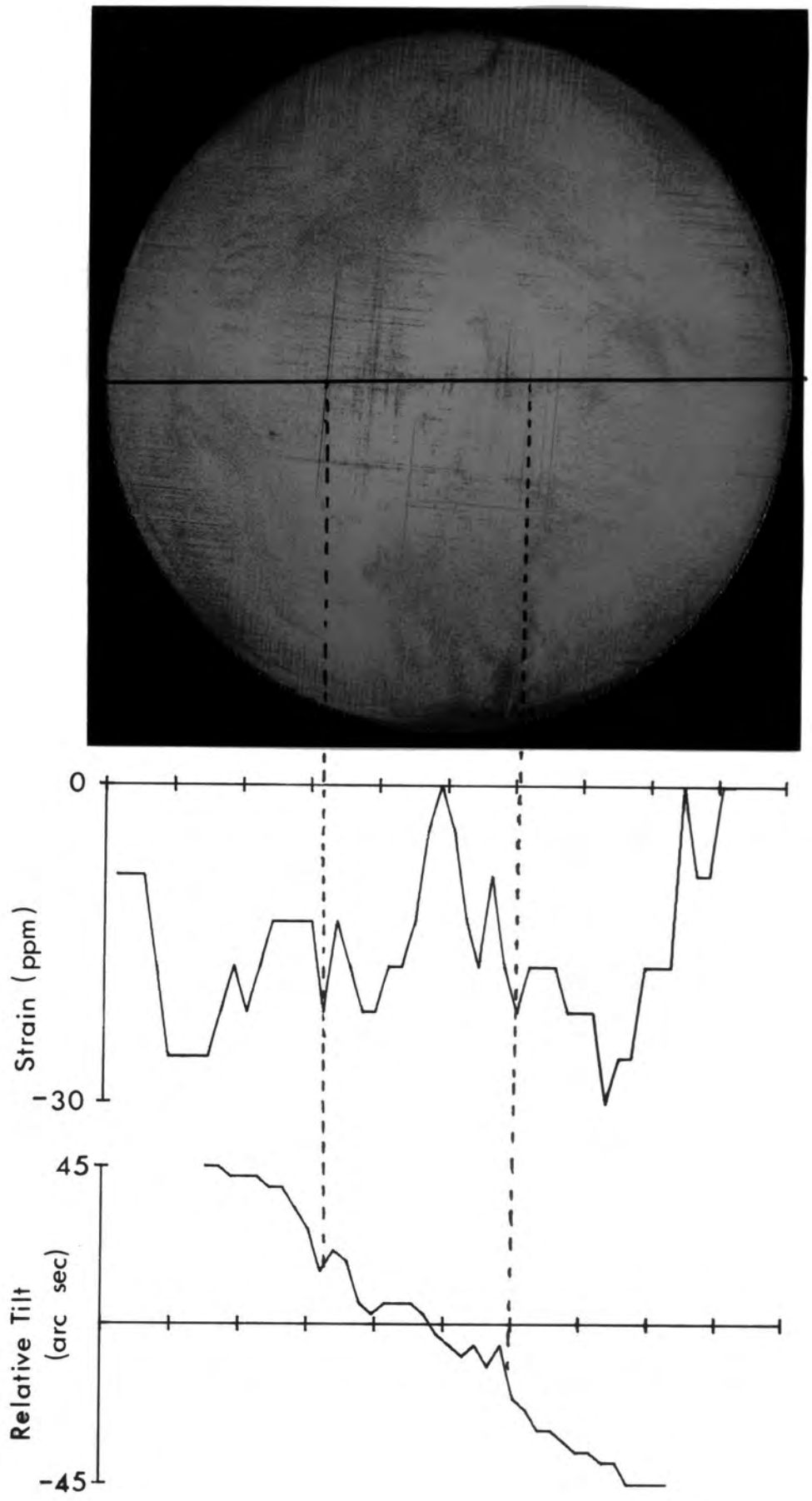

Fig. 3.21: Picture of the KOH etch surface of the In-doped sample and line scans of the strain and tilt across the <110> diameter indicated.

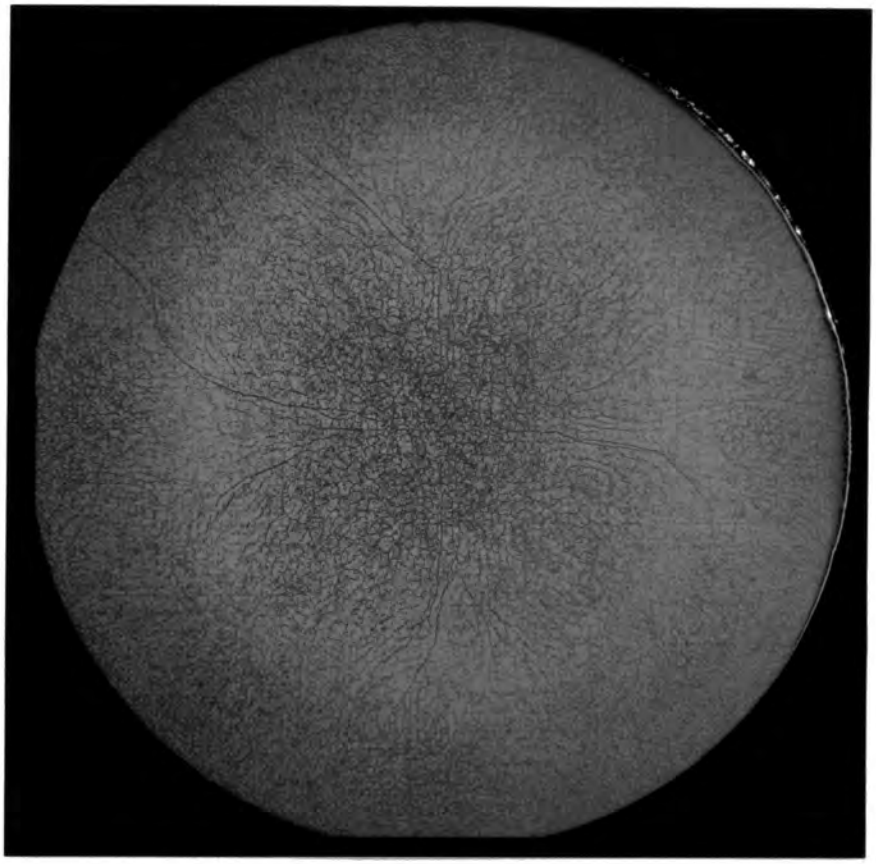

Fig. 3.22a: Sample MMT 76 T2 – KOH etch picture

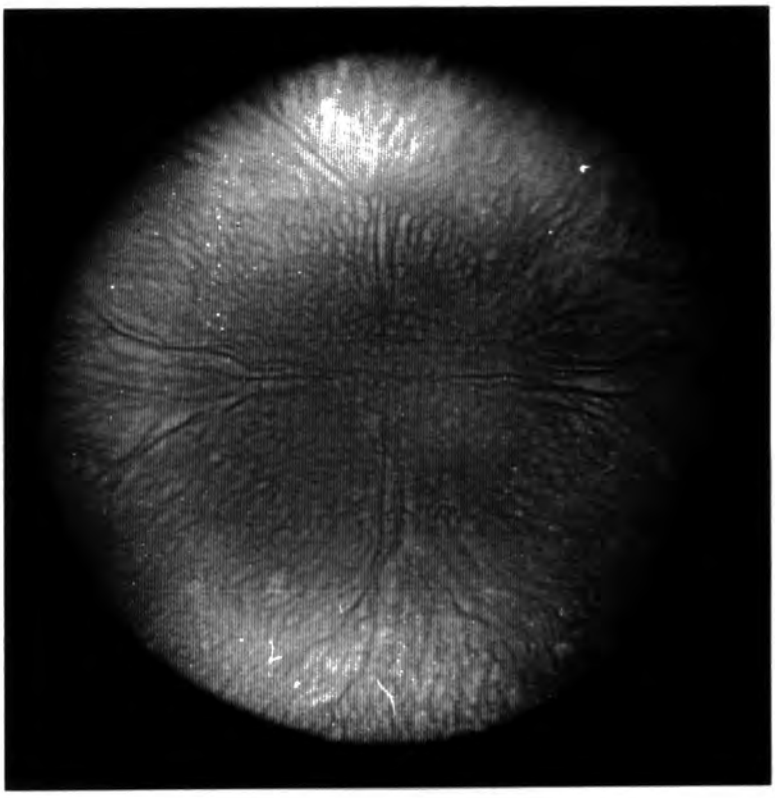

Fig. 3.22b: Sample MMT 76 T2 – transmission IR micrograph. Dark contrast indicates increased IR absorption

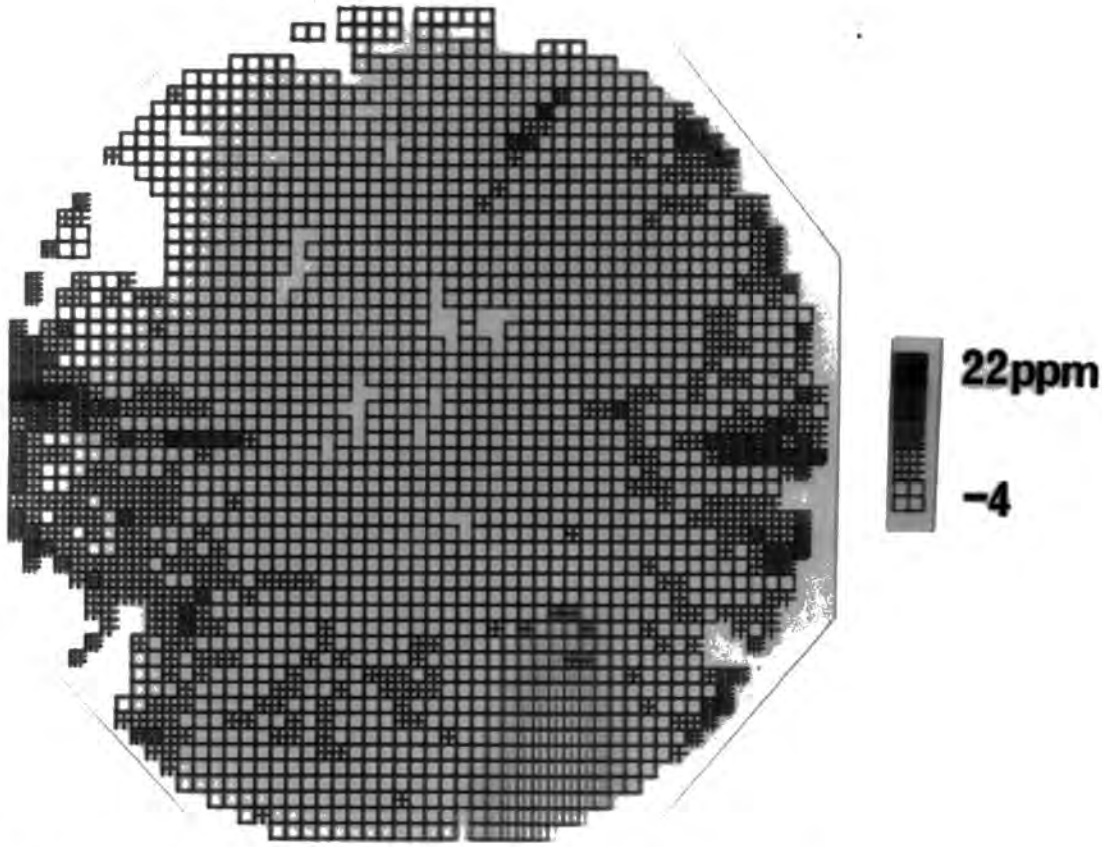

Fig. 3.22c: Sample MMT 76 T2 – relative lattice strain map

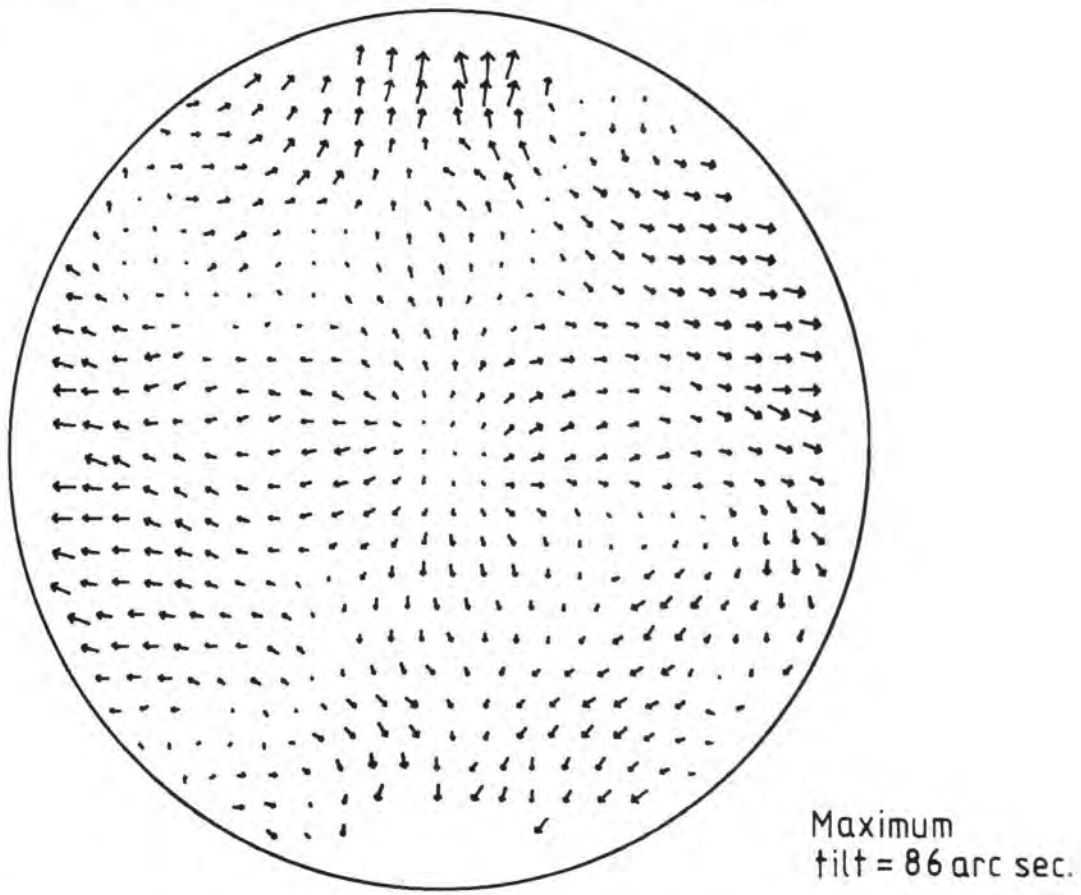

Fig. 3.22d: Sample MMT 76 T2 – relatice lattice tilt map

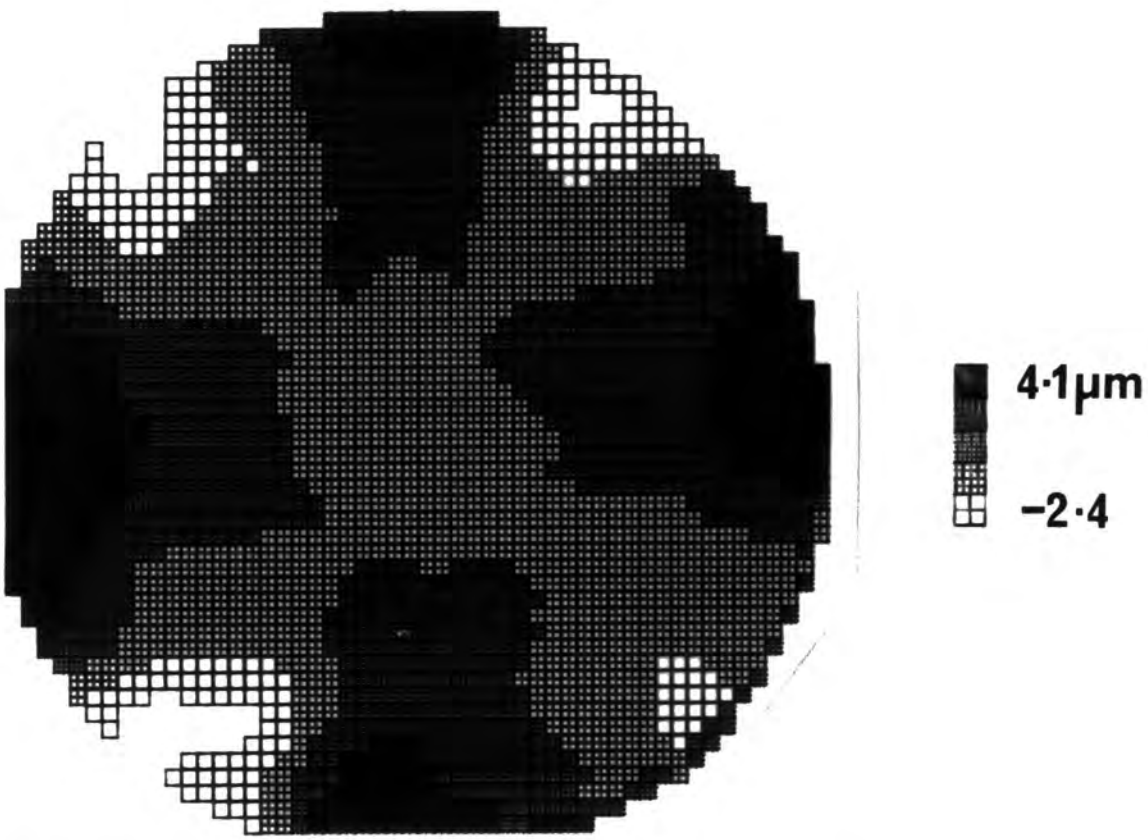

Fig. 3.22e: Sample MMT 76 T2 – relative lattice displacement map

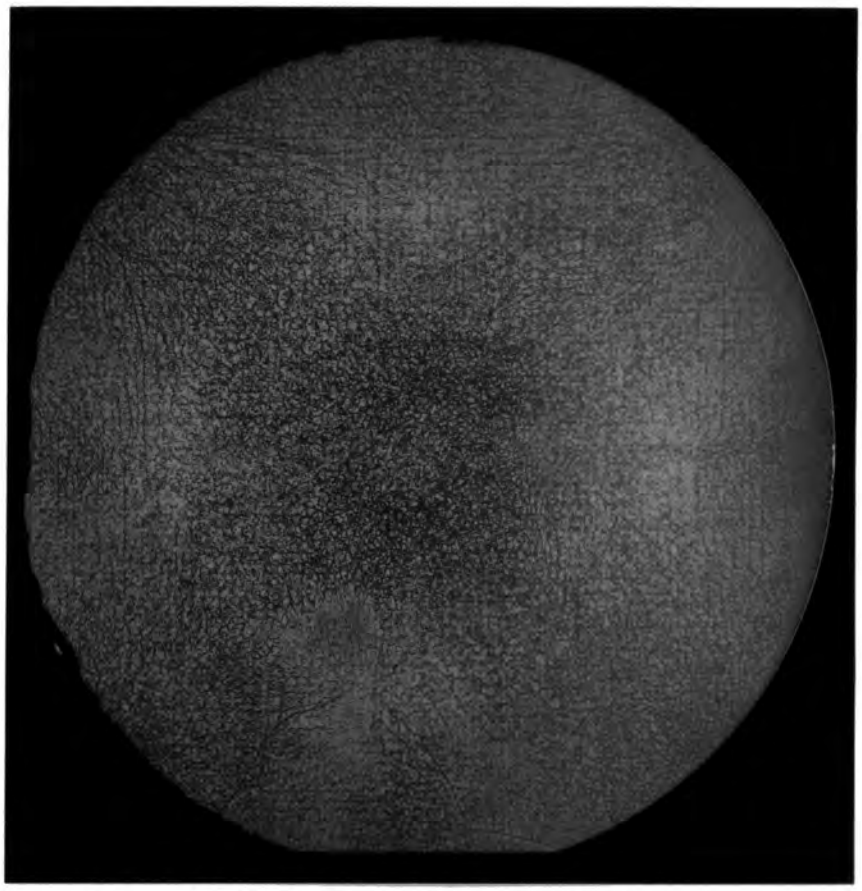

Fig. 3.23a: Sample MMT 76 B2 – KOH etch picture

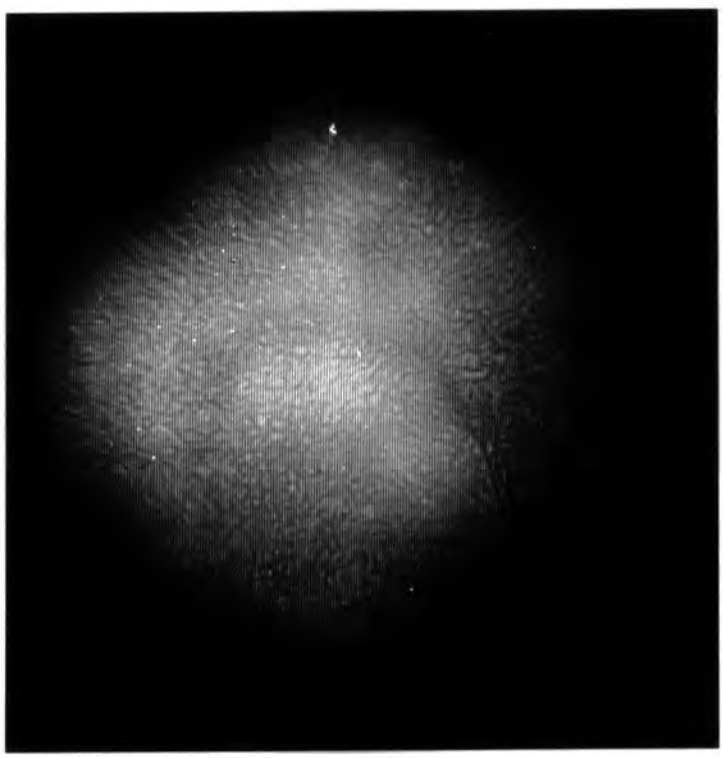

Fig. 3.23b: Sample MMT 76 B2 – transmission IR micrograph. Dark contrast indicates increased IR absorption

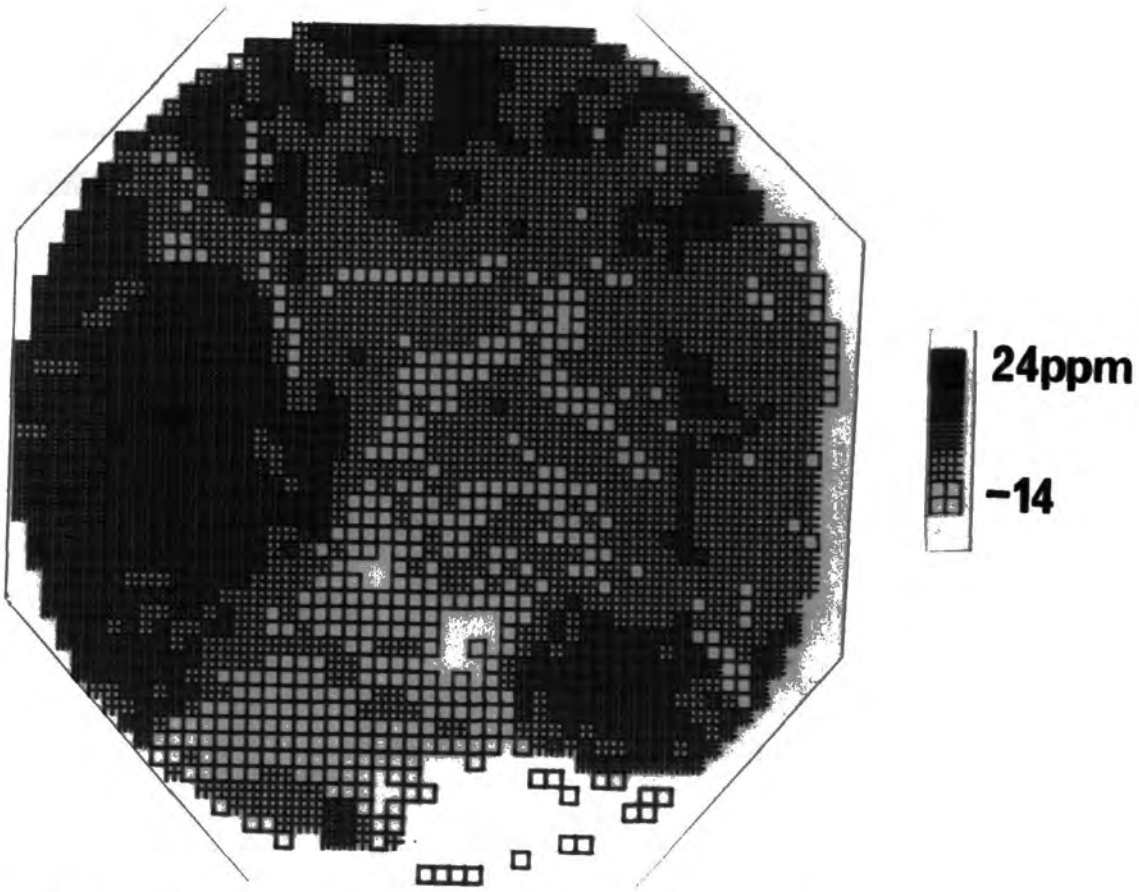

Fig. 3.23c: Sample MMT 76 B2 – relative lattice strain map

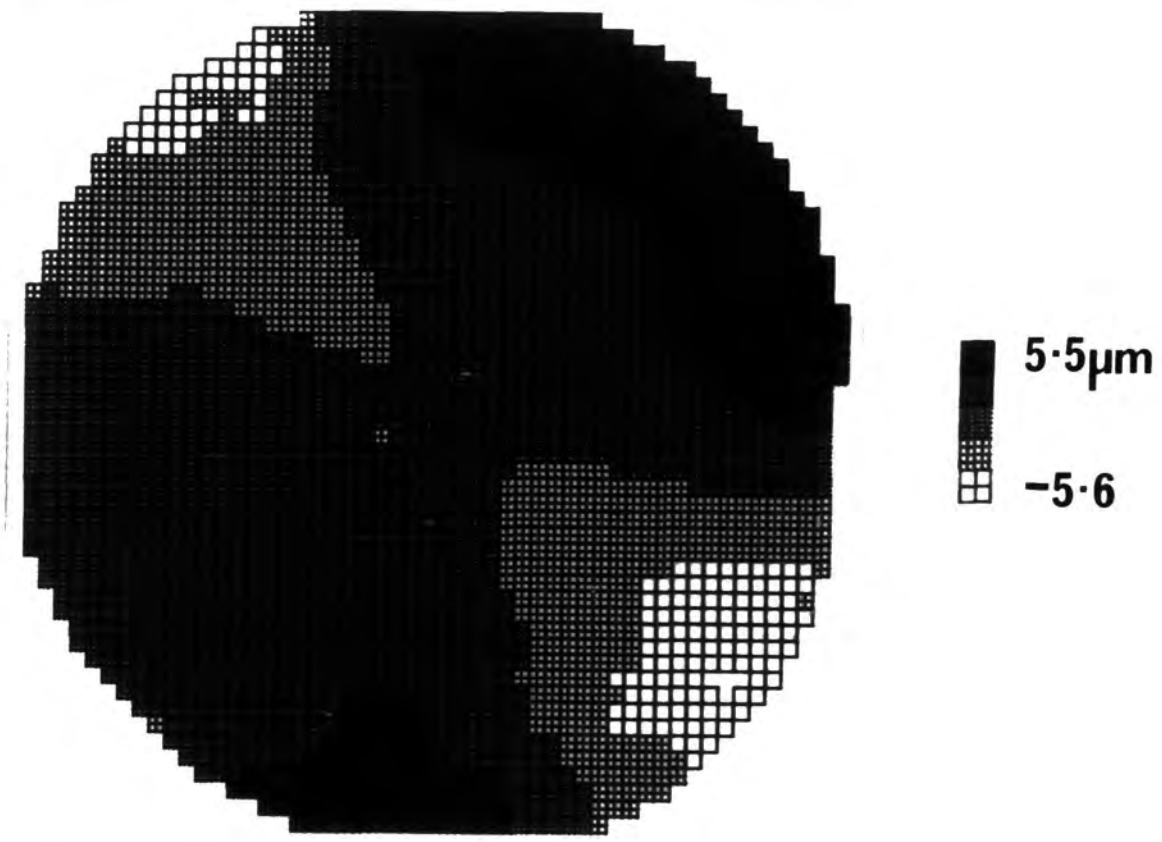

Fig. 3.23d: Sample MMT 76 B2 – relative lattice displacement map

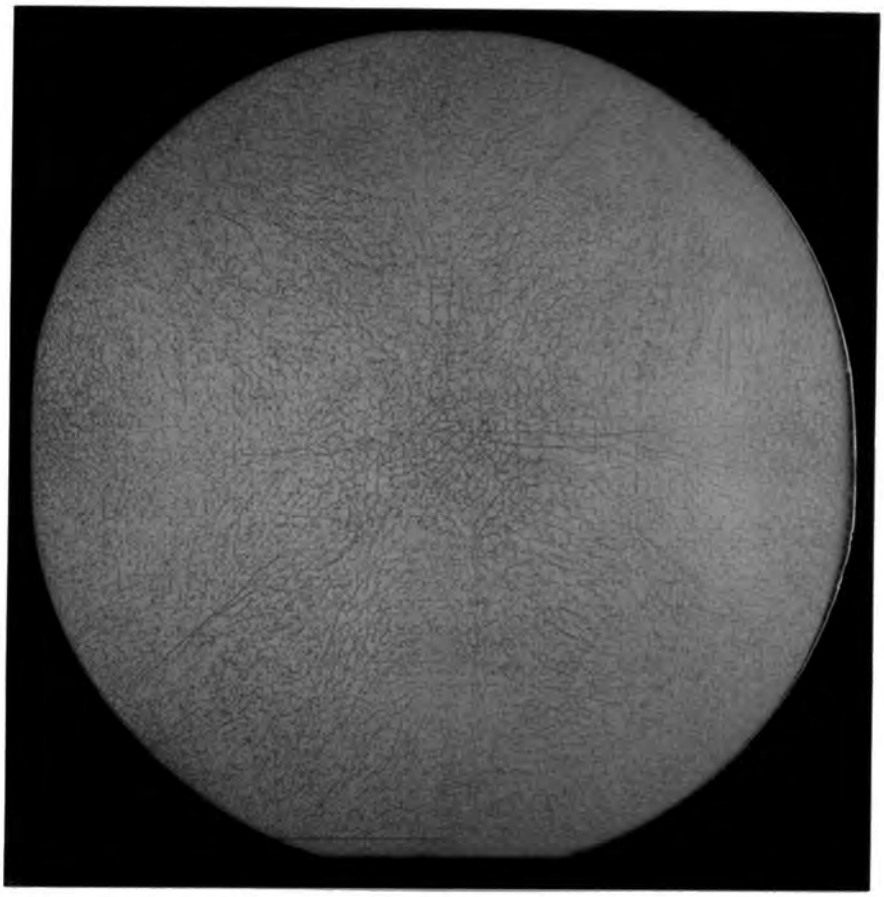

Fig. 3.24a: Sample MMT 65a annealed – KOH etch picture

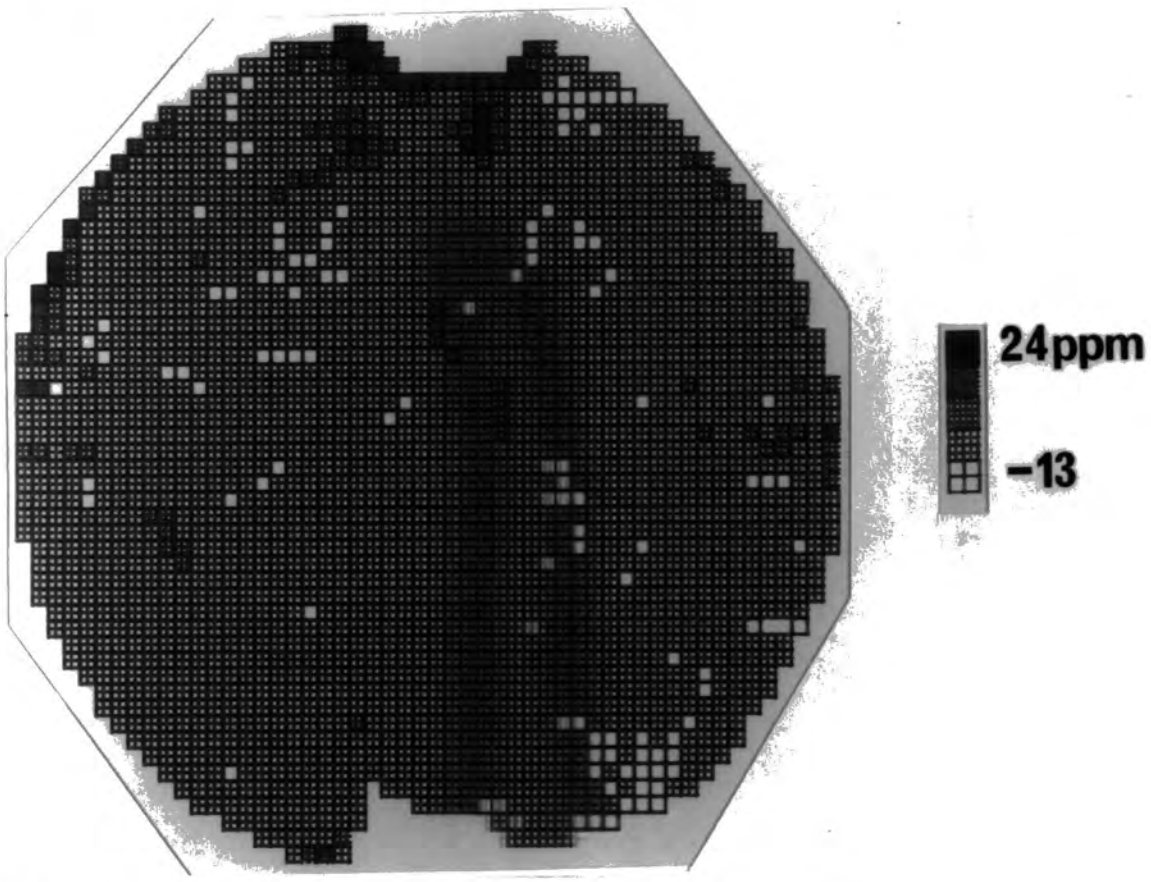

Fig. 3.24b: Sample MMT 65a annealed – relative lattice strain map

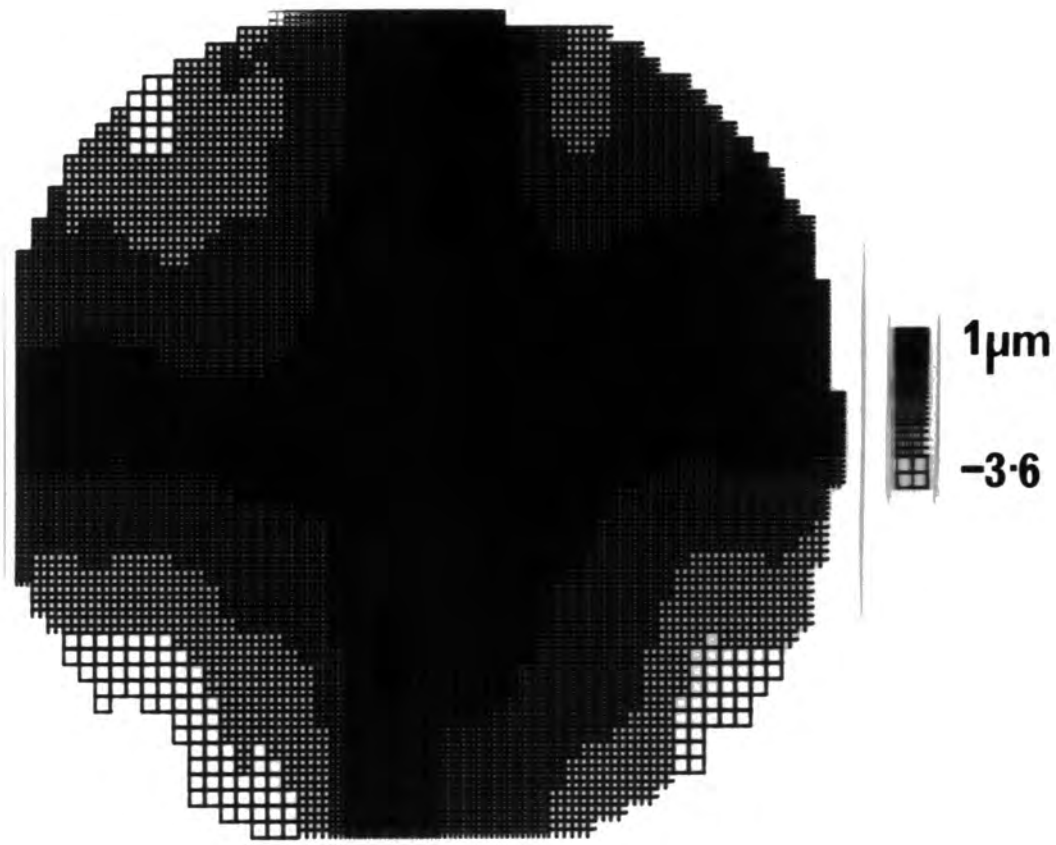

Fig. 3.24c: Sample MMT 65a annealed – relative lattice displacement map

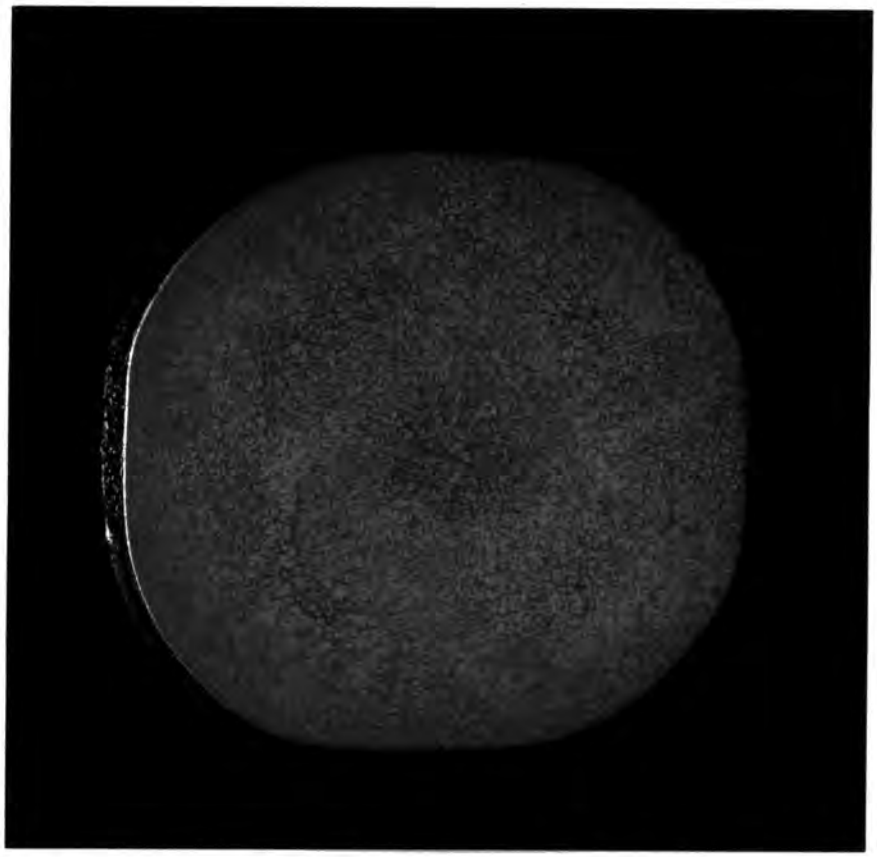

Fig. 3.25a: Sample MMT 65a unannealed – KOH etch picture

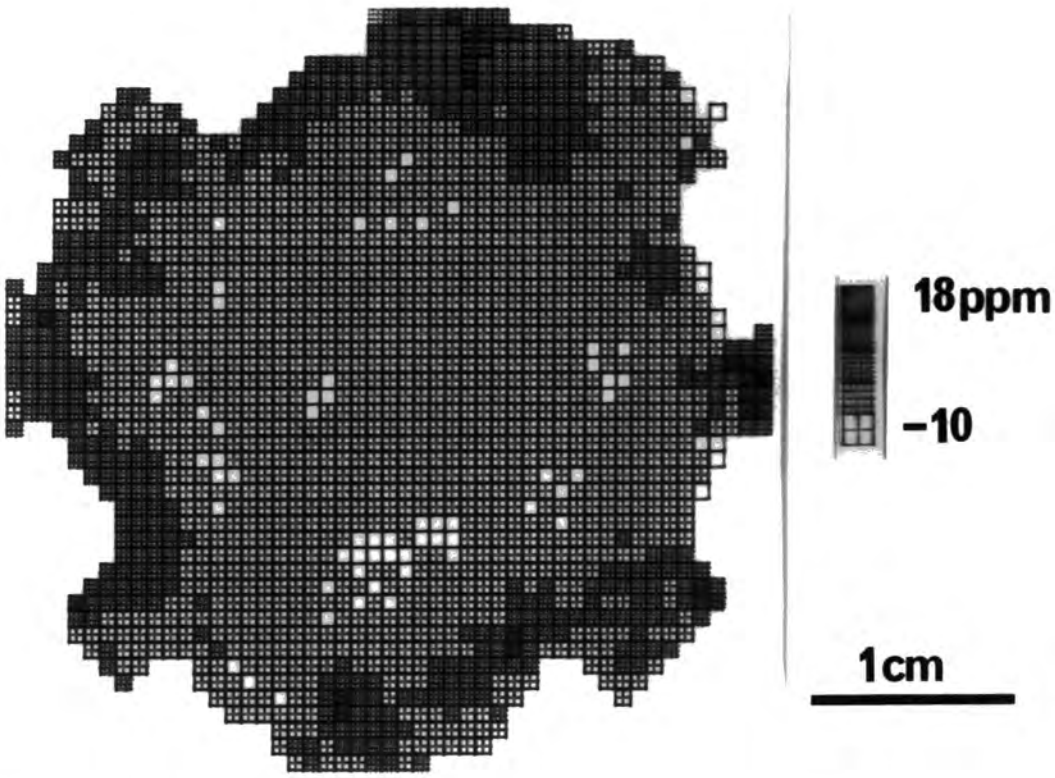

Fig. 3.25b: Sample MMT 65a unannealed – relative lattice strain map

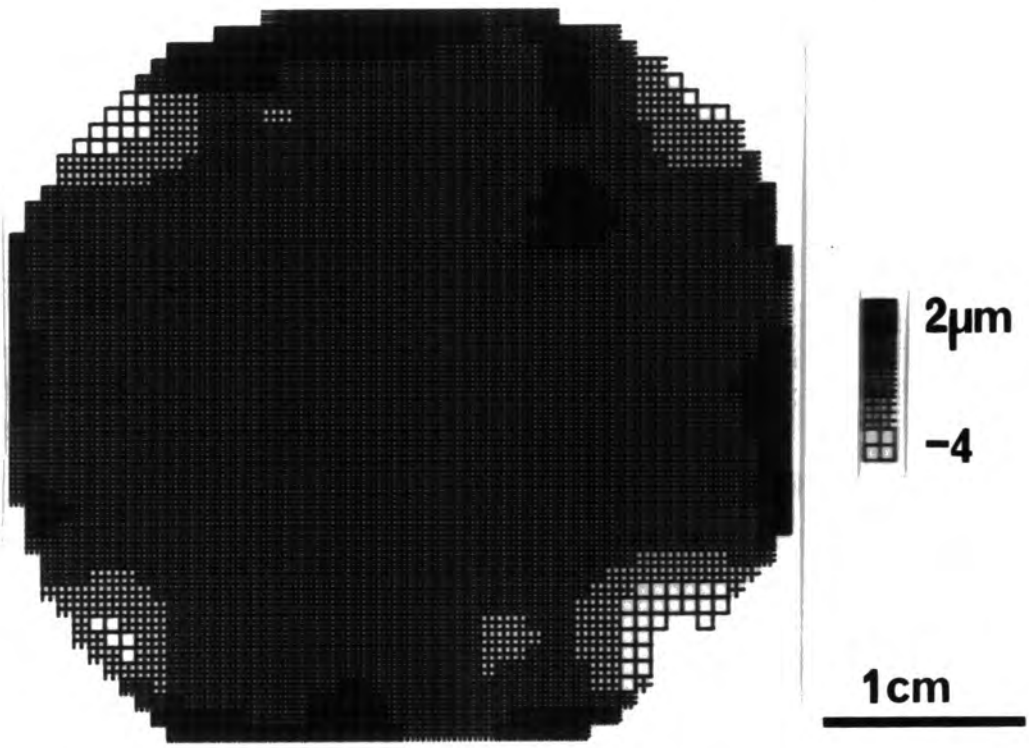

Fig. 3.25c: Sample MMT 65a unannealed – relative lattice displacement map

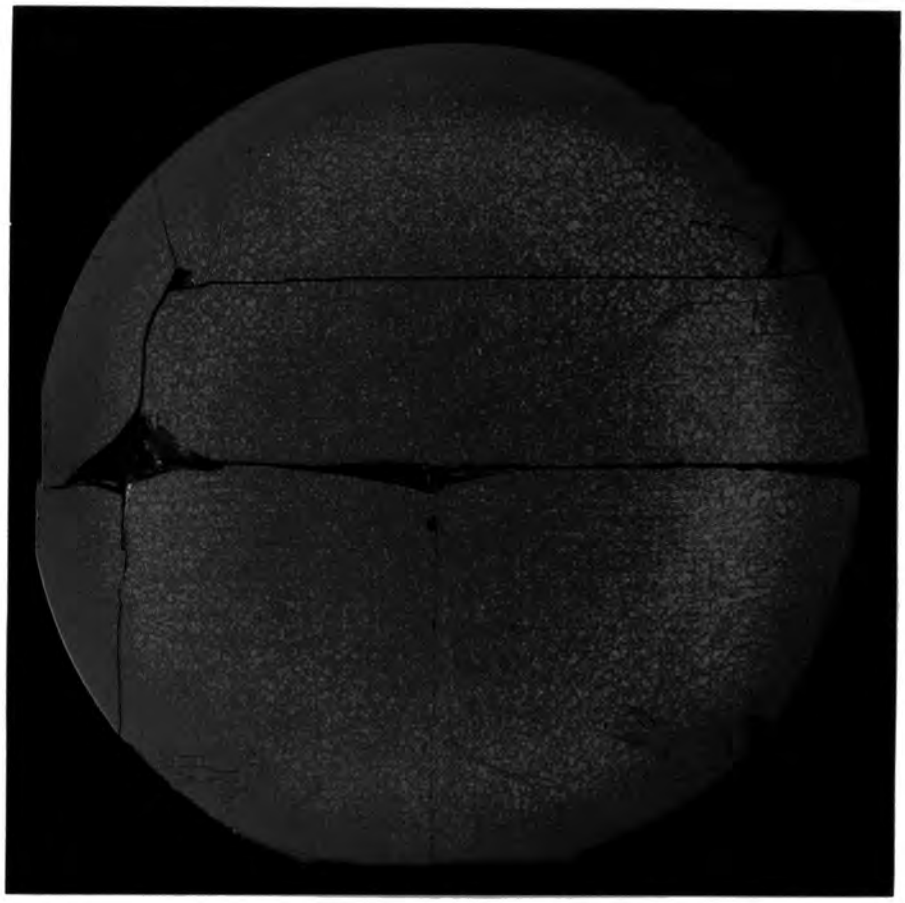

Fig. 3.26a: Sample MMT 65z annealed – KOH etch picture

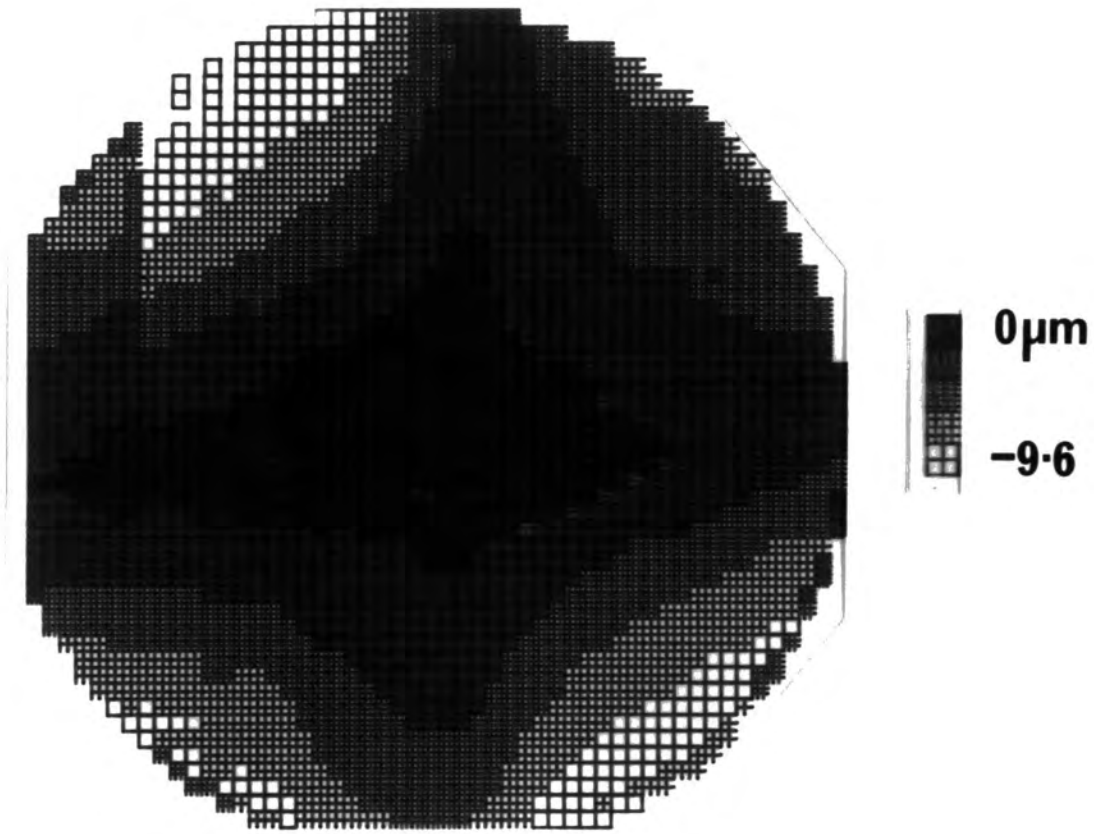

Fig. 3.26b: Sample MMT 65z annealed – relative lattice displacement map

4. STOICHIOMETRY VARIATIONS IN GaAs MEASURED BY X-RAY DIFFRACTION METHODS

4.1 Introduction

4.2 Lang topography using the quasi-forbidden 200 reflection

4.3 Double crystal diffractometry

a) Experimental

b) Results and Discussion

4.4 Summary

4. STOICHIOMETRY VARIATIONS IN GaAs MEASURED BY DIFFRACTION METHODS

Introduction

The lattice strain measurements described in section 3 and those performed by other authors (refs. 36-40, 50) were all undertaken with the aim of revealing variations in stoichiometry or point defect concentration. The results of section 3 and those of Okada (ref. 34) indicate that the strain distribution primarily reflects the strain induced by the dislocation structure, which may or may not reflect the point defect environment. Strain measurements are thus of limited use for studying stoichiometry and should be confined to dislocation-free material. It may be possible, however, to use the integrated intensity of the diffracted radiation as a measure of the stoichiometry since the structure factor will vary as a function of the proportion of constituent atoms. For strong reflections such as the 400 reflection this dependence is weak since the structure factor, ignoring the Debye Waller factor, is given by

$$F_{400} = 4\ (f_{III} + f_V)$$

where f_{III} and f_V are the averaged complex scattering factors for the elements on the group III and V sites respectively. A 1% increase in the As atomic ratio ([As]/[Ga + As]), when using Cu Kα radiation, increases the magnitude of the structure factor by only 0.04%. However, consider a weak reflection which is totally forbidden in an elemental semiconductor with the diamond structure but is permitted in the GaAs zincblende structure due to the difference in scattering factors of Ga and As. Such a reflection is the 200 reflection for which the structure factor is given by

$$F_{200} = 4\ (f_{III} - f_V)$$

where f_{III} and f_V have their former meanings. For this 'quasi-forbidden' reflection a 1% increase in the As atomic ratio increases the magnitude of the structure factor by 24%. Given a detection limit of 0.1% intensity change and assuming kinematical diffraction the minimum change in stoichiometry detectable is $1x10^{-3}$% in the As atomic ratio. (This calculation assumes that an excess of either atomic species is taken up by an increase in the vacancy concentration of the other species.) This is clearly a very sensitive technique but the interpretation of data may be ambiguous since there is some confusion about the relative concentrations of different point defects at a specific stoichiometry. The stoichiometry resolution of the technique may be improved by the use of synchrotron radiation; the wavelength can then be tuned to change the anomalous dispersion corrections in order to reduce further the 200 diffracted intensity and therefore increase the sensitivity to stoichiometry changes.

Fujimoto (refs. 96, 97) has used this technique to study stoichiometry fluctuations in LEC and HB bulk GaAs as well as VPE, LPE and MBE epitaxial layers. He measured the integrated intensity of the 200 reflection on a specially adapted single crystal diffractometer using Mo Kα, radiation (for which the stoichiometry sensitivity is better than Cu Kα) and found intensity distributions across (001) LEC material which followed the 'W' shaped dislocation profile. It is well known that when using the 400 reflection to measure the lattice parameter of LEC GaAs the integrated intensity of the diffracted beam follows the dislocation density (ref. 34). Fujimoto argued that for the weak 200 reflection, since the ratio of the integrated intensity for a mosaic crystal relative to that of a perfect single crystal is 1.01 for Mo Kα radiation, the diffracted intensity should be independent of dislocation density. It is this hypothesis that ensures the intensity variations reflect the stoichiometry rather than the dislocation density and as such should be rigorously tested.

4.2 Lang topography using the 200 quasi-forbidden reflection

In order to test whether or not the 200 reflection is sensitive to the dislocation density in LEC material it is necessary to use topography rather than direct measurements of the diffracted intensity using, for example, a scintillation counter. Direct intensity measurements would require a comparison between dislocation free and dislocated material. Since lattice parameter measurements (refs. 34, 37) may indicate a correlation between the dislocation density and stoichiometry, the source of any differences between the diffracted intensities of the two materials would be ambiguous (either due to the dislocations or stoichiometry differences). The most suitable method is to establish whether or not the dislocation structure present in LEC material is visible on reflection topographs taken using the 200 reflection. To this aim Lang reflection topography was undertaken on a small sample of LEC GaAs approximately $1cm^2$ square and 2.5mm thick. The Lang camera used was a Marconi Avionics system which was mounted on a GEC GX6 rotating anode generator.

Since the 200 reflection is weak, the sample was first set up on the 400 reflection using Cu $K\alpha_1$ radiation. The diffraction conditions were then optimised for this reflection to ensure the correct ratio of the $K\alpha_1$ and $K\alpha_2$ diffracted intensities. A 400 reflection topograph is shown in fig. 4.1a, the dislocation cell structure and a lineage feature being clearly visible. The 400 diffraction setting of the Lang camera was then used as a reference point to find the weak 200 reflection. Once this reflection was detected the generator was set at 15kV and 35mA to ensure that the diffracted beam would not be contaminated with the 400 reflection from 0.771Å wavelength radiation (excitation voltage 16.5kV) present in the white radiation bremsstrahlung. The angular separation and relative intensities of the diffracted beams from the $K\alpha_1$ and $K\alpha_2$ lines were checked to ensure the correct reflection had been found and was properly aligned. (If the generator was adjusted to higher kV the

α_1/α_2 diffracted beam intensity ratio was dramatically reduced indicating the presence of a significant component of the 400 reflection excited from bremsstrahlung radiation at 0.771Å Fig. 4.1b shows a 200/400 topograph taken with the generator set at 35kV and 30mA, although only weak contrast is seen from the lineage feature and cell structure, their presence is clearly visible. A high resolution 200 topograph taken on Ilford L4 25μm nuclear plate with the generator at 15kV and 40mA is shown in fig. 4.1c. The topograph appears completely uniform and even the surface scratches are not seen. It is interesting to note that Fujimoto (ref. 89) had his rotating anode generator set at 60kV and 500mA and thus his diffracted beam would suffer from significant harmonic contamination and be sensitive to the dislocation density in LEC material.

These results suggest that the 200 reflection is insensitive to the dislocation density within the limits of contrast detectable to the human eye. For x-rays over the working range of exposures, the film density is proportional to the energy deposited in the film, E (A R Lang in ref. 60) rather than log E as is the case for visible photons. This proportionality and the contrast detectable by the human eye ($\Delta D/D$ = 0.1-0.2 for a gradual intensity variation) introduce a limit on the 200 reflected intensity resolution of 10% for detection on nuclear emulsion plates. This limit falls short of that required for the detection of stoichiometry variations but it must be remembered that in the sample studied the cell centres were essentially dislocation free, while the cell wall dislocation density is approximately $2x10^5 cm^{-2}$. Typical dislocation density variations on a macroscopic scale over 50mm (001) LEC GaAs are only half an order of magnitude. It is unlikely therefore, given that a dislocation density variation five orders of magnitude causes a variation in diffracted intensity of less than 10%, that the typical macroscopic dislocation density variations of half an order of magnitude will be detectable. However, since the expected 200 intensity distribution across (001) LEC material would be 'W' shaped, following the

dislocation density, it was decided to undertake these experiments on dislocation free material. This would eliminate doubts about dislocation density effects and would reveal whether or not stoichiometry variations exist across (001) slices of GaAs in the absence of dislocation density variations.

Dislocation-free material similar to that studied here had already shown slight variations in 1μm infra-red transmission (ref. 91) which should be accompanied by stoichiometry variations. Studies on the effects of magnetic field on EL2 concentration (ref. 92) have shown a decrease in EL2 with increasing magnetic field. The magnetic field damps down the time-dependent temperature fluctuations in the melt which, in turn, modify the point defect incorporation. Since the time-dependent temperature fluctuations also change as a function growth time, and the growth interface is usually convex, it is likely that point defect environment (and hence stoichiometry) will exhibit small radial variations even in dislocation-free material.

In order to investigate the above hypothesis, Lang topography was carried out on a dislocation free 10mm diameter (001) slice of undoped LEC GaAs grown in a low pressure puller at RSRE, Malvern by D A Hope. The same experimental precautions were taken as in the previous studies to ensure only the 200 reflection was excited. Fig. 4.2 shows a 200 reflection topograph of that slice taken with the generator set at 15kV and 30mA. It is clear from fig. 4.2 that the rather high scattered background intensity is non-uniform across the topographic image. In order to permit removal of this background intensity it was decided to digitise the image. Digital analysis could then be used to create a background image to be subtracted from the total image.

The 200 topograph shown in fig. 4.2 was digitised in 25μm x 25μm square pixels on the Joyce-Loebl flat-bed microdensitometer at the Daresbury laboratory. The digitised image was stored on magnetic tape from which it

could be loaded onto a VAX-780 computer system for analysis. The Advanced Raster Graphics System on the VAX-780 implemented several image processing packages which included contrast enhancement and line scans of intensity across an image. Several other image manipulation programs were also written specifically to analyse the film density distribution on this topograph.

Once loaded into the computer system, the topographic image was expanded in the direction common to the plane of diffraction and the surface of the photographic plate in order to restore the relative dimensions of the original sample. The expansion used a linear interpolation between existing points to determine the density of the extra pixels in the expanded image. The expanded digitised image is shown in fig. 4.3a. Vertically the background intensity distribution is far from uniform but the intensity is essentially constant along the horizontal direction with a small decrease in intensity from left to right (as determined by line scans of the digitised image).

A background image file was created using the vertical background intensity distributions at each end of the topograph. The horizontal intensity profiles above and below the image were used to scale the vertical intensity profile between the known vertical intensity profiles at each end of the image. A background image generated in this way is shown in fig. 4.3b. This image was then subtracted from the total image to reveal a zero background level topograph (fig. 4.3c). Clearly this image is not uniform and a distinct contrast change can be seen along the upper region of the topograph. This is probably caused by the excitation of another, unwanted, reflection which takes flux from the incident beam and is manifested as reduced intensity on the 200 topograph. The gradual reduction in diffracted intensity towards the top left hand edge of the sample may be due to incorrect positioning of the diffracted beam slits, resulting in the blocking of a component of the diffracted beam. The top region of the topograph is clearly unsuitable for stoichiometry measurements.

Horizontal line scans of the lower region are shown in fig. 4.4 and show a reduced diffracted intensity towards the sample edges of approximately 10%. This would correspond to a reduction in the As atomic ratio of 0.33% at the sample edges, an unlikely situation. Previous work on similar samples (ref. 91) had shown a slight increase in EL2 (and hence As) concentration at the sample edge. This contradicts the present results.

Because of the problems described above and the contradiction with previous results (ref. 91), it was felt that Lang topography was not the ideal method of measuring variations in the diffracted intensity for the quasi-forbidden 200 reflection. The use of double crystal diffractometry, however, would ensure that only the 200 reflection was excited and the direct detection of x-rays using a scintillation counter would give improved resolution of the diffracted beam intensity. If implemented on a white radiation source the wavelength could also be tuned to optimise the sensitivity of the diffracted intensity to stoichiometry variations. For these reasons the next experiments were undertaken on the double crystal diffractometer on station 7.5 at the Darebury SRS.

4.3 Double crystal diffractometry

The scattering factor for a particular element may be described by the sum of three terms:

$$f = f_o + f' + if''$$

where f_o is the atomic scattering factor and f' and f'' the real and imaginary parts of the anomalous scattering corrections.

f' and f'' are wavelength dependent and vary considerably, especially close to an absorption edge where there are large negative values of f' and a step function

in f". The approximate profiles of f' and f" for Ga and As are shown in fig. 4.5. It can be seen that at two wavelengths on either side of the As K absorption edge, where $f'_{As} < f'_{Ga}$ the resultant value of F_{200} may be zero and thus the 200 reflected intensity has maximum sensitivity to stoichiometry changes. It is this factor that was exploited in the following study.

a) Experimental

The experiment was carried out on the double crystal diffractometer on station 7.5 of the Daresbury SRS. The same sample was used as in the previous Lang topography study and the system was configured as shown in fig. 4.6. The white radiation beam from the synchrotron source (operating at 2GeV and 115mA) was first monochromated by a double 111 reflection Si beam conditioner and then allowed to pass through a set of $85\mu m^2$ slits followed by an ion chamber to monitor the beam flux. Diffraction from both monochromator and sample were in the vertical plane, ie using the σ polarisation state. The sample was mounted 10mm above the surface of an x-y scanning stage, similar to that described by Halliwell et al (ref. 93) (the extra 10mm height was required to enable the scintillation counter to 'see' the radiation diffracted at the relatively small Bragg angle). Two scintillation counters were employed; one to measure the intensity of the diffracted beam, the other to measure the fluorescence yield from the GaAs sample. Once the monochromator and diffractometer were accurately aligned and set to a wavelength of approximately 1.25Å the wavelength was calibrated relative to the Ga K absorption edge. The monochromator was scanned decreasing the wavelength to that of the Ga K edge (1.195Å) at which point the fluorescence yield from the GaAs sample dramatically increased. The double crystal design of the monochromator is such that the displacement of the diffracted beam is almost independent of wavelength. In the range λ = 1.05Å - 1.25Å the change in the displacement of the diffracted beam is less than 0.3mm. The wavelength calibration exercise

and the experiment can, therefore, be undertaken without the need to adjust the main diffractometor 2θ drive.

Fig. 4.7a shows a double crystal rocking curve taken at 1.2Å, a wavelength slightly greater than the Ga K absorption edge. The rocking curve has a half-width of 6.0 ± 0.1 arc seconds, approximately 4 times the theoretical 200 rocking curve width. The monochromator was then scanned down to a wavelength of 1.16Å and at this point the sample rocking curve split up into a number of peaks (fig. 4.7b). At first it was thought that the detector was faulty but on returning to 1.2Å the original smooth rocking curve was obtained and reducing the wavelength further to 1.148Å also gave a smoother rocking curve (fig. 4.7c).

Tests to discover whether or not the detector or amplifiers were saturating due to an excessive x-ray flux also proved negative, so it was decided to continue the experiment. At a wavelength of 1.16Å the minimum diffracted intensity was obtained so, at this wavelength, rocking curves were recorded as a function of position across a diameter of the sample.

During the acquisition of each rocking curve the incident beam flux was monitored using both the ion chamber and the main storage ring electron current monitor, the outputs of which were relayed to the station control cabin. These measurements were then used to correct the data within each rocking curve to account for the decay of the incident beam and also to normalise the individual rocking curves to the first curve (RC 2007). These rocking curves are shown in fig. 4.8 as a function of position on the sample. Each rocking curve was recorded with an angular step size of 0.1 arc seconds and a counting time of 3 sec. per data point. There are clear differences in the rocking curve as a function of sample position and a significant change in the diffracted intensity (fig.4.9). Each curve in fig. 4.8 spans approximately the same angular

range as the 1.2Å rocking curve (fig. 4.7a) but is split up into a number of individual peaks approximately 0.4 arc seconds wide.

b) Discussion

The rocking curve shape and distribution shown in fig. 4.8 was found to be reproducible and could not be explained as an artifact of the detection system. The observed multi-peaked rocking curves must, therefore, be due to the sample crystal.

If the sample crystal contains regions slightly misorientated with respect to one another, it is possible that the smooth rocking curves at 1.2Å and 1.48Å represent a superposition of curves from the misorientated regions which produce the broader than theoretical rocking curves. If, however, the wavelength is adjusted to 1.16Å, a value at which the 200 structure factor is much reduced the sample rocking curve becomes narrower and it is possible to resolve the individual misorientated regions within the volume of sample probed by the beam. The theoretical 1.2Å, 200 rocking curve width of approximately 2 arc seconds would not resolve these micro-misorientations. The span of the 1.16Å curve can be seen to lie just within that for the 1.2Å curve taken at the same position on the sample (fig. 4.7d) as would be expected if misorientations were present. A double crystal topograph of the sample (ref. 91) does show some structure on a 100-200μm scale which is comparable to the area of the 85μm x 400μm beam size on the sample surface.

The sense of the 200 integrated intensity variation as a function of stoichiometry depends on the sign of the structure factor and for Cu Kα_1 radiation is well defined with increased intensity reflecting an increase in the As composition. For the 1.16Å rocking curves, the sign of the structure factor is unknown and therefore changes in the diffracted intensity cannot be ascribed to specific

changes in stoichiometry. The increase in integrated diffracted intensity towards the sample edges cannot, therefore, be ascribed to a specific stoichiometry change and it is unclear that the observed change is due to stoichiometry variations at all. In order to clarify this situation it would be necessary to measure the anomalous dispersion corrections as a function of wavelength for Ga and As in order to determine the sign of the structure factor. Work should also be undertaken using high order reflections to ensure stoichiometry is responsible for the observed intensity variations and they are not caused by variations in the micro-misorientations across the sample.

Summary

This study has revealed some of the problems associated with quasi-forbidden reflection intensity measurements for determining stoichiometry. The experiments first performed using Lang topography were unsuccessful due to inherent problems in ensuring alignment of the sample and diffracted beam slits. The experiments, however, highlighted the importance of ensuring only the 200 reflection is excited since for the 400 reflection dislocation images are clearly seen on topographs. The data obtained from this study agrees with the lattice parameter measurements (section 3.3a) on 50mm diameter low pressure LEC GaAs. In section 3.3a a lattice parameter decrease of 20ppm was measured towards the sample edges which may correspond to a decrease in the As atomic concentration. The Lang topography results show a decrease in the diffracted intensity towards the sample edges which would also correspond to a decrease in the As atomic concentration. However, not too much weight should be placed on these results since the two samples vary vastly in diameter (50mm and 14mm) and have experienced different growth conditions.

In an attempt to improve the measurement technique double crystal diffractometry was used and wavelength tuning to 1.16Å showed an order of

magnitude decrease in the diffracted intensity compared to that at 1.2Å, which should result in an improvement in stoichiometry resolution. However, the accompanying reduction in rocking curve width at 1.16Å revealed the presence of what are believed to be micro-misorientations of less than 2 arc seconds in the material. A detailed investigation of the above effect has not been undertaken and is beyond the scope of this study. The interpretation of the diffracted intensity data is ambiguous since the sign of the structure factor is unknown for the 1.16Å wavelength used. Before this technique can be used with confidence detailed measurements of the anomalous scattering corrections for Ga and As should be made in the wavelength range from 1.0Å to 1.2Å. With these data it should be possible to choose a wavelength with good stoichiometry sensitivity where the sense of stoichiometry change with respect to diffracted intensity is known. The effects of dislocations on the 200 diffracted intensity could then be fully investigated by making similar intensity measurements at two different wavelengths for which the structure factor has opposite sign. If the changes in diffracted intensity are solely due to stoichiometry variations they would have opposite sign for the two measurements. If, however, intensity variations are linked to the dislocation density then the same intensity distribution would be observed for each set of measurements.

If the above experiment proved the validity of quasi-forbidden intensity measurements for determining stoichiometry then this type of measurement accompanied by electrical measurements, Si implant activation efficiency studies, density and x-ray density measurements should allow insight into the type and concentration of point defects present and their role in determining the electrical properties of GaAs.

Using a synchrotron source and slitting the incident beam down to a 10μm square spot, it may even be possible to probe the point defect environment and stoichiometry variations which are believed to exist around cell wall dislocations in undoped LEC material (ref. 30).

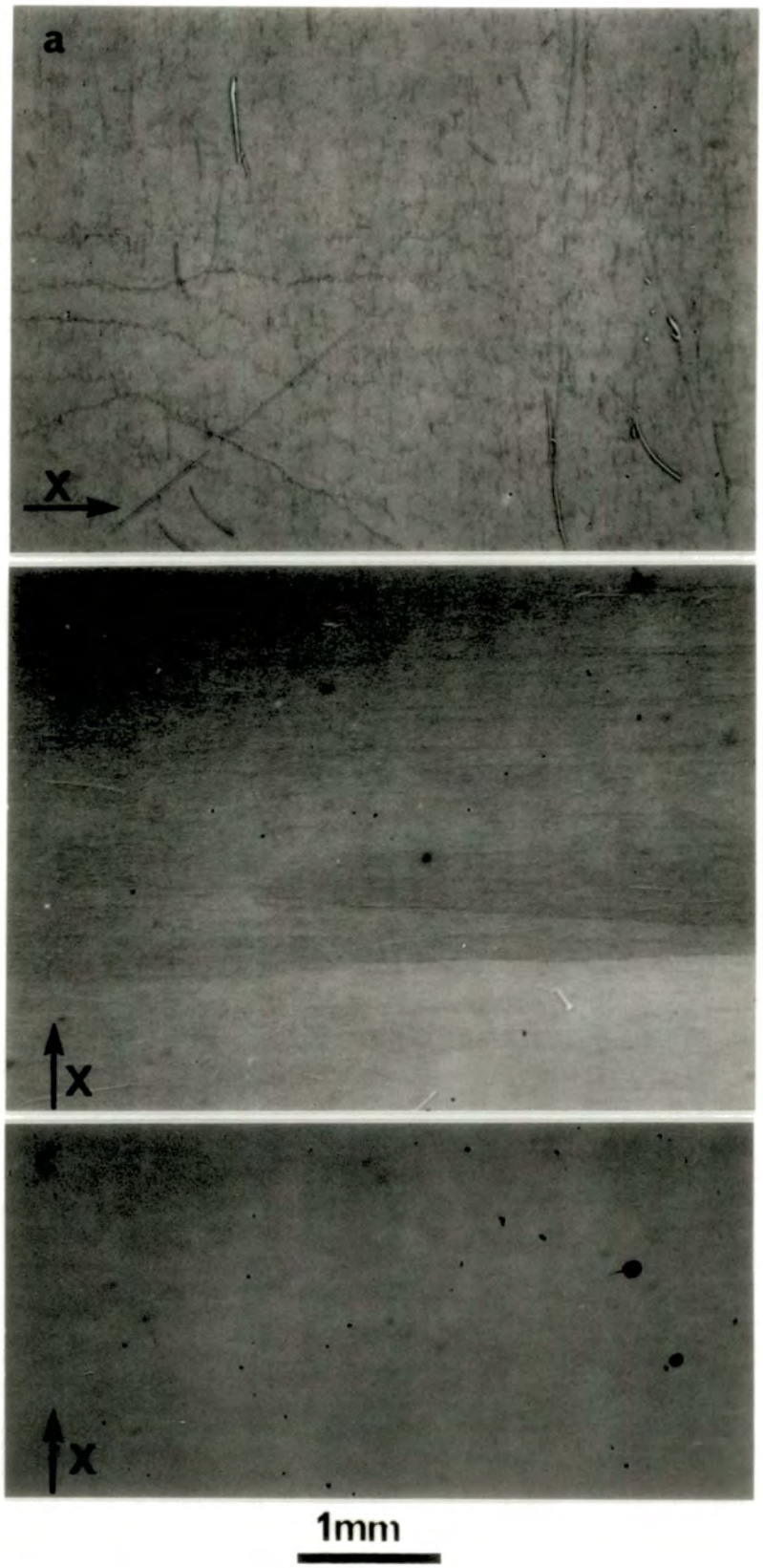

Fig. 4.1: Lang reflection topographs (001) LEC GaAs
a) 400 reflection CuKα_1
b) 200/400 reflections Cu Kα_1/0.771Å generator set at 35KV, 30mA
c) 200 reflection Cu Kα_1 generator set at 15KV, 35mA

Fig. 4.2: Lang 002 reflection topograph of a (001) slice of dislocation-free low pressure LEC GaAs

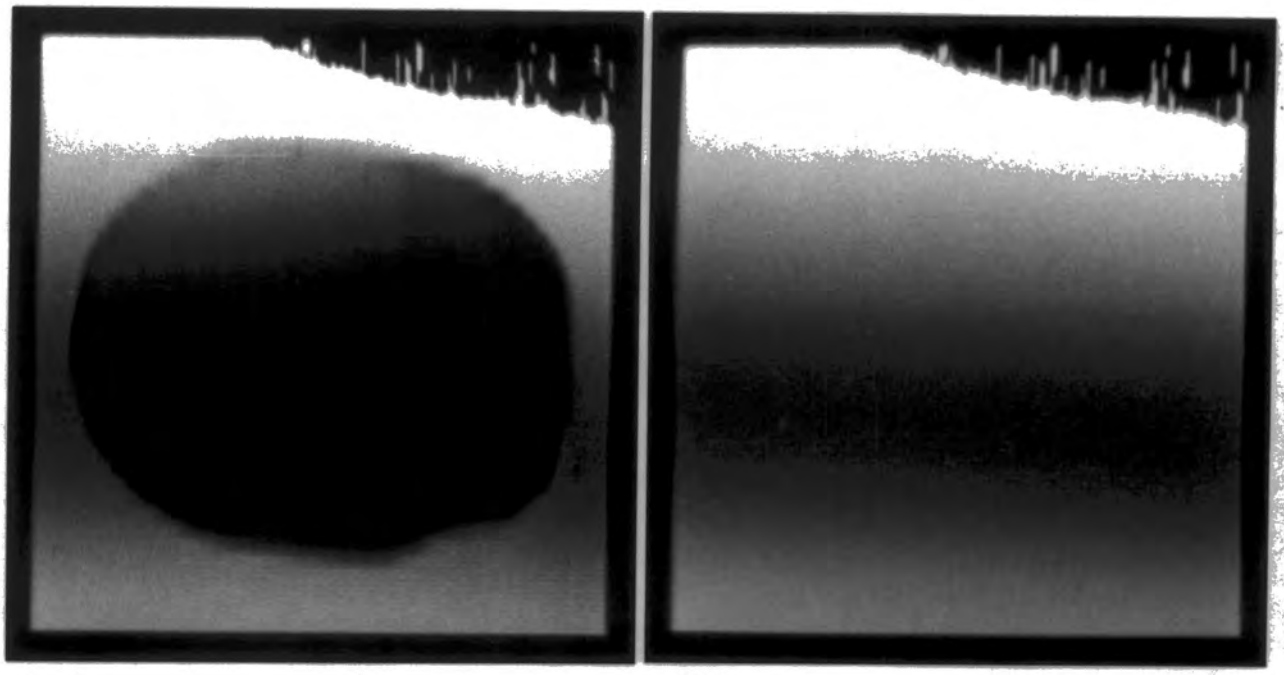

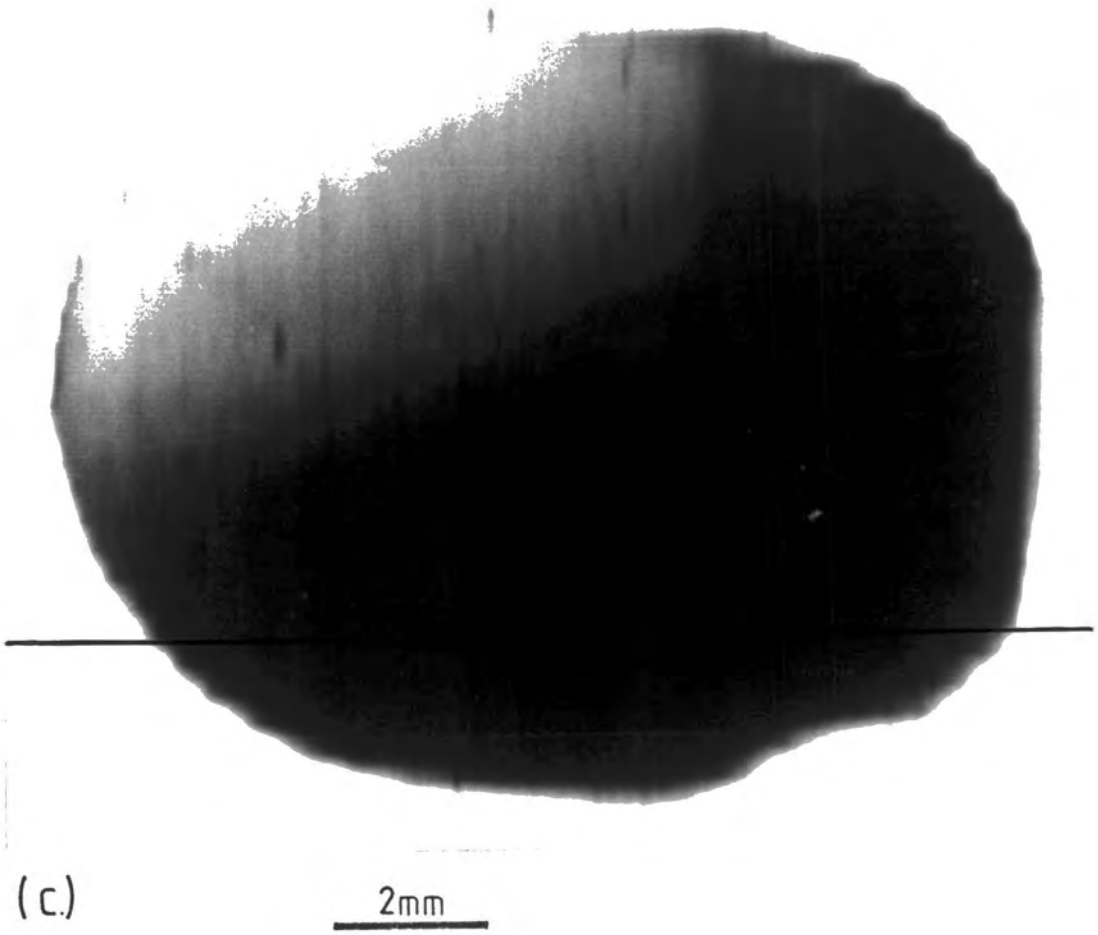

Fig. 4.3: a) Expanded digitised image of the topograph shown in fig. 4.2
b) Background image calculated from a)
c) Total image; a) minus background image b)

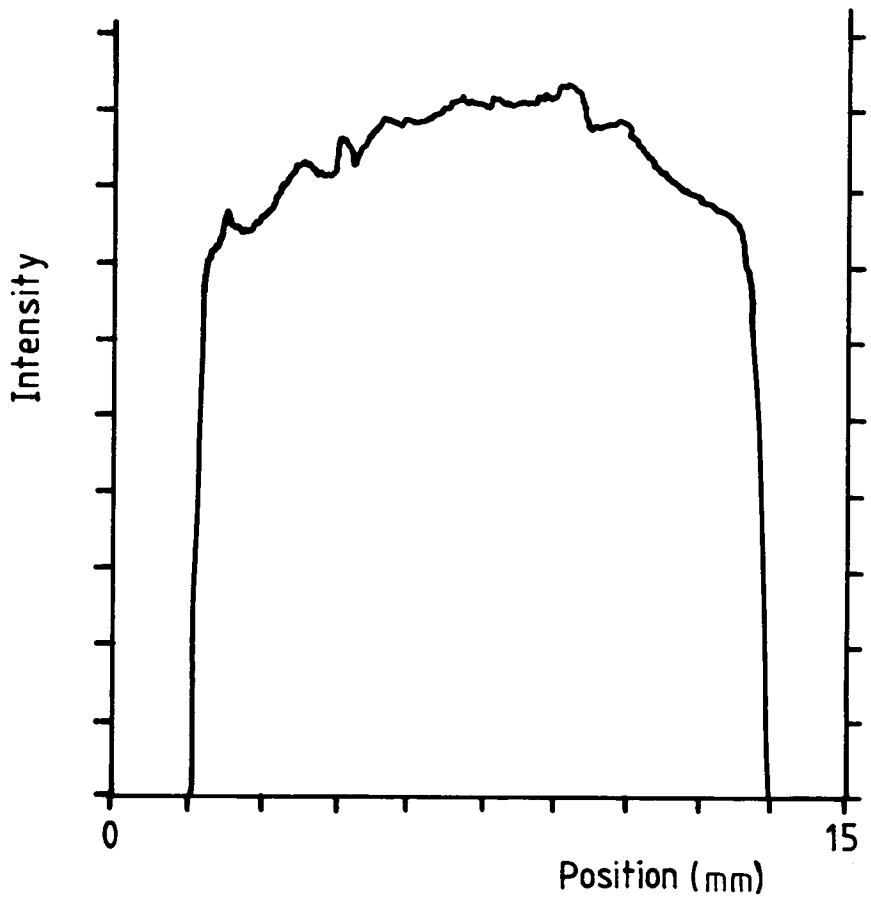

Fig. 4.4: Intensity line scan of the topograph shown in fig. 4.3c

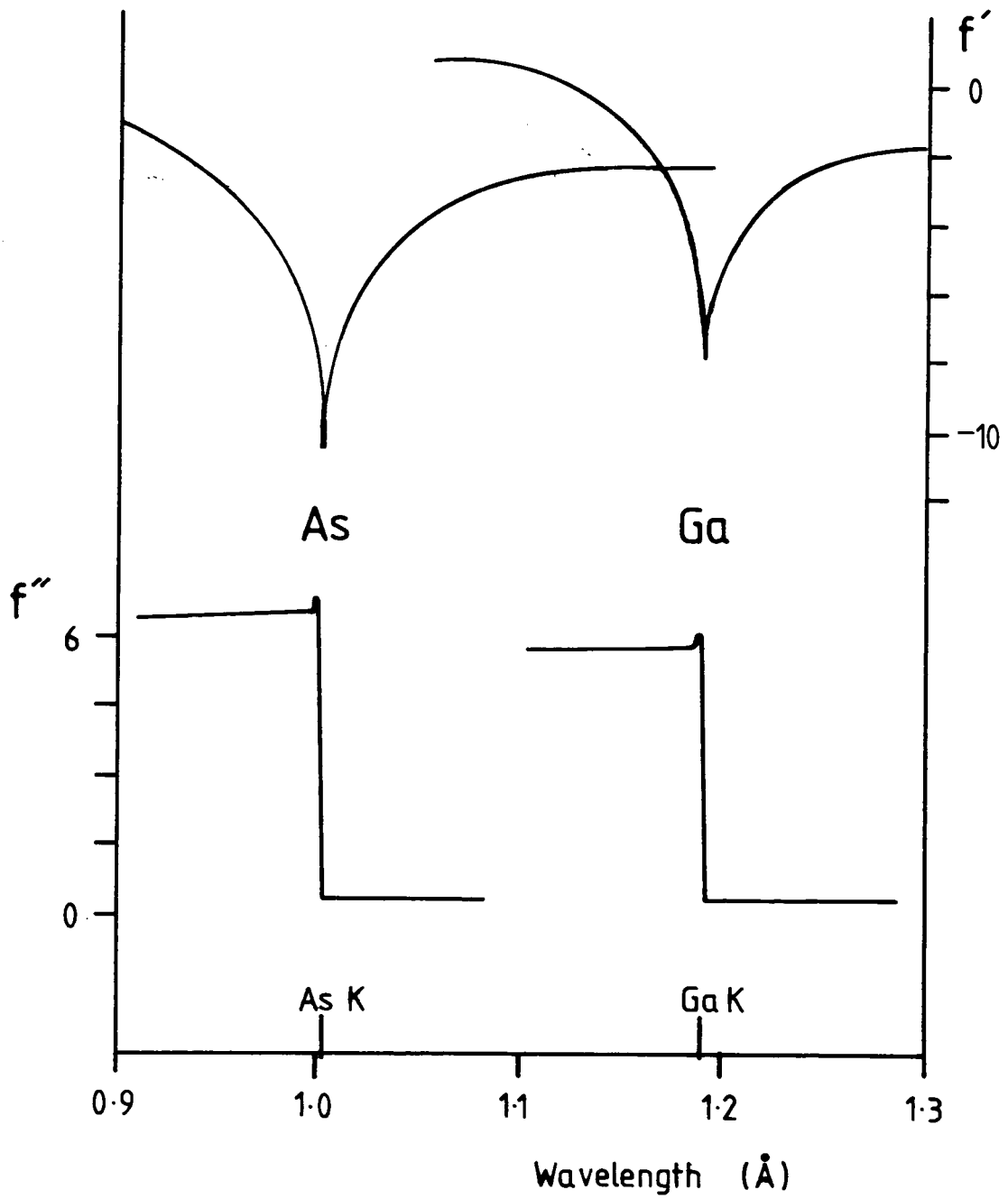

Fig. 4.5: Graph showing the approximate forms of f' and f" for Ga and As in the wavelength range close to the Ga and As K absorption edges

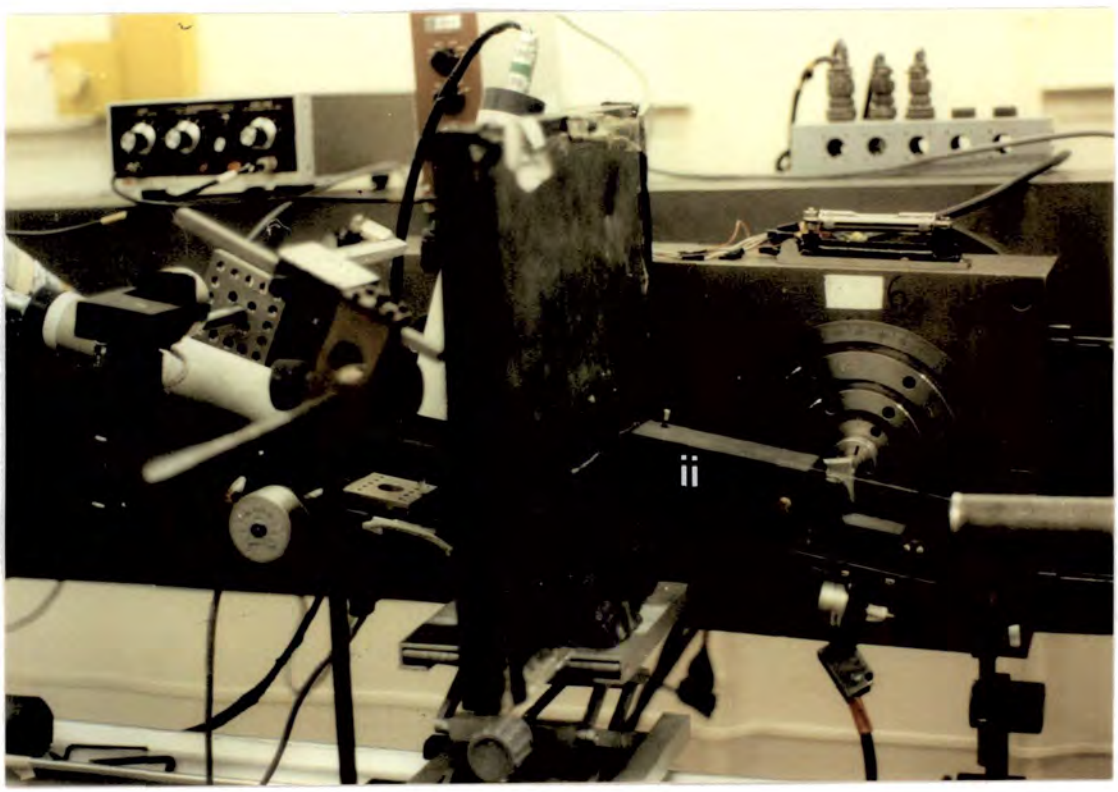

(i) – incident beam pipe
(ii) – double crystal monochromator
(iii) – ion chamber mounted in scatter shield
(iv) – diffracted beam scintillation detector
(v) – GaAs sample fluorescence detector
(vi) – x–y scanning stage → indicates sample

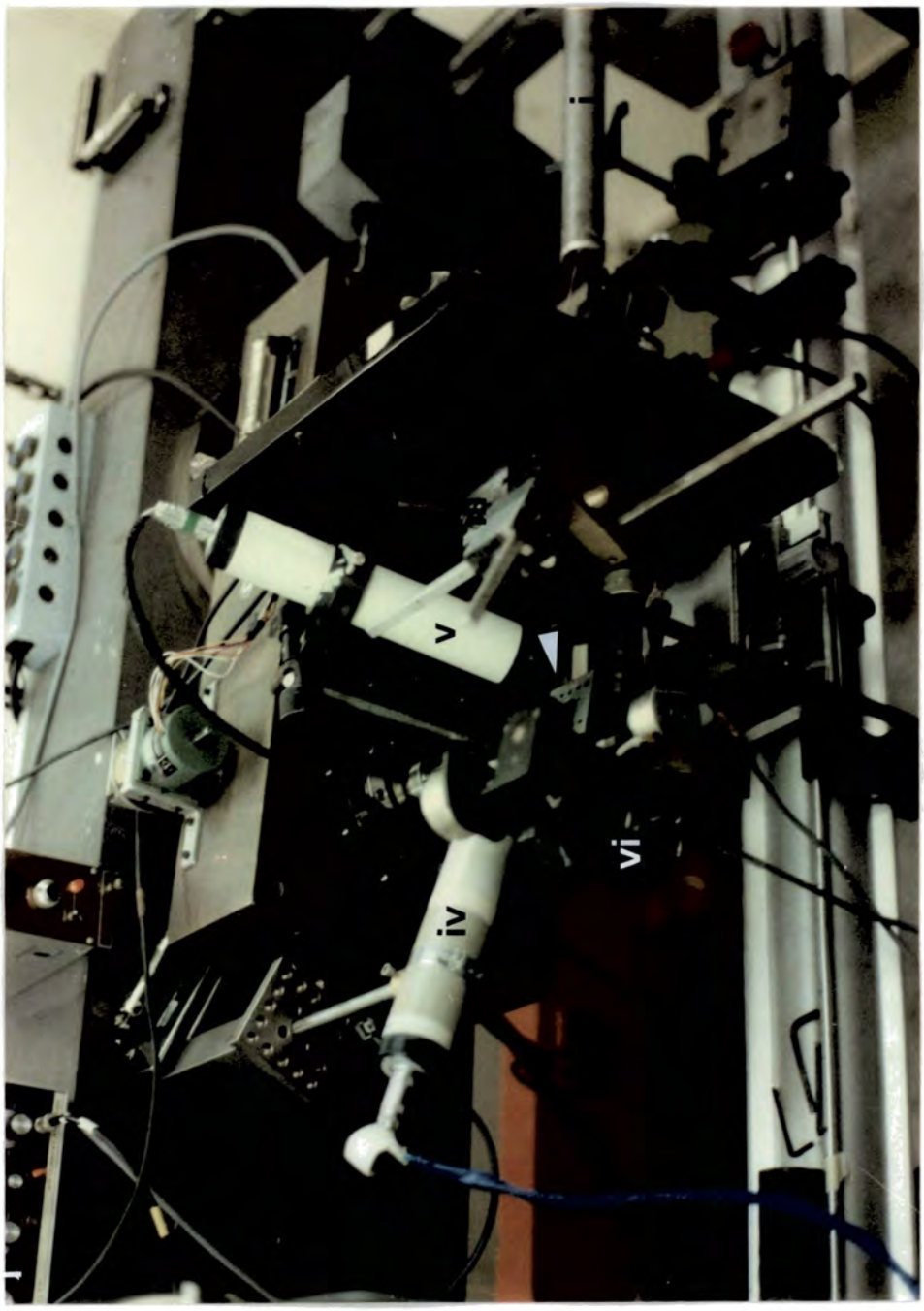

Fig. 4.6: Picture showing the double crystal diffractometer on station 7.5 of the Daresbury synchrotron source as configured for 200 diffraction experiments

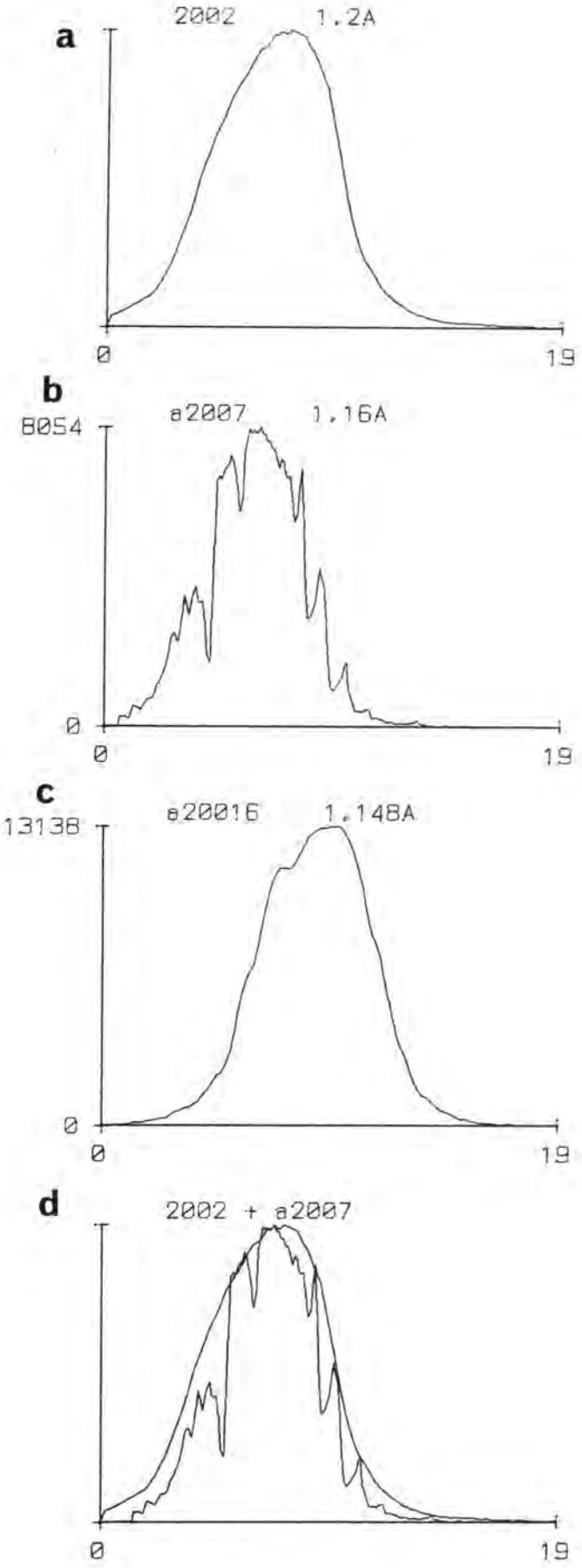

Fig. 4.7: Double crystal rocking curves of the dislocation free (001) GaAs sample using the 200 reflection at a wavelength of: a)1.2Å, b) 1.16Å and c) 1.48Å d) Superposition of curves (a) and (b)

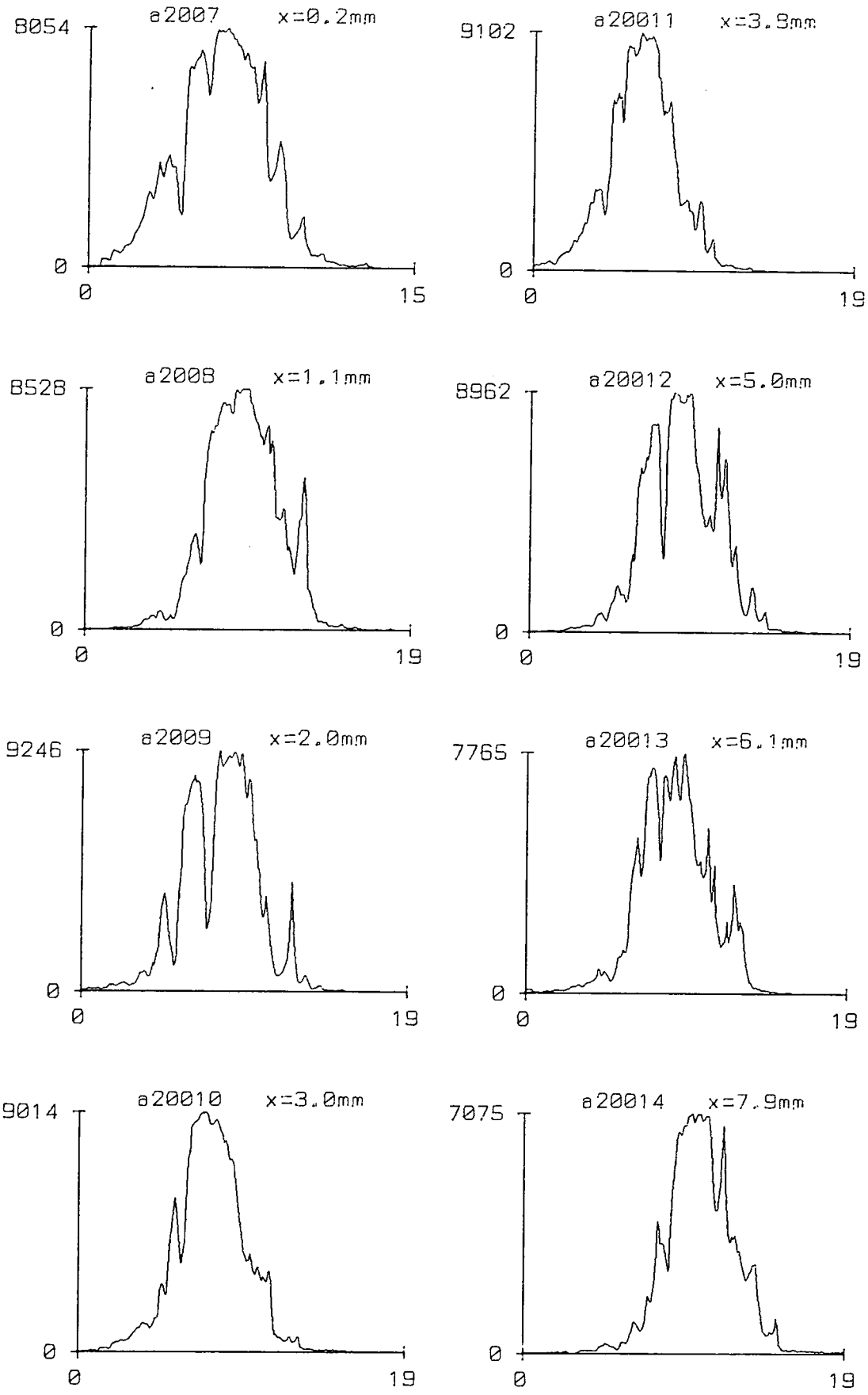

Fig. 4.8: Series of 200 rocking curves of the zero dislocation density (001) GaAs taken at 1.16Å. x indicates the position of the measurements relative to the sample edge

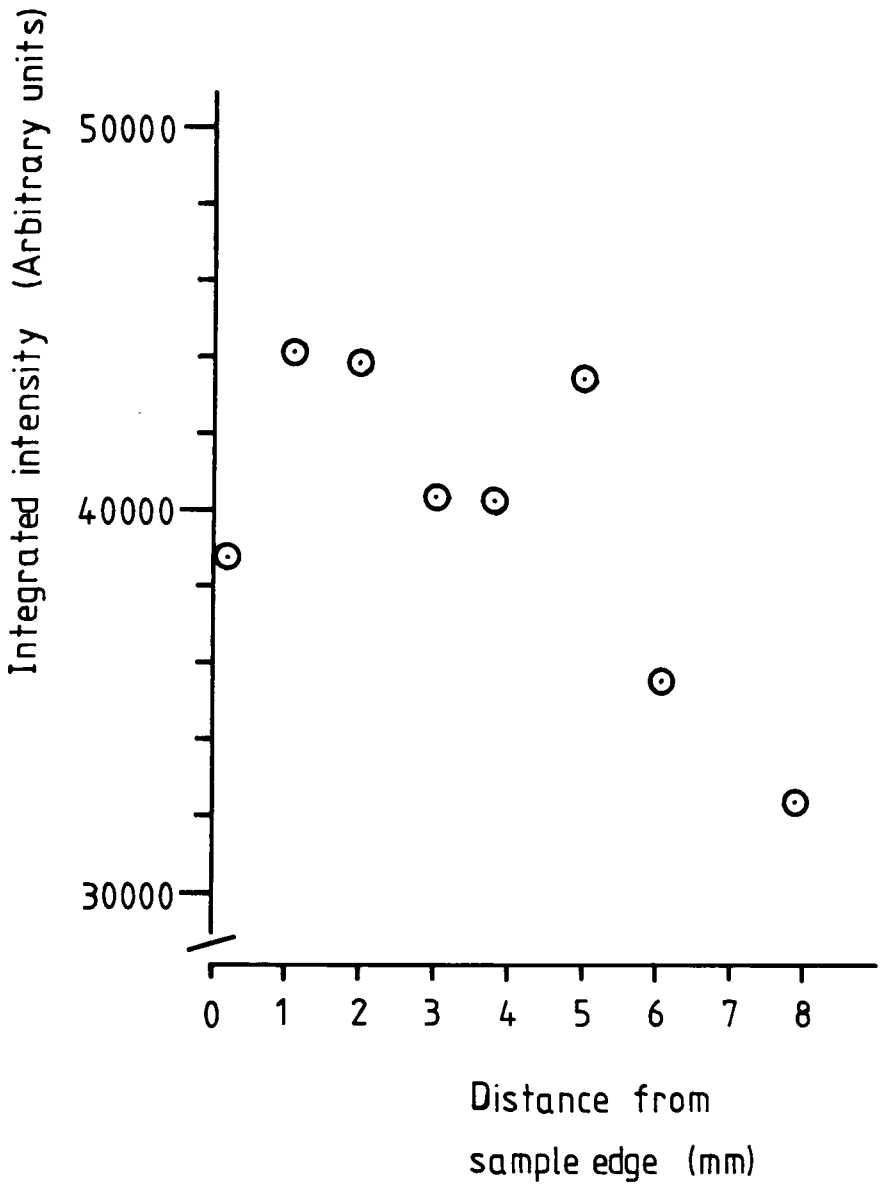

Fig. 4.9: Plot of integrated intensity against position for the rocking curves shown in fig. 4.8

5. DISCLOCATION IMAGE SIMULATION APPLIED TO GaAs

5.1 Introduction

5.2 Image formation mechanisms

5.3 Image simulation by integration of the Takagi-Taupin equations

5.4 Experimental dislocation images in undoped LEC As - general observations

5.5 Image simulation

5. DISLOCATION IMAGE SIMULATION APPLIED TO GaAs

5.1 Introduction

Many papers have been published reporting correlations between the dislocation distribution and various other materials and device parameters in undoped semi-insulating LEC GaAs. Microscopic variations in EL2 concentration (ref. 28) and FET threshold voltage (ref. 15) have both been linked to the dislocation distribution. Etching and CL studies (ref. 30) have both indicated a variation in the point defect environment around cell wall dislocations and TEM studies (ref. 36) reveal the presence of As precipitates on all the dislocations studied. More recently EL2 concentration variations (possibly indicating fluctuations in the point defect environment) have been observed at single isolated dislocations (ref. 94). It has been suggested by a number of authors that this increased EL2 concentration at dislocations arises from an interaction between the dislocation strain field and that surrounding the point defects. If this is the case then the dislocation strain field should be modified which, in turn, may result in a change in the dislocation contrast observed in x-ray topographs. This study aims to compare experimental double crystal topographic dislocation images with theoretical images simulated using dynamical x-ray diffraction theory. This should reveal the effects, if any, of the point defect environment and As precipitates on the dislocation image and hence show any modifications to the strain field surrounding the dislocation.

The dynamical simulation program used here was written by P Riglet and kindly supplied by Y Epelboin from the laboratory of Minerology and Crystallography, University of Paris, France. The program is based on the numerical integration of the Takagi-Taupin equations and is specific to Bragg reflection geometry. A short review of image simulation and the principles involved is presented below; this is followed by the results of the present study.

During the development of x-ray topography as a tool to investigate the perfection and defect structure of crystalline solids several theories have been developed in order to explain the defect images observed. Most of these theories are specific to particular types of defects and particular diffraction geometries, but many retain the physical representation of wave-fields or ray trajectories which is important when trying to understand the diffraction phenomena responsible for image formation. It was not until the formulation of the Takagi-Taupin equations (refs. 95, 96) and the subsequent development of fast computers that it became possible, if difficult and time-consuming, to calculate the images produced from the complex 3-dimensional strain fields which form the structure of many crystal defects. Unfortunately image simulation based on integration of the Takagi-Taupin equations loses the physical representation of wave-fields. However, all the diffraction and absorption phenomena necessary to accurately calculate many defect images are included.

5.2 Image formation mechanisms

A detailed discussion of defect image formation in x-ray topography will not be presented here; refs. 59-61 and 97 should be consulted for further information. Broadly speaking, however, there are two distinct contributions to the formation of defect images in x-ray topography:

a) the reflection of the direct beam as it passes through a highly deformed region (direct images)

b) perturbations in the wave-field propagation within the Bormann triangle (dynamical and intermediary images)

Within category (a) the contrast can be explained using a kinematical model of x-ray diffraction and this contrast usually constitutes the most significant part of

dislocation images in topographs taken under conditions of low to medium absorption (μt <1). The contrast arises from areas where the effective misorientation of crystal planes exceeds the half width of the rocking curve and relies on the direct (transmitted) beam having a larger divergence than the perfect crystal rocking curve width. In these misorientated regions parts of the divergent direct beam not satisfying Bragg's law for the perfect crystal matrix may be diffracted, producing higher diffracted intensity from the deformed region than from the perfect crystal surround. The contrast observed from dislocations under low absorbtion conditions have been explained using this theory (refs. 98, 99).

The images of dislocations produced by effects related to category (b) above can be split into two distinct classes:

i) when the strain gradient is small the concept of a local dispersion surface is maintained and the wave-field is progressively modified as it passes through the strained region. In this region geometric optics can be applied and this situation corresponds to a gradual change of refractive index in an optical analogue. This type of image is generated in the region far from the core of a dislocation where the strain gradient is small. A theory based on these concepts has been devloped by Kato (refs.100, 101) and used to study the qualitative aspects of dislocation images by Dunia et al (ref. 102).

ii) close to the core of dislocations, where the strain gradient is large, it is no longer possible to define a local dispersion surface so the concepts of geometric optics cannot longer be applied. The result is inter-branch scattering and the creation of new wave-fields (intermediary and dynamical images). Only in a limited number of cases where a defect can be completely specified by one simple parameter and in the absence of a complex 3-dimensional anisotropic strain field can interbranch scattering, and the subsequent interference of

wavefields, be described adequately by an analytical solution to the equations governing dynamical diffraction. For example, Authier (ref. 103) applied Kato's theory of diffraction in a slightly deformed crystal and formulated an analytical solution to describe stacking fault contrast. Authier and Patel (ref. 104) have also applied this theory to study the contrast produced by oxygen precipitates in silicon.

These theories provide a good qualitative understanding of defect contrast in many cases but are, in general, unable to accurately predict defect images. For example, Barns et al (ref. 105) observed that the contrast of dislocations in quartz was not obeying the normal extinction criteria. Although simple kinematical theory was sufficient to explain why, it was useless for trying to determine the Burger's vector of the dislocations; the purpose of the exercise. In this situation the only method available is to use theoretical image simulation utilising numerical integration of the Takagi–Taupin equations and look in detail at the dislocation contrast and its dependence on diffraction vector.

The first numerical integration of the Takagi–Taupin equations was undertaken by Taupin (ref. 96) for the case of an incident plane wave impringing on a perfect crystal. The first simulation of an extended defect was carried out by Authier and Balibar in 1967 (ref. 106) for the case of a straight dislocation in an isotropic media. These pilot studies, although useful in marking the start of major advances in the x–ray topographic technique, were limited in their applicability by the accuracy and speed of the computers used. Major advances came with the development of faster and more accurate computers and the development of the integration routines by authors such as Epelboin and Authier.

5.3 The Takagi-Taupin equations

The Takagi-Taupin equations formulated independently by S Takagi and D Taupin relate the amplitudes of the refracted and reflected waves within a crystal solid with an arbitrary specified strain. Takagi, in 1969 (ref. 107) showed that the intensities and integrated intensities with respect to the incident beam angle of the transmitted and diffracted rays at a point on the exit surface are given by integrals over the entrance surface. It is this formulism which allowed the simulation of images in traverse x-ray topography which may be produced from complex anisotropic strain fields such as those surrounding dislocations.

The Takagi-Taupin equations may be written:

$$\frac{\partial D_o(r)}{\partial s_o} = -i\pi K \chi_{\bar{h}} D_h(r)$$

$$\frac{\partial D_h(r)}{\partial s_h} = -i\pi K \chi_h D_o(r) + 2i\pi \left[K\beta_h - \frac{\partial [h.u(r)]}{\partial s_h} \right] D_h(r)$$

where χ_h and $\chi_{\bar{h}}$ are Fourier components of the electric susceptibility, u(r) is the local deformation of the crystal at point r and h is the reciprocal vector of the reflection. $D_o(r)$ and $D_h(r)$ are the amplitudes of the refracted and reflected waves respectively and s_o and s_h are unit vectors in the direction of the refracted and reflected rays respectively.

$$\beta_h = (|k_h| - |k_o|)/|K|$$

where K is the wave vector of the incident wave and k_o and k_h wave vectors of the refracted and reflected waves respectively. The value of β_h is chosen to

simplify the relations of continuity between the vacuum and the entrance surface and to match the extremities of the vectors k_h amd k_o.

Two different methods have been developed for the numerical integration of the Takagi–Taupin equations. Taupin's method (ref. 108) and that developed by Authier et al (ref. 109). The Taupin method uses an extension into two dimensions of the one–dimensional Runge–Kutta third order method and is ultimately more accurate than the algorithm developed by Authier et al. However, for a given precision, the formulism used by Authier et al based on the half–step derivation, is faster than Taupin's (ref. 110). Since it is Authier's method which is most often used in numerical calculation, the theoretical approach is described below.

Following the approach outlined by Epelboin (ref. 111), the equations may be integrated along a network whose axes are defined by the diffracted and refracted beam directions (fig. 5.1). If the elementary steps of integration are along the s_o and s_h directions and are defined as p and q respectively then:

$$p = \gamma_o \text{ ELEM}$$

$$q = \gamma_h \text{ ELEM}$$

where ELEM is the thickness of a slab of material parallel to the crystal surface and $\gamma_o = \cos(n.s_o)$ and $\gamma_h = \cos(n.s_h)$ where n is the unit vector in the direction of the surface normal.

If we introduce the variables:

$$A = -\tfrac{1}{2}ip\pi k\ \chi_h$$

$$B = -\tfrac{1}{2}iq\pi k\ \chi_h$$

$$W = i\pi q \left\{ K\beta_h - \frac{\partial[h.u(r)]}{\partial s_h} \right\}$$

where only W is a function of position inside the crystal; then using the so–called 'half–step derivative' the Takagi–Taupin equations may be written:

$$\begin{bmatrix} D_o(s_o,s_h) \\ D_h(s_o,s_h) \end{bmatrix} = {}^1/d \begin{bmatrix} C_2AC_2 & AB & AC_1 \\ B & AB & B & C_1 \end{bmatrix} \times \begin{bmatrix} D_o(S_o-p,S_h) \\ D_h(S_o-p,s_h) \\ D_o(S_o,S_h-q) \\ D_h(S_o,S_h-q) \end{bmatrix}$$

Where $d = 1 - W - AB$, $C_1 = 1 + W$ and $C_2 = 1 - W$

Thus, referring to fig. 5.1, if D_o and D_h are known at positions B and C then D_o and D_h can be calculated at position A. The thickness of the slab ELEM must be small enough so that D_o and D_h vary slowly over this distance. This is particularly true for regions of the crystal close to the edge of the Bormann fan or in a very distorted region where D_o and D_h may vary rapidly.

This formulation of the Takagi-Taupin equations permits their numerical integration relative to the boundary conditions which must be defined for the diffraction geometry used. Details of the specific boundary conditions for different diffraction geometries are presented in detail by Epelboin (refs. 111, 112).

The theoretical approach to the simulation of defect images is specific to the experimental technique employed. A section topograph (incident spherical wave) may be simulated to a good approximation by 'lighting' one point on the entrance surface and setting the deviation parameter β equal to zero. An extended plane wave may be successfully simulated by lighting a number of points on the entrance surface and taking into account their relative phases. Transverse topographs (extended spherical wave) present particular problems; they may be simulated by adding the results from a series of point sources as is the case in the experimental situation. However, because of the rapidly varying values of D_h and D_o where the defect intersects s_o (where the direct image is formed) and in regions close to the edge of the Borrmann fan, it is necessary to chose a small integration step. This increases the integration time and also introduces computational errors due to the large number of integration steps,

Epelboin (refs. 113–115) solved this problem by introducing a 'varying step algorithm' which chooses the step size to fit in with the large fluctuations of D_h and D_o at the edges of the Borrmann fan and in areas where the defect strain gradient is large. Thus it is now possible to simulate accurately defect images for spherical wave diffraction both in section and traverse topographs and for plane wave topographs.

Numerical integration of the Takagi–Taupin equations as described above has been successfully used to simulate the contrast due to dislocations (refs. 113–116), stacking faults (ref. 117) and concentration striations (ref. 118) all in the transmission geometry. Epelboin et al have made a study of the effects of crystal anisotropy on dislocation contrast (ref. 119) and defined the limits above which anisotropy must be included in strain field calculations. They found that anisotropy considerations were more significant for dislocation contrast in diffraction geometries where $g.b = 0$. In the Bragg reflection geometry Bedynska has studied the contrast of screw dislocations lying perpendicular to the sample surface (ref. 120) and Gronkowski (ref. 121) has studied the contrast of edge dislocations inclined at small angles to the crystal surface. Bedynska observed good agreement between simulated and experimental images, Gronkowski emphasised the importance of considering surface relaxation effects when the dislocation lies close to the surface (even with these effects included in the simulation the agreement between theory and experiment is not good in the region where the dislocation line emerges at the surface. Riglet et al (refs. 122, 123) have studied misfit dislocations in a GaAlAsP/GaAs epilayer structure under plane wave reflection diffraction. They observed good agreement between experimental and theoretical images for dislocation in the layer and substrate. This latter observation has a bearing on this study since it proves the ability of the theory to accurately predict dislocation contrast in GaAs. The misfit dislocations studied by Riglet et al have not undergone the same high temperature treatment as the intrinsic dislocations in bulk material and would

therefore not be expected to lie within the same point defect environment. Any significant discrepancies between experimental and simulated data in the present study should therefore reflect modification of the dislocation strain field caused by the point defect environment or As precipitates.

The program used in this study was a constant step algorithm which is adequate for simulating plane wave topographs where the direct image component should be small. The program allows arbitrary reflection geometry and permits any orientation of the dislocation line. However, surface relaxation effects are only included if the dislocation line lies parallel to the sample surface. The formula determined by Stroh (ref. 124) and Tucker (ref. 125) are used to calculate the dislocation strain field. The program was run on a VAX-780 computer and images were displayed on a sigma graphics terminal using the Advanced Raster Graphics System. The densitometric response of the L4 nuclear emulsion plate was included in the image representation using a program written by M Pantos at Daresbury Laboratory and hard copies were obtained via a Polaroid hard copy unit. Care was always taken to ensure that the integration step size conformed with that required for the diffraction conditions employed (refs. 112, 123).

5.4 Experimental dislocation images in undoped LEC GaAs - general observations

The overall dislocation distribution and its relation to the lattice distortions in (001) LEC GaAs has been discussed in Section 3. Here the dislocation image contrast is discussed. Detailed analysis is difficult because of the high dislocation density which gives rise to image overlap. However, general comments can be made.

For certain diffraction conditions, in all the (001) material studied the cell wall

contrast extends approximately 50μm wider than that which can be ascribed to the dislocations themselves. This mainly occurs for diffraction conditions on the low theta side of the Bragg reflection. Fig. 5.2 shows two sets of double crystal topographs of the central region of a 75mm (001) slice. The two topographs on the left were taken using the 224 reflection while for the two on the right the sample was rotated by 180° about the surface normal and the 224 reflection was used (the right hand topographs appear slightly blurred due to the lower resolution structurix D7 film used to record these topographs). The top two topographs show an area on the high theta side of the Bragg reflection and those at the bottom an area on the low theta side. It can be seen that for both diffraction vectors the 'extended' cell wall contrast is light (decreased intensity) for the topographs taken on the low theta side of the Bragg reflection. In the two topographs on the high theta side this contrast is reversed but is less pronounced than that on the low theta side. This effect indicates a reduction in the Bragg angle around the cell walls. (A lattice tilt would cause a reversal in the contrast for the 180° sample rotation.) The contrast change is more pronounced on the low theta side of the reflection due to the asymmetry of the rocking curve profile; the steeper slope on the low theta side results in a higher strain sensitivity. Estimating the change in Bragg angle observed to be less than 1 arc second the upper limit on the lattice strain is $4x10^{-6}$. This finding is consistent with 1μm infrared transmission microscopy where an increased EL2 concentration is observed at cell walls (ref. 28). This would be accompanied by an increase in the As atomic ratio which is thought to cause a lattice expansion. A more detailed study of the dislocation contrast in (001) slices is impossible due to the high dislocation densities. A (111) cut slice from the seed end of an ingot was chosen for a comparison of the experimental and theoretical dislocation images.

5.5 Image simulation

The aim of this study was to examine the general dislocation contrast and make a comparison with the simulated images, rather than to produce a detailed study and comparison of the dislocation contrast. Fig. 5.3 shows a 440 reflection double crystal topograph taken of a (111) cut slice from the seed end of a (001) undoped LEC ingot. The topograph was taken using radiation of 1.5A wavelength from a Si monochromator (440 reflection from a {110} surface) on the synchrotron radiation source. In certain areas individual dislocations can clearly be distinguished and are well separated from other images. The long uniform images are from dislocations lying almost parallel to the sample surface and in the two {111} slip planes intersecting the surface at an angle of 120° to one another (ie the (1$\bar{1}$1) and ($\bar{1}$11) slip planes). By analysing topographs taken using the three $\{440\}$ type Bragg reflections and employing the usual contrast extinction rules it was possible to identify the Burgers vectors of the two sets of dislocations (types (a) and (b) as shown in fig. 5.3). Type (a) were found to be predominantly $\frac{1}{2}a[10\bar{1}]$ and type (b) predominantly $\frac{1}{2}a[01\bar{1}]$. In order to determine the deviation, as a function of position on the crystal, from the top of the Bragg reflection profile a Bragg angle map was produced in the same manner as described in section 3. This Bragg angle data was used as part of input data for the simulation program.

The experimental dislocation images range from 9μm to 16μm in width and follow the usual contrast changes as a function of the diffraction conditions relative to the Bragg peak (ie. opposite black/white contrast on the two flanks of the rocking curve and narrow white images on the peak of the rocking curve). The width of the images is in agreement with the results of Petroff et al (ref. 123) for misfit dislocations in (001) material. The narrow image width of these dislocations excludes any quantitative analysis of the experimental data using the Joyce-Loebl flat bed micro-densitometer, the minimum slit size of

which is 5μm x 10μm.

Figs. 5.4 to 5.7 show a series of simulated and experimental images, the experimental images being taken from the topograph shown in fig. 5.5. The critical data for the simulation of each image is shown in table 5.1 along with a comparison of the experimental and simulated image widths. There is a general agreement between the experimental and simulated data except for fig. 5.4 where the simulated image is approximately 20% broader than the experimental image. The depth (used in the simulation) of the dislocation below the sample surface was chosen by an analysis of the image contrast. Simulated images as a function of depth in the range from 1μm to 4μm showed little change in image width. Those outside this range had quite different contrast, particularly close to the surface where fringes were seen as an extension of the normal black/white contrast.

Further, more quantitative analysis of the image contrast is impractical with the equipment available. However, the above results do indicate a general agreement between experiment and theory, suggesting that As precipitates and an enhanced EL2 concentration around the dislocations do not significantly modify the dislocation strain field. This suggests that there is not a strong strain interaction between the EL2 centre and the dislocation strain field and adds to suggestions that the interaction may be electrostatically driven.

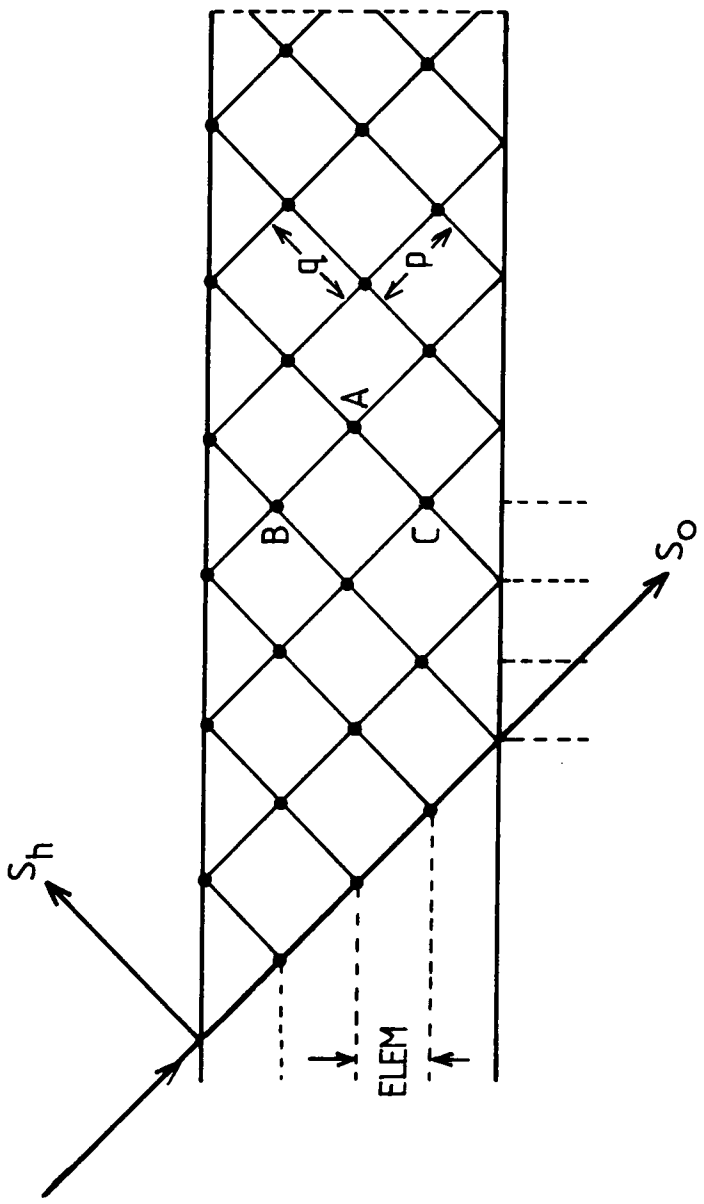

Fig. 5.1 Diagram showing the network used for the integration of the Takagi–Taupin equations

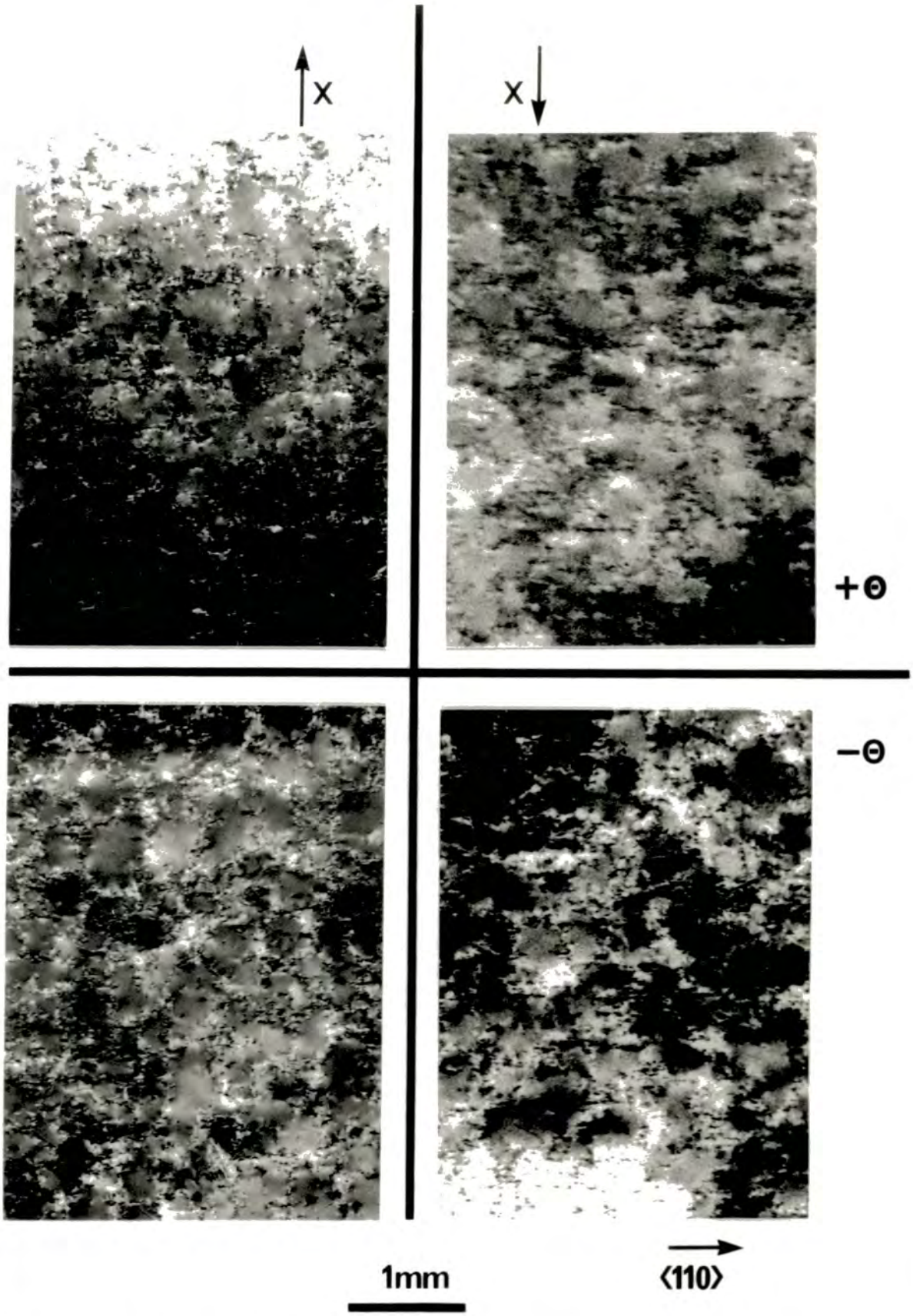

Fig. 5.2 422 double crystal reflection topographs using the 224 reflection (left) and the $22\bar{4}$ reflection (right). The topographs were taken at 1.5A on the synchrotron source using the 511 reflection from a {511} cut Si monochromator. The figures on the right-hand side indicate the position on the sample rocking curve of each topograph.

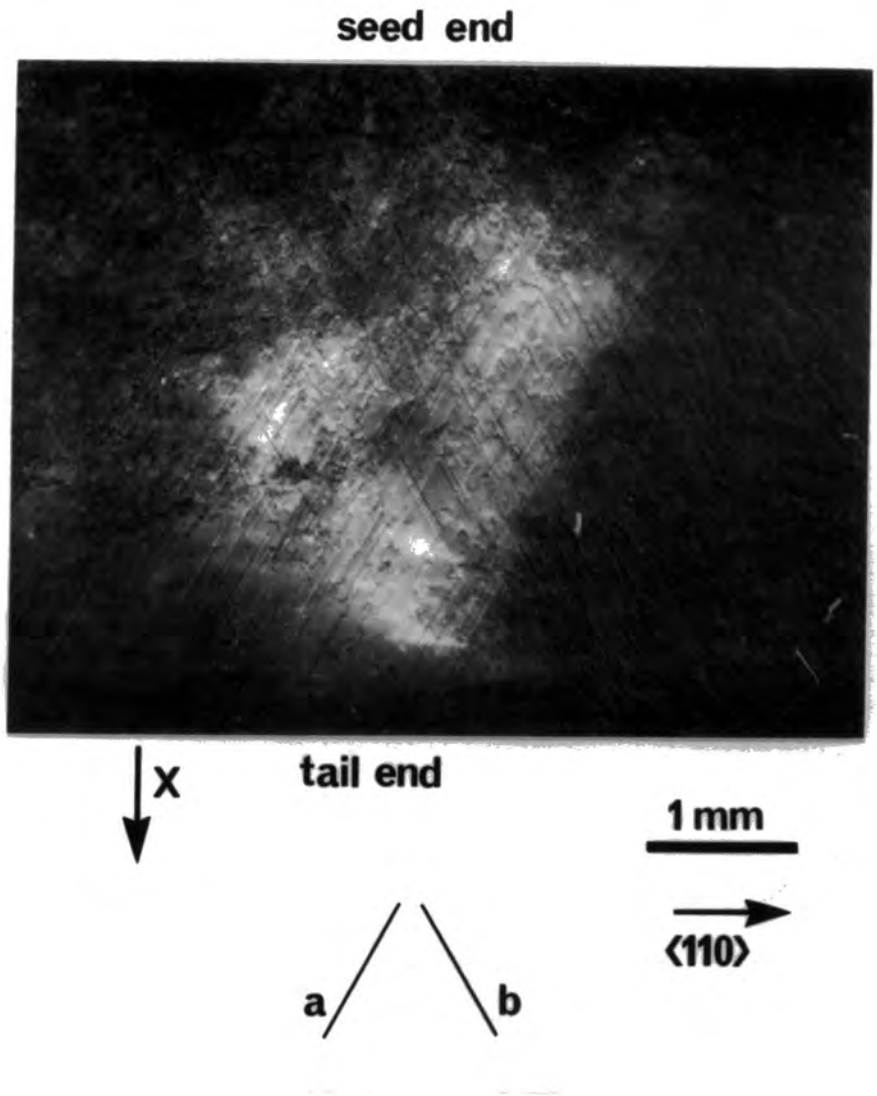

Fig. 5.3 440 double crystal reflection topograph of a {111} slice from the top end of an undoped LEC GaAs ingot. Taken at 1.5A on the synchrotron source using the 440 reflection from a {440} cut Si monochromator

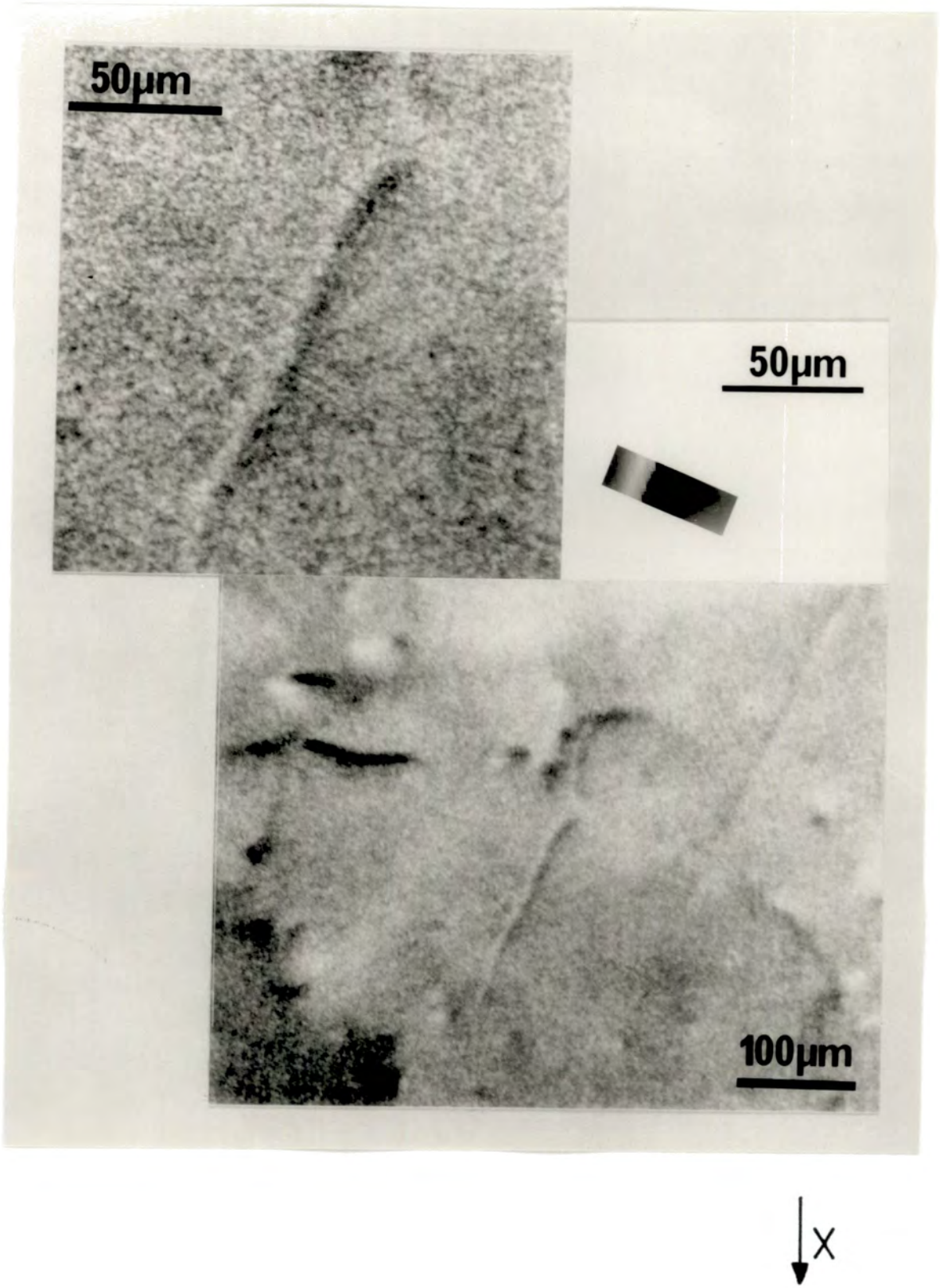

Fig. 5.4 Experimental and simulated dislocation images – dislocation data shown in table 5.1

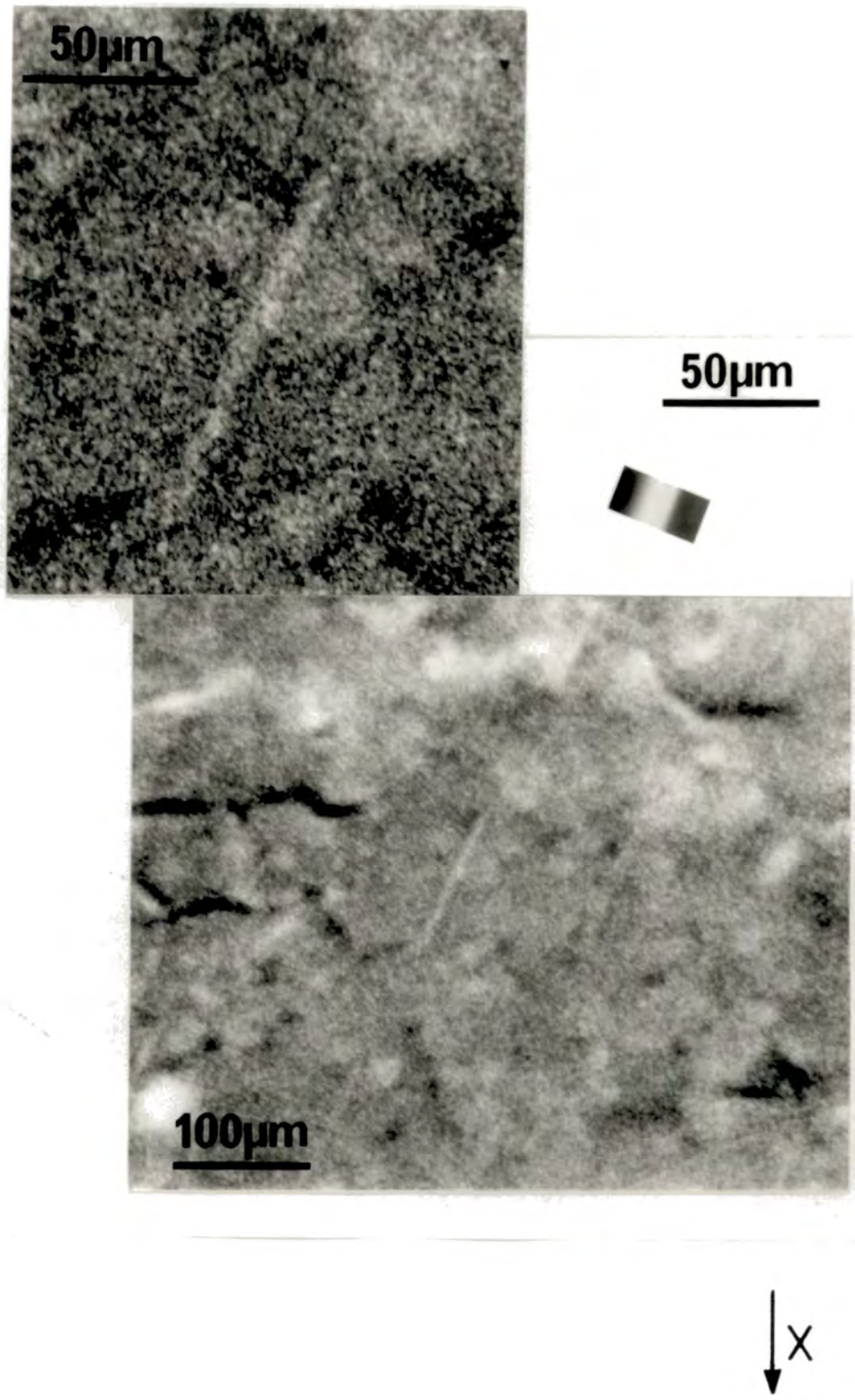

Fig. 5.5 Experimental and simulated dislocation images – dislocation data shown in table 5.1

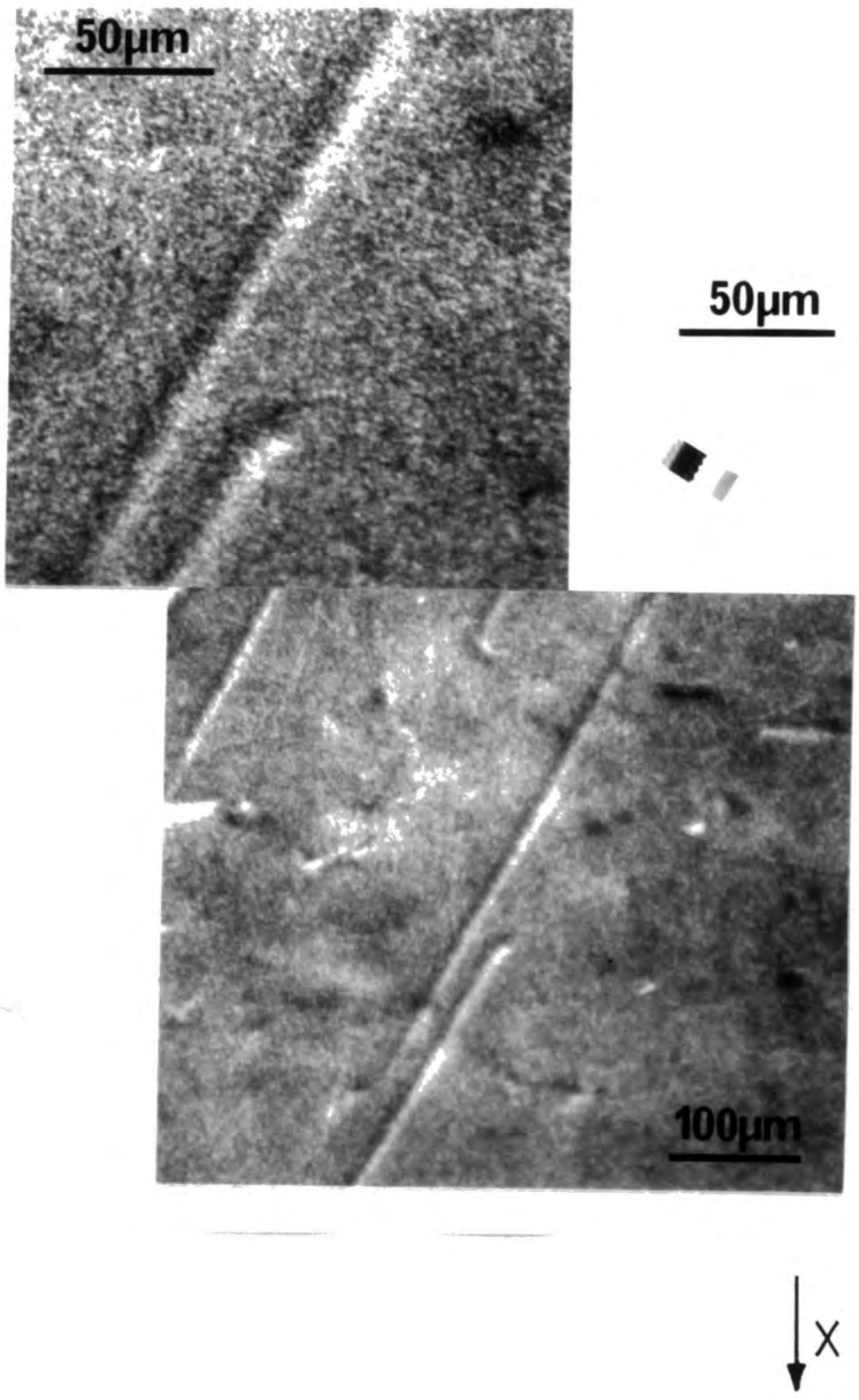

Fig. 5.6 Experimental and simulated dislocation images – dislocation data shown in table 5.1

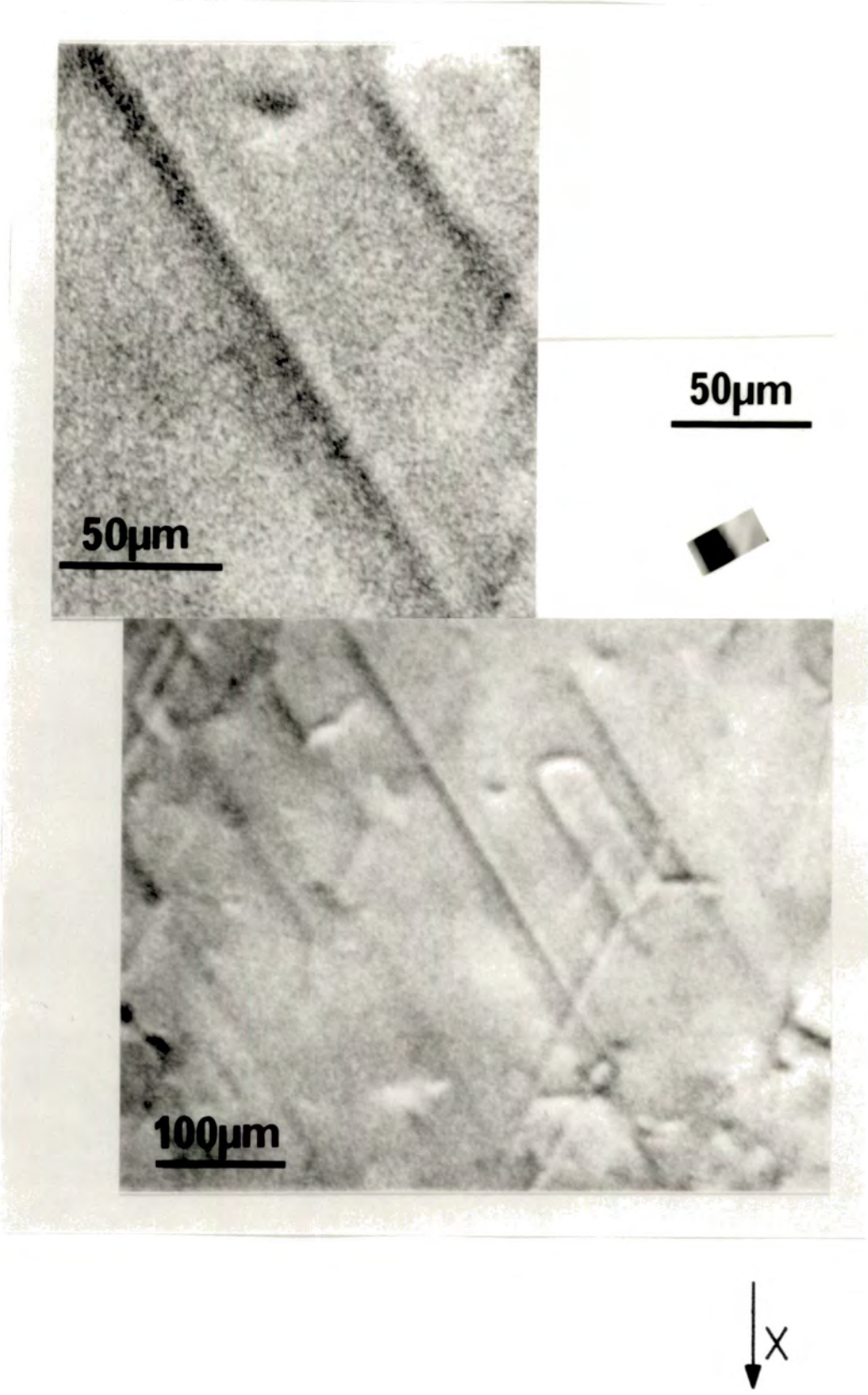

Fig. 5.7 Experimental and simulated dislocation images – dislocation data shown in table 5.1

TABLE 5.1

Simulation →	Fig.5.4	Fig.5.5	Fig.5.6	Fig.5.7
Dislocation Type	a	a	a	b
Burgers Vector	$\frac{1}{2}a[10\bar{1}]$	$\frac{1}{2}a[10\bar{1}]$	$\frac{1}{2}a[\bar{1}01]$	$\frac{1}{2}a[01\bar{1}]$
Depth (μm)	3	3	2	3
Deviation from Bragg peak (arc seconds)	−5	0	−5	−5
Simulated image width (μm)	19	9.5	13.5	14
Experimental image width (μm)	16	9	14	15

6. SUMMARY

This study has demonstrated the suitability of double crystal topography for the analysis of long and short range lattice distortions in 50mm diameter samples of semi-insulating GaAs. The properties of the x-ray source necessary for these measurements have been specified and the principal requirement of low beam divergence is fulfilled by a synchrotron source. This combination of synchrotron source and double crystal topography has enabled mapping of relative lattice strain and tilt over large sample areas with precisions of 2ppm and 1 arc second respectively. However, the low beam divergence of the source does introduce more stringent requirements on monochromator perfection, particularly if the above precisions are to be achieved and it has been shown that monochromator non-uniformities that would not be detectable when using a standard sealed tube source are significant on an SRS.

Initial double crystal x-ray topography studies of undoped material revealed lattice tilts of 20-40 arc seconds which were associated with dislocations arranged in linear arrays (lineage) and smaller tilts of less than 2 arc seconds associated with dislocations arranged in cell walls. A comparison of the topography data with 1μm infrared micrographs has shown that all areas of increased dislocation density (cell walls, lineage and slip bands) are associated with an increase in the neutral EL2 concentration. This latter finding suggests that the increase of EL2 at dislocations is not a consequence of EL2 formation by dislocation climb and is probably due to a strain or electrostatic interaction between the EL2 centre and dislocations. This does not, however, exclude dislocation climb as a formation mechansim responsible for the macroscopic EL2 distribution.

Lattice strain measurements on a series of 50mm diameter undoped samples revealed positive strains of 20-30ppm towards the periphery of samples, where the dislocation density is highest. The same diametric strain distribution was observed in both annealed and unannealed samples and indicates that EL2 (and

hence point defect environment) is not the primary cause of lattice strain since EL2 is known to redistribute uniformly on annealing. It is more likely that the strain is related to the dislocation distribution with increased dislocation density corresponding to a positive strain.

(001) lattice tilt measurements were made by analysis of data taken for 90° rotations of the sample about the surface normal. This was necessary since topographic techniques are only sensitive to the component of lattice tilts lying in the plane of diffraction. These measurements revealed a four-fold symmetry in the (001) lattice tilts and showed that the lineage features play a major role in determining this symmetry although the symmetry still exists in the absence of lineage features. For seed end samples a four-fold symmetry was invariably found about the <110> and <100> directions in the sample surface and where lineage features existed they always pointed along the <110> directions. The (001) lattice planes in these samples were always displaced (with respect to those in the centre of the sample) towards the seed end along the <110> direction and towards the tail along the <100> directions. (001) lattice tilts distributions in tail end samples showed a less clear symmetry and lineage features were often observed lying along the <001> directions. In some of these samples only two-fold symmetry was observed about the <100> directions. This must reflect a different, less symmetrical thermal stress pattern encountered by the tail end of a crystal; the reason for this is not apparent.

Similar lattice strain and tilt measurements on an In-doped sample (melt composition 0.15 at % In) revealed larger lattice strains of 90ppm which had a 'W' shaped diametric profile. This is probably related to a combination of relative In concentration variations of 10% - 20% across the sample and variations of almost an order of magnitude in dislocation density. The lattice tilt in this sample was also greater than in any of the undoped samples and exhibited a convex shape with the central planes being misplaced in the growth

direction with respect to those at the periphery. The slip band dislocation distribution showed a correlation with the lattice tilt but its high magnitude was surprising considering the maximum dislocation density in this sample was an order of magnitude less than in any of the undoped samples. (Direct evidence was seen for this correlation at isolated slip bands where lattice tilts of ~5 arc seconds and strains of -7ppm were measured.) Since no two- or four-fold symmetry in the lattice tilt distribution was observed in this sample (a feature that was always present in the undoped samples) and because of the large tilts, it is likely that radial In concentration variations play a major role in determining the lattice tilt distribution as they do with the strain.

An investigation of the application of diffracted beam intensity measurements, (using the 200 quasi-forbidden reflection) to measure stoichiometry variations is presented in section 4. The 200 reflected beam intensity was found to be insensitive to dislocations (within the limits described in section 4) and as such should be ideal for these measurements. However, measurements on a dislocation-free sample using reflection topography showed a 10% decrease in diffracted intensity towards the sample edges. The magnitude of this change is far too large to be explained by stoichiometry variations and its origins are unclear. Optimisation of the diffraction conditions was undertaken on a synchrotron source in order to reduce the 200 diffracted beam intensity and hence improve the stoichiometry sensitivity. The reduction in rocking curve width which accompanied this optimisation revealed a splitting of the sample rocking curve which is believed to be due to micro-misorientations in the dislocation-free sample. Stoichiometry measurements on this sample were inconclusive but experiments are described which should permit unambiguous use of the technique to study stoichiometry variations in large diameter undoped LEC material.

The images of cell walls in double crystal topographs, taken under certain

diffraction conditions, were found to be broader than would be due solely to the dislocation images in those walls. By analysis of topographs taken under various diffraction conditions this was shown to be caused by a slight lattice parameter increase (<1ppm) which is consistent with the enhanced EL2 concentration known to exist in these areas (ref. 28). Comparisons of theoretical and experimental image widths of dislocations in a <111> cut sample from the seed end of a boule showed a broad agreement, indicating that the dislocation strain field is not greatly modified by the EL2 environment. This suggests that there is not a strong strain interaction between the EL2 centre and the dislocation strain field and adds to the suggestions that the interaction may be electrostatically driven.

REFERENCES

1. A E Payne, P C Newman 1984 GaAs and Related Compounds, Biarritz, Inst. of Phys. Conf. Series 74, p7
2. S Niyazawa, 1986, Semi-insulating III-V Materials, Hakone, p3
3. J Czochralski, Z. Physik. Chem. (Leipzig) 1917, 92 219
4. G K Teal, 1976, IEEE Transactions on Electron Devices, 23 621
5. E P A Metz, R C Miller, R Mazelsky, 1962, J.Appl.Phys. 33 2016
6. J B Mullin, B W Straughan, W S Brickell, 1965, J.Phys.Chem.Solids 26 782
7. D T J Hurle, 1977, J.Cryst. Growth 42 473
8. W Bardsley, G W Green, C H Holliday, D T J Hurle, 1972, J.Cryst.Growth 16 277
9. E M Swiggard, S H Lee, F W von Batchelder, 1977, Inst. Phys. Conf. Series 33b p23
10. D E Holmes, R T Chen, K R Elliot, C G Kirkpatrick 1982, Appl.Phys.Lett. 40 46
11. A Ojemel, J Costaing, 1986, Europhysics Lett. 2 611
12. S McGuigan, R N Thomas, H M Habgood, G W Eldridge, B W Swanson, 1986, Semi-insulating III-V Materials, Hakone, p29
13. T Kobayashi, H Kohda, H Nakanishi, F Hyuga, K Hoshikawa, 1986, Semi-insulating III-V Materials, Hakone, p17
14. Y Nanishi, S Ishida, T Hoda, H Yamazaki, S Miyazawa, 1982, Jap. J. Appl. Phys. 21, L335
15. T Egawa, Y Sano, H Matsuura, H Nakamura, K Kaminishi, 1986, Semi-insulating III-V Materials, Hakone, p567
16. R T Chen, D E Holmes, 1983, J. Cryst. Growth 61 111
17. Y Okada, 1983, J. Cryst. Growth 22 413
18. J G Grambmaier, C B Watson, 1967, Phys. Stat. Sol. 32 K13
19. M S Abrehams, C J Buiocchi, 1965, J.Appl.Phys. 36 2855
20. J Angilello, R M Penski, G R Woolhouse, 1975, J.Appl.Phys. 46 2315
21. A S Jordan, R Caruso, A R Von Neida, J W Nielson, J.Appl.Phys. 52 3331
22. G T Brown, C A Warwick, 1986, J.Electrochem.Soc. Solid State Sci. and Tech. 133 2576
23. A G Cullis, P D Augustus, D J Stirland, 1980, J.Appl.Phys. 51 2556
24. T Matsumura, H Emori, K Terashima, T Fukuda, 1983, Jap.J.Appl.Phys. 22 L154
25. S Miyazawa, T Mizutani, H Yamazaki, 1982, Jap.J.Appl.Phys. 21 L542

26. T Honda, Y Ishii, S Miyazawa, H Yamazaki, Y Nanishi, 1983, Jap.J.Appl.Phys. 22 L270

27. M S Skolnick, L J Reed, A D Pitt, 1984, Appl.Phys.Lett. 44 447

28. M S Skolnick, M R Brozel, L J Reed, I Grant, D J Stirland, R M Ware, 1984,
J.Electronic Materials 13 107

29. D E Holmes, R T Chen, K R Ellit, C G Kirkpatrick, 1983, Appl.Phys.Lett. 43 305

30. C A Warwick, G T Brown, 1985, Appl.Phys.Lett. 46 574

31. T Kamejima, F Shimura, Y Matsumoto, H Watanabe, J Matsui, 1982, Jap.J.Appl.Phys. 21 L721

32. A F W Willoughby, C M H Driscoll, B A Bellamy, 1971, J.Materials Sci. 6 1389

33. M Nakajima, T Sato, T Inada, T Fukuda, K Ishida, 1986, Semi-insulating III-V Materials, Hakone, p181

34. Y Okada, Y Tokumara, 1986, Semi-insulating III-V Materials, Hakone, p175

35. M E Straumanis, C D Kim, 1965, Acta Cryst. 19 256

36. H Kuwamoto, D E Holmes, 1986, J.Appl.Phys. 59 656

37. Y Okada, Y Tokamara, Y Kadota, 1986, Appl.Phys.Lett. 48 975

38. R A Stein, 1986, Advanced Materials for Telecommunication XIII, Proc. E MRS, p77

39. K Terashima, O Ohmori, A Okada, M Watanabe, T Nakanisi, 1986, Semi-insulating III-V Materials, Hakone, p187

40. K Terashima, J Nishio, A Okada, S Washizuka, M Watanabe, 1986, J.Cryst.Growth 79 463

41. T Sato, M Nakajima, T Fukuda, K Ishida, 1986, Appl.Phys.Lett. 49 1599

42. Y Takano, T Ishiba, Y Fukisaki, J Nakagawa, T Fukuda, 1986, Semi-insulating III-V Materials, Hakone, p169

43. D E Holmes, H Kuwamoto, C G Kirkpatrick, R T Chen, 1984, Semi-insulating III-V Materials, Kah-nee-ta, p204

44. S Martin, M Duseaux, M Erman, 1984, 11th Int. Symp. on GaAs and related compounds. Inst. of Phys. Conf. Series 74, p53

45. K Lohnert, W Wettling, G Koschek, 1986, Semi-insulating III-V Materials, Hakone, p267

46. T Obakata, T Matsumura, K Terashima, F Orito, T Kikuta, T Fukuda, 1984, Jap.J.Appl.Phys. 23 L602

47. R C Stoakes, A F W Willoughby, I R Grant, 1986, Semi-insulating III-V Materials, Hakone, p231

48. U Kaufmann, J Windscheif, M Baeumlert, J Schneider, F Kohl, 1984, Semi-insulating III-V Materials, Kah-nee-ta, p246

49. J Matsui, T Kitano, T Makejima, T Ishikawa, 1984, Inst. of Phys. Conf. Series 74, Int.Symp. on GaAs and Related Compounds, Biarritz, p101

50. T Kitano, T Ishikawa, J Matsui, 1986, Jap.J.Appl.Phys. 25 L282

51. T Kitano, T Ishikawa, H Ono, J Matsui, 1986, Jap.J.Appl.Phys. 25 L530

52. T Kitano, T Ishikawa, H Ono, J Matsui, 1986, Semi-insulating III-V Materials, Hakone, p91

53. H Miyari, T Inada, T Obakata, M Nakajima, T Katsumata, T Fukuda, 1985, Jap.J.Appl.Phys. 24 L729

54. B Pichard, N Burle-Durbec, F Minari, M Duseaux, 1985, J.Cryst.Growth 71 648

55. M P Scott, S S Laderman, A G Elliot, 1985, Appl.Phys.Lett. 47 1280

56. A Chabli, E Molva, A George, F Bertin, P Bunod, J Bletry, 1986, Advanced Materials for Telecommunications XIII Proc. E MRS, p27

57. K Kitahara, K Kodama, M Ozeki, 1985, Jap.J.Appl.Phys. 24 1503

58. P W Yu, D C Walters, M C Mitchel, 1986, J.Appl.Phys. 60 3864

59. B K Tanner, 1976, X-Ray Diffraction Topography, Pergamon Press

60. B K Tanner, D K Bowen, 1980, Characterisation of Crystal Growth Defects by X-ray Methods, NATO Advanced Study Institute Series, 63

61. A R Lang, 1978, Techniques and Interpretation in X-ray Topography in Diffraction and Imaging Techniques in Materials Science, North-Holland Publishing Co., Amsterdam, Vol.II, p623

62. B W Batterman, H Cole, 1964, Rev. of Modern Physics 36 681

63. Z G Pinsker, 1978, Dynamical Scattering of X-rays in Crystals, Springer Series in Solid State Sciences, 3

64. C S Barrett, 1945, Trans. AIME 161, 15

65. W F Berg, 1931, Naturwissenschaften 19 391

66. S Kikuta, K Kohra, 1970, J.Phys.Soc.Jap. 29 1322

67. S Kikuta, 1971, J.Phys.Soc.Jap. 30 223

68. T Matsushita, S Kikuta, K Kohra, 1971, J.Phys.Soc.Jap. 30 1136

69. U Bonse, K Olthoff-Munter, A Rumpf, 1983, J.Appl.Cryst. 16 524

70. M Hart, A R D Rodriguies, J.Appl.Cryst. 1978, 11 248

71. T Ishikawa, S Kikuta, K Kohra, 1985, Jap.J.Appl.Phys. 24 L559

72. W L Bond, 1960, Acta Cryst. 13 814

73. M Hart, 1981, J.Cryst.Growth 55 409

74. S R Stock, H Chen, H K Birnbaum, 1986, Phil.Mag.A. 53 73

75. T Fukamachi, S Hosoya, T Kawamura, M Okunaki, 1977, Acta Cryst. A33 54
76. W L Bond, J Andrus, 1952, Am.Minerologist, 37 622
77. U Bonse, E Klapper, 1958, Z.Naturforschung 13a 348
78. M C Robert, F Lefaucheux, M Sauvage, 1981, J.Cryst.Growth 52 976
79. M M Swartschild, 1928, Phys.Rev. 32 162
80. J Yoshimura, 1984, J.Appl.Cryst. 17 426
81. C L Kuo, J C Biletto, 1984, J.Appl.Cryst. 17 442
82. S Kikuta, K Kohra, Y Sugita, 1966, Jap.J.Appl.Phys. 5 1047
83. D K Bowen, G F Clark, S T Davies, J R S Nicholson, K J Roberts, J N Sherwood, B K Tanner, 1982, Nuclear Instr. and Methods 195 277
84. D K Bowen, S T Davies, 1983, Nuclear Instr. and Methods 208 725
85. T Obokata, H Emori, T Fukuda, 1983, Jap.J.Appl.Phys. 22 L168
86. S Yasuami, H Mikami, A Hojo, 1983, Jap.J.Appl.Phys. 22 1567
87. E R Weber, H Ennen, U Kaufmann, J Windschief, J Scheider, T Wesinski, J.Appl.Phys. 513 6140
88. D J Stirland, I Grant, M R Brozel, R M Ware, 1983, Inst.of Phys.Conf.Series. 16 377
89. I Fujimoto, 1984, Jap.J.Appl.Phys. 23 L287
90. I Fujimoto, N Kamata, K Kobayashi, T Suzuki, 1986, GaAs and Related Compounds, Inst. of Phys.Conf.Series 79 199
91. D A Hope, M S Skolnick, B Cockayne, J Woodhead, R C Newman, 1985, J.Cryst.Growth 71 795
92. K Terashima, T Katsumata, F Orito, T Kikuta, T Fukuda, 1983, Jap.J.Appl.Phys. 22 L325
93. M A G Halliwell, M H Lyons, B K Tanner, Ilczyzyn, 1983, J.Cryst.Growth 65 672
94. D J Stirland, M R Brozel, I Grant, 1985, Appl.Phys.Lett. 46 1066
95. S Tagaki, 1962, Acta Cryst. 15 1311
96. D Taupin, 1964, Bull.Soc.Fr.Min.Cryst. 87 469
97. A Authier, 1978, Diffraction and Imaging Techniques in Materials Science, North Holland Publishing (Amsterdam), Vol.II, p115
98. J F Petroff, A Authier, 1966, Phys.Stat.Sol. 13 373
99. J Miltat, D K Bowen, 1965, J.Appl.Cryst. 8 657
100. N Kato, 1963, J.Phys.Soc.Jap. 18 1785
101. N Kato, 1964, J.Phys.Soc.Jap. 19 67
102. E Dunia, C Malgrange, J F Petroff, 1974, Phil.Mag. A41 291
103. A Authier, 1968, Phys.Stat.Sol. 27 77
104. A Authier, J R Patel, 1975, Phys.Stat.Sol. A27 213

105. R L Barnes, P E Freeland, E D Kolb, R A Laudise, R J Patel, 1978, J.Cryst.Growth 43 676
106. A Authier, F Balibar, 1967, Phys.Stat.Sol. 21 413
107. S Tagaki, 1969, J.Phys.Soc.Jap. 26 1239
108. D Taupin, 1967, Acta Cryst. 23 25
109. A Authier, A Malgrange, M Tournaire, 1968, Acta Cryst. A24 126
110. C Nourtier, D Taupin, 1981, J.Appl.Cryst. 14 432
111. Y Epelboin, 1977, Acta Cryst. A33 758
112. Y Epelboin, 1979, Phys.Stat.Sol. (a) 54 547
113. Y Epelboin, 1981, Acta Cryst. A37 132
114. Y Epelboin, 1983, Acta Cryst. A37 761
115. Y Epelboin, A Soyer, 1985, Acta Cryst. A41 67
116. K Ishida, A Otuka, S Takagi, 1981, Phil.Mag. A43 935
117. Y Epelboin, 1979, J.Appl.Phys. 50 1312
118. B Jenichen, R Köhler, 1981, Phys.Stat.Sol. (a) 65 245
119. Y Epelboin, M Gandais, C Willaime, 1977, Phys.Stat.Sol. (a) 44 651
120. T Bedynska, 1973, Phys.Stat.Sol. (a) 18 147
121. J Gronkowski, 1980, Phys.Stat.Sol. (a) 57 105
122. F Petroff, M Sauvage, P Riglet, H Hashizume, 1980, Phil.Mag.A 42 319
123. P Riglet, M Sauvage, J E Petroff, Y Epelboin, 1980, Phil.Mag.A 42 339
124. A N Stroh, 1958, Phil.Mag. 3 625
125. M O Tucker, 1968, Phil.Mag. 19 1141